

The effect of mildly rapid strain on turbulent pipe flow

Udhav U. Gawandalkar

Technische Universiteit Delft

The effect of mildly rapid axisymmetric strain on turbulent pipe flow

by

Udhav U. Gawandalkar

to obtain the degree of Master of Science
at the Delft University of Technology,
to be defended publicly on Tuesday October 22, 2019 at 14:00
P & E Report Number: 2993

Student number:	4746430
Project duration:	November 1, 2018 – October 22, 2019
Thesis committee:	Prof. dr. ir. J. Westerweel, TU Delft, supervisor
	Dr. ir. G. E. Elsinga, TU Delft, supervisor
	Prof. dr. ir. C. Poelma, TU Delft
	Dr. ir. F. F. J. Schrijer, TU Delft

An electronic version of this thesis is available at <http://repository.tudelft.nl/>.

Acknowledgements

I thank Prof. dr. Jerry Westerweel for providing me with an opportunity to work in the laboratory for aero and hydrodynamics and guiding me at critical times amidst his busy agenda. A huge thanks to Dr. Gerrit Elsinga, your perspective and depth of knowledge in the subject was awe-inspiring. Thank you for being extremely approachable, I have learnt ample from our discussions. I also thank you for taking the time to proof-read my thesis. It is only because of your timely critical feedback, guidance and motivation, I am able to hand in this thesis on time. I will be fortunate to work with you in the future. Further, I extend my gratitude to Prof. dr. C. Poelma and Dr. F. Schrijer for agreeing to be a part of my thesis committee.

This thesis would not have been complete without the help of Edwin, whom I have pestered throughout the experimental campaign with random queries. Thanks for going out of your way at times to help me with the test-section. Further, I thank you for teaching me various aspects of PIV from scratch, your experience and insight has benefited me immensely. Jasper, thanks for building various articles and your practical suggestions that have saved me ample of time. Thank you for taking responsibility for polishing the test section without which I could not start my experiments. I would also like to thank Jan for promptly helping me with DAQ systems and pressure measurement. Further, I thank Caroline for arranging my masters defense.

I would like to thank Saad Jahangir for providing me with an opportunity to perform experiments in venturi. It was indeed a brilliant learning experience for me. Thanks to all the PhDs and master students in the lab for helping out whenever I approached you. A special thanks to Sudarshan and Ankur for free coffees, pass-card and random chats in the evenings. I am very thankful to Kalpit for the lunches and random discussion (technical/non-technical), I have found a good friend in you during the course of this thesis. Thank you to all my beloved friends in Delft for offering me much-needed respite and distractions after work and on the weekends: Bishwa, Shrinivas, Sarvesh. Thanks to Kishan, Filippo and entire Tam-gang for their kind words and motivation from time to time. I also thank Anand for proof-reading this thesis.

Lastly, and most importantly, a huge thanks to my maa, pappa and family back in India for their unconditional love, support and financial help during my stay in the Netherlands. Further, Rav thanks for dealing with me patiently during the busy thesis time.

*Udhav U. Gawandalkar
Delft, October 2019*

Abstract

The way in which mean strain affects the turbulent structures is imperative to understand various natural flows such as flow over a hill, the flow of a river in the delta, jet streams in the upper atmosphere etc. Further, it also has industrial implications viz; flow over bodies such as airfoil, turbomachinery, gas pipelines. The strained pipe flows, in particular, have huge engineering interest due to its prevalence in industrial fittings wherein a larger pipe diameter is connected to a smaller one and vice versa. This subject also has a fundamental interest as strain highlights the interaction of various scales of turbulence. This scale interaction essentially dictates transfer of energy in turbulence and hence is fundamental in understanding turbulence dynamics itself.

The present work deals with the experimental study of the response of pipe turbulence to axisymmetric, irrotational strain using high-resolution planar Particle Image Velocimetry (PIV). A mildly rapid strain ($s^{*s} \leq 3.2$) is imposed on turbulence via a spatial contraction. It is seen that turbulence is suppressed upon straining. As a response to mean strain, transverse Reynolds stress increases at the expense of streamwise Reynolds stress and anisotropy is induced in the turbulence. Despite strain being only mildly rapid, Rapid Distortion Theory (RDT) is found to predict the correct trend of normal Reynolds stress although transverse Reynolds stress is over-predicted.

The effect of strain on different scales of turbulence is discerned. The large scales of turbulence are seen to get compressed in the radial direction although they do not get affected significantly in the streamwise direction. Near-wall coherent structures which were initially inclined w.r.t. the wall are seen to get aligned with the flow as they also get severely compressed in the radial direction. On the other hand, the small scales of turbulence are found to be spatially organised in the form of sheets or layers. Upon straining, these sheets are found to get aligned with the mean flow. Further, they get elongated in streamwise and compressed in the radial direction. It is observed that the small scales are more severely distorted than the large scales upon straining inside the contraction. At the Reynolds number (Re) range employed in this thesis, there is no substantial difference in which turbulence is strained inside the contraction at disparate Re . Downstream of the contraction, at the axis of the pipe, the anisotropy of Reynolds stress is found to recover slowly. Further, this relaxation is seen to be Re dependent with higher Re turbulence relaxing slightly faster.

Contents

Acknowledgement	iii
Abstract	v
Nomenclature	x
List of figures	xiv
List of tables	xv
1 Introduction	1
1.1 Motivation	1
1.2 Research Theme	2
1.3 Outline of Thesis	2
2 Background theory	3
2.1 Turbulent flows	3
2.2 Turbulence scale interaction: The heart of turbulence dynamics	4
2.3 Isotropic turbulence	6
2.4 Turbulent scales: The measure of large and small scales	7
2.5 Flow topology	8
2.6 Pre-contraction: Straight pipe.	8
2.7 Contraction: The effect of axial strain on the pipe flow	10
2.7.1 The effect of axial strain on the mean flow	10
2.7.2 The effect of axial strain on turbulence.	11
2.7.3 Rapid Distortion Theory (RDT)	11
2.8 Post-contraction	13
3 Relevant experimental and numerical observations: A literature review	15
3.1 The effect of rapid strain on turbulence.	15
3.2 Spatially accelerated wall-bounded Turbulence.	20
3.3 Temporally accelerated wall-bounded flows	23
3.4 Discussion	25
3.5 Research objectives and questions	25
4 Flow in a venturi: A preliminary experiment	27
4.1 Motivation	27
4.2 Experiment setup	27
4.2.1 Flow facility	27
4.2.2 Measurement technique: Planar PIV.	28
4.2.3 Design of experiment	30
4.2.4 Remark	31
4.3 Results and discussion	33
4.3.1 Mean flow	33
4.3.2 Turbulent statistics.	36
4.4 Mathematical model	40
5 Experiments in long pipe: The effect of mildly rapid strain on turbulence	43
5.1 Experimental setup	43
5.1.1 Flow facility	43
5.1.2 Design of contraction	44
5.1.3 Design of experiments	47
5.1.4 Measurement Technique: PIV	48

5.2	Data validation	50
5.3	Results and discussions	53
5.3.1	The effect of strain on pipe flow statistics	54
5.3.2	Turbulence evolution by mildly rapid strain rate	55
5.3.3	The effect of strain on turbulent structures.	60
5.3.4	Turbulence evolution in post-contraction region	65
6	Conclusions and recommendations	69
6.1	Conclusion	69
6.2	Recommendation for future work.	70
A	Appendix 1: Optical anomaly - 1	71
B	Appendix 2: Optical anomaly - 2	73
C	Appendix 3: Calibration	75
D	Appendix 4: Optical anomaly-3	77

Nomenclature

Abbreviations

BL	Boundary Layer
FOV	Field Of View
IW	Interrogation Window
PIV	Particle Image Velocimetry
TBL	Turbulent Boundary Layer
TI	Turbulent Intensity
TKE	Turbulent Kinetic Energy

List of Symbols

Δt	Laser pulse separation
δ	Boundary layer thickness
ϵ	Turbulent Kinetic dissipation
η	Kolmogorvs length scale
ν	Kinematic viscosity of water
$\overline{u'u'}$	Streamwise normal Reynolds stress
$\overline{u'v'}$	Reynolds shear stress
$\overline{u'}$	streamwise velocity fluctuation
$\overline{u_{c,i}^2}$	Streamwise normal Reynolds stress at the centre of pre-contraction straight pipe
$\overline{u_{c,i}}$	Mean incoming centreline axial velocity
$\overline{u_c}$	Mean centreline axial velocity
\overline{u}	Mean axial velocity
$\overline{v'v'}$	Transverse normal Reynolds stress
$\overline{v'}$	Transverse velocity fluctuation
$\overline{v_{c,i}^2}$	Transverse normal Reynolds stress at the centre of pre-contraction straight pipe
\overline{v}	Mean radial velocity
$\overline{w'w'}$	Spanwise normal Reynolds stress
$\overline{w'}$	spanwise velocity fluctuation
\overline{w}	Mean spanwise velocity
$\sqrt{\overline{u'u'}}$	urms fluctuation
$\sqrt{\overline{v'v'}}$	vrms fluctuation

b_{11}^s	Surrogate of Reynolds stress anisotropy
b_{11}	Reynolds stress anisotropy
C	Area-based contraction ratio
D	Diameter of the pipe
d_i, d_o	Image and object distance
f_B	Blasius friction factor
f_D	Darcy-Weisbach friction factor
K	Acceleration Parameter
k	Turbulent kinetic energy
K_{Cr}	Critical acceleration Parameter
L_c	Length of contraction
M	Image magnification
P	Pressure
R	Local radius of pipe
r	Radial distance
$R_{\omega\omega}$	Vorticity correlation coefficient
R_{uu}	Streamwise correlation coefficient
R_{vv}	Transverse correlation coefficient
Re	Reynolds number based on bulk velocity
S	Mean strain rate
s^{*s}	Surrogate non-dimensionalized strain rate
s^*	Non-dimensionalized strain rate
T_E	Eddy turn-over time
u^*	Wall-friction velocity
U_b	Bulk velocity
x	Axial/streamwise distance
y	Wall-normal distance
y^+	Wall units

List of Figures

1.1	Typical examples of flows involving straining-relaxation cycles; (a) Flow over an airfoil. (b) Flow in a pipe with a contraction.	1
2.1	Turbulent jet flow showing eddies of different sizes, cyan and red boxes show typical small and large turbulent scales respectively. The image is reproduced from: Van Dyke, An album of fluid motion.	4
2.2	Vortex stretching in x direction, (a) before stretching (b) after stretching : strain is positive in x and negative in y or z (The image is reproduced from [1]).	5
2.3	A schematic explaining energy cascading process in pipe turbulence.	5
2.4	The pipe flow with axisymmetric contraction, D_i is the inlet diameter of pipe, D_0 is the outlet diameter of contraction, L is the length of the contraction, $u_{x,1}(r)$ is the fully developed velocity profile in precontraction region, $u_{x,2}(r)$ is the fully developed velocity profile in pre-contraction region, post-contraction.	8
2.5	Fully developed pipe flow with velocity profile $(\overline{u_x}(r))$, diameter D_i , pressure gradient $(\frac{d\overline{P}}{dx})$	9
2.6	The dimensionless mean velocity profile ($u^+ = \frac{\overline{u}}{u_\tau}$) in a turbulent pipe flow as a function of r ; showing different regions as discussed above equation 2.22,2.23,2.24 (taken from [2]).	10
2.7	Wind tunnel with axisymmetric contraction showing vortex stretching [3].	12
2.8	Normal reynolds stress variation normalised with pre-contraction turbulent statistics with contraction ratio (strain ratio) predicted by RDT [4].	13
3.1	The comparison of Rapid Distortion Theory (RDT) with Uberoi et. al. [5] and Hussain et. al. [6].	16
3.2	Peak shifting in $E_{11}(k)$ and second peak occurrence in $E_{22}(k)$ reported in [7]; (1)-(6) corresponds to disparate grids and Re cases examined. (6) being the largest $Re_\lambda \sim 470$	18
3.3	Stretching of turbulence structure due to axial strain [8].	19
3.4	Different regimes in accelerated boundary layer [9].	21
3.5	figure 1 (a) from [10] Streaks and vortex structures in three-dimensional plots of isosurfaces. Streaks are shown in green/blue and vortical structures are shown in red.	25
4.1	Schematic diagram of closed flow loop (flow is from left to right). Part 12: Inlet section of length $40D$, 2: Venturi test section, 4: Pressure recovery section, 5: Temperature sensor, 9: Vaccum pump 10: centrifugal pump, 11: Flowmeter, 1,3,6,8: Pressure ports (taken from: Jahangir et. al. [11]).	28
4.2	Venturi test section (red arrows show flow direction) ([11]).	29
4.3	Experimental setup and planar PIV measurement system.	29
4.4	(a) A typical raw particle image. (b) A Typical time-averaged velocity vector field (Note that every fourth velocity vector is shown for the sake of clarity); The flow is from left to right.	30
4.5	Designed measurement campaign with different FOVs (red box show schematics of various FOVs).	30
4.6	(a) Non dimensioned strain rate (s^*). (b) Acceleration parameter (K) along the axis of convergent part of venturi for $Re = 60,000$. See 2.26, 2.27 for definitions Note that $x=0$ corresponds to the inlet of CS, $x=0.051$ to throat.	31
4.7	(a) Convergence plot of mean velocity at a point (Centreline of the CS). (b) Convergence plot of streamwise velocity fluctuations at a point (Centreline of the CS). Note that residual is defined on the basis of old value (0) and new value (i) of the quantity such that Residual = $(i - 0)/0$	31
4.8	(a) Velocity-time signal measured at a point on the axis of CS by PIV. (b) Pressure time signal measured by pressure transducer upstream of venturi.	32
4.9	(a) Two-point correlation of velocity fluctuations(R_{uu}) for $Re= 35,000$ in CS. (b) Two-point correlation of vorticity ($R_{\omega\omega}$) for $Re= 35,000$ in CS. (Red boxes indicate the PIV cross-correlation interrogation window).	32

4.10	Schematic of measurement domain showing various radial profiles over which data has been shown in the this section. Note that the flow is from left to right with 0 being the inlet of venturi and 170mm being the exit of the venturi.	33
4.11	(a) Mean axial velocity $u(x)$ normalised by inlet flow velocity U_{in} in the straight pipe upstream of venturi vs. axial distance along the centreline of venturi. (b) Mass of fluid passing through each cross-section of venturi compared with mass flow rate measured by flow meter.	34
4.12	Instantaneous velocity contour plots as the function of time qualitatively showing flow separation in the DS for $Re = 10,000$ (a) $t = 1$ sec (b) $t = 2$ sec (c) $t = 3$ sec (d) $t = 4$ sec (e) $t = 5$ sec.	34
4.13	Instantaneous velocity contours as the function of time qualitatively showing flow separation in the DS for $Re = 60,000$ (a) $t = 1$ sec, (b) $t = 2$ sec (c) $t = 3$ sec (d) $t = 4$ sec (e) $t = 5$ sec.	35
4.14	(a) Mean axial velocity $u(x)$ plotted along radial direction for L_1, L_2, L_3 for CS for $Re=35,000$. (b) Mean axial velocity $u(x)$ plotted along the radial direction for L_4, L_5, L_6, L_7 for DS for $Re=35,000$. For inset see figure 4.10.	35
4.15	(a) Measured mean axial velocity profile (normalised by centreline velocity) inside contraction at L_2 for $Re= 35,000$ compared with fully developed axial velocity in straight pipe for $Re= 5,300$ (figure 2 in Eggels et.al. [12]). (b) Mean radial velocity profile $v(x)$ in CS at L_1, L_2, L_3 for $Re = 35,000$. For inset see figure 4.10.	36
4.16	(a) Velocity fluctuations (u'), (v') normalised by centreline velocity ($u(x)$) along the centreline of venturi for $Re= 35,000, 60,000, 71,300$. (b) Velocity fluctuations (u'), (v') normalised by incoming bulk velocity (u_{in}) along the centreline of venturi for $Re= 35,000, 60,000, 71,300$	37
4.17	(a) Streamwise Normal Reynolds stress as a function of local contraction ratio (C) compared with data of Hussain et.al. [6]. (b) Transverse Normal Reynolds stress as a function of local contraction ratio (C) compared with data of [6]. \bullet : current measurement, \cdots : trendline through measured data, Theory: Rapid Distortion Theory (RDT) predictions [4], Uberoi: Data from [5]	37
4.18	(a) Streamwise turbulent intensity at various profiles (L_1, L_2, L_3). (b) Transverse turbulent intensity at various profiles (L_1, L_2, L_3) for $Re 35,000$. For inset see figure 4.10.	38
4.19	(a) Reynolds shear stress ($u'v'$) normalised by local centreline velocity square along profiles L_1, L_2, L_3 for $Re= 35,000$. (b) Absolute Reynolds shear stress ($u'v'$) along profiles L_1, L_2, L_3 for $Re= 35,000$. For inset see figure 4.10.	38
4.20	Evolution of two-dimensional surrogate of Reynolds stress anisotropy tensor component b_{11}^s along the axis of venturi.	39
4.21	(a) Streamwise turbulent intensity at various profiles (L_4, L_5, L_6, L_7). (b) Transverse turbulent intensity at various profiles (L_4, L_5, L_6, L_7) for $Re= 35,000$. (c) Reynolds shear stress at various profiles (L_4, L_5, L_6, L_7). For inset, see figure 4.10.	40
5.1	Long pipe flow facility at the laboratory for aero and hydrodynamics, Delft (The flow is from left to right). A : Reservoir, B: Centrifugal pump, C: Settling chamber followed by contraction, D ₁ , D ₂ : Pressure Taps, E: Test Section with contraction, F:Flowmeter, G: Discharge chamber, H: Return pipe.	44
5.2	(a) Computer aided drawing of the designed test section (all dimensions are in mm). (b) Fabricated Test section with contraction (Component E in figure 5.1) made of PMMA.	45
5.3	(a) Measured friction factor (f_D) compared with Blasius friction correlation for smooth pipes. (b) Relative % error in measurement (f_D) w.r.t. Blasius's theoretical expression (f_B). It might be important to note that different pressure transducers were used for $Re \leq 35,000$ and $Re > 35,000$ to consider working range of sensor.	46
5.4	The contraction profile is shown in green; radial position vs. axial position. A fifth order polynomial can be fitted through the contraction profile with fit residual of $R^2 \sim 0.9999$	46
5.5	A schematic showing different FOVs over which measurements were performed. FOV-1: straight pipe upstream of contraction, FOV-2: Inside the contraction, FOV-3: Downstream of contraction, FOV-4: Further downstream of contraction, FOV-5: zoomed into contraction.	47
5.6	A typical particle image with optical artefact in FOV-3. Notice vertical stripping and local distinct blurry appearance of particle images on the left end of particle image (red box). At these corresponding points, cross-correlation coefficient drops to as low as 0.3 resulting in low signal to noise ratio. However, region of relatively good correlation is shown in green box.	48

5.7	Setup for a planar PIV measurement; 1: Dual head Nd:YAG Laser, 2: High resolution camera, 3: Test Section, 4, 5, 8: Plane mirror, 6: Spherical convex lens, 7: Plano-concave cylindrical lens. Note also that the cartoon of laser sheet is shown.	49
5.8	(a) Instantaneous velocity vector field in FOV-1. (b) Instantaneous velocity vector field in FOV-5. Note that every fourth vector is shown in the field for the sake of clarity and the flow is from left to right.	50
5.9	(a) Mean axial velocity profile ($\overline{u^+} = \frac{\overline{u}}{u^*}$) vs radial distance ($\frac{r}{R}$) (outer scaled with pipe radius). (b) Mean axial velocity profile ($\overline{u^+}$) vs wall normal distance (y^+) (inner scaled with wall units).	51
5.10	(a) Stream-wise velocity fluctuation, ($\text{rms} u^+ = \frac{\sqrt{\overline{u'u'}}$) vs radial distance ($\frac{r}{R}$) (outer scaled with pipe radius). (b) Rms u^+ vs wall normal distance (y^+) (inner scaled with wall units) at different Re	51
5.11	(a) Transverse velocity fluctuation ($\text{rms} v^+ = \frac{\sqrt{\overline{v'v'}}$) vs radial distance ($\frac{r}{R}$) (outer scaled with pipe radius). (b) Rms v^+ vs wall normal distance (y^+) (inner scaled with wall units)	52
5.12	Reynolds shear stress normalised by u^{*2} ($\overline{u'v'^+} = \frac{\overline{u'v'}}{u^{*2}}$) vs radial distance normalised by pipe radius (outer scaled) at different Re	52
5.13	(a) Two-point correlation of velocity fluctuations (R_{uu}) vs axial separation. (b) Two-point correlation on out of plane vorticity ($R_{\omega\omega}$) vs axial separation. Both the quantities have been normalised by their respective covariance.	53
5.14	Mean axial velocity at the centreline normalised by the incoming centreline velocity at the centre of contraction as a function of axial distance (a) (x) unscaled. (b) scaled (x/D).	53
5.15	(a) The gradient of the mean centreline velocity as a measure of mean strain rate. (b) Non-dimensionalized strain rate (s^{*s}) along the centreline of contraction.	54
5.16	A schematic showing axial positions along which profiles have been plotted in the subsequent sections.	54
5.17	Mean axial velocity profile normalised by centreline velocity at different axial positions i.e. L0, L1, L2 for (a) $Re=25,000$. (b) 35,000. (c) 47,700.	55
5.18	(a) Mean radial velocity profile normalised by local centreline velocity at different axial positions L0, L1, L2 for (a) $Re=25,000$. (b) 35,000. (c) 47,700.	55
5.19	(a) Streamwise velocity fluctuations $\sqrt{\overline{u'u'}}$ (urms) normalised by incoming centreline velocity ($\overline{u_{c,i}}$) at different axial positions i.e. L0, L1, L2 for (a) $Re=25,000$. (b) 35,000. (c) 47,700.	56
5.20	(a) Streamwise turbulent intensity $\sqrt{\overline{u'u'}}$ profile normalised by local centreline velocity ($\overline{u_c(x)}$) at different axial positions L0, L1, L2 for (a) $Re=25,000$. (b) 35,000. (c) 47,700.	56
5.21	(a) Transverse velocity fluctuations $\sqrt{\overline{v'v'}}$ (vrms) profile normalised by incoming centreline velocity ($\overline{u_{c,i}}$) at different axial positions i.e. L0, L1, L2 for (a) $Re=25,000$. (b) 35,000. (c) 47,700.	57
5.22	(a) Transverse turbulent intensity $\sqrt{\overline{v'v'}}$ (vrms) profile normalised by local centreline velocity ($\overline{u_c(x)}$) at different axial positions i.e. L0, L1, L2 for (a) $Re=25,000$. (b) 35,000. (c) 47,700.	57
5.23	(a) Streamwise Reynolds stress evolution inside the contraction at different Re (25,000, 35,000, 47,700) compared with Batchelor and Proudman [4], Uberoi [13], Hussain et.al. [6], Ertunc et.al. [14]. (b) Transverse Reynolds stress evolution inside the contraction at different Re (25,000, 35,000, 47,700) compared with Batchelor and Proudman [4], Uberoi [13], Hussain [6], Ertunc et.al. [14].	58
5.24	Surrogate Reynolds stress anisotropy tensor (b_{11}^s) as a function of local contraction ratio for $Re = 25,000, 35,000, 47,700$	58
5.25	The evolution of turbulent kinetic energy inside the contraction at L0, L1, L2 for Re (a) 25,000. (b) 35,000. (c) 47,700.	59
5.26	The evolution of rms enstrophy inside the contraction at L0, L1, L2 for Re (a) 25,000. (b) 35,000. (c) 47,700.	59
5.27	The evolution of Reynolds shear stress inside the contraction at L0, L1, L2 for Re (a) 25,000. (b) 35,000. (c) 47,700.	59
5.28	Sample two-point correlation coefficient at $Re=35,000$ (a) R_{uu} in the pre-contraction straight section. (b) R_{uu} inside the contraction (the artefacts in correlation is due to the optical anomaly; see appendix D). (c) R_{vv} in the pre-contraction straight section. (d) R_{vv} inside the contraction. The flow is from left to right.	60

5.29	R_{uu} at the axis of the pipe and contraction (a) along streamwise direction, (b) along the radial direction at $Re = 25,000, 35,000, 47,700$	61
5.30	Sample two-point correlation R_{uu} at $r/R = 0.82$ at $Re=35,000$; (a) In the straight pre-contraction straight section. (b) Inside the contraction; Note: The flow is from left to right; the vertical strips in the (b) is the result of optical artefacts, see appendix D.	61
5.31	Sample two-point correlation R_{vv} at $r/R = 0.82$ at $Re=35,000$; (a) In the straight pre-contraction straight section. (b) Inside the contraction. Note that the flow is from left to right	62
5.32	Iso-contours of swirling strength realised with DNS, reproduced from [8] (figure 20); left to right: straight section to progressively inside of contraction.	62
5.33	Taylor micro-scale comparison in the pre-contraction to inside the contraction for (a) $Re = 25,000$. (b) $Re = 35,000$	63
5.34	Vorticity correlation ($R_{\omega\omega}$) as a function of axial separation at $Re = 35,000$ at various axial locations; (a) Straight pipe (L0). (b) at L1. (c) at L2. (d) The spatial extent of vorticity correlation in terms of Kolmogorov's length scale (η).	64
5.35	Mean axial velocity profile normalised by centreline velocity at different axial positions L0, L1, L2, L3, L4 for Re (a) 25,000 (b) 35,000 (c) 47,700.	65
5.36	Streamwise velocity fluctuations (urms) normalised by incoming centreline velocity at different axial positions i.e. L0, L1, L2, L3, L4 for Re (a) 25,000. (b) 35,000. (c) 47,700.	65
5.37	Transverse velocity fluctuations (vrms) normalised by incoming centreline velocity at different axial positions L0, L1, L2, L3, L4 for Re (a) 25,000. (b) 35,000. (c) 47,700.	66
5.38	Surrogate Reynolds stress anisotropy component (b_{11}^s) along the axial length of contraction.	66
5.39	Reynolds shear stress normalised by the square of incoming centreline velocity at different axial positions i.e. L0, L1, L2, L3, L4 for (a) $Re = 25,000$. (b) 35,000. (c) 47,700.	67
5.40	Sample two-point correlation at axis of pipe at $Re=35,000$ at axial distance equivalent to L4 (a) R_{uu} . (b) R_{vv} . The flow is from left to right.	67
5.41	R_{uu} at the axis of in pipe in pre-contraction straight section (Pre-C), inside the contraction (C), post-contraction (Post-C); (a) Along streamwise direction. (b) Along the radial direction at $Re = 25,000, 35,000, 47,700$	67
A.1	Calibration Target with grid spacing 2mm and 2mm '+'	71
A.2	Calibration grid generated with 3 rd order polynomial fitting	72
A.3	Qualitative ray tracing diagram for current test setup. source: Ray Optics Simulation	72
A.4	Final corrected calibration in two different sections	72
B.1	Particle images with streaks caused by diffraction. The interference pattern shown in white box was reported in [15]	73
B.2	The diffraction due to gratings (courtesy:Thorlabs Inc.)	74
B.3	Surface plot of intensity for particle image as shown in the inset (with thresholding).	74
B.4	Left: Intensity plot along a yellow profile line with fitted Gaussian function for a imaged particles streak. Right: Intensity plot along a yellow profile line for un-diffracted particle image	74
D.1	Cross-correlation coefficient over IW of particle images throughout the measured FOV.	77

List of Tables

4.1	Test matrix for experiments in venturi	31
5.1	Test matrix for experiments in long pipe.	47

Introduction

1.1. Motivation

The effect of mean strain on the turbulence has been studied for a long time. Such strained turbulent flows are inevitable and encountered frequently in aero and hydrodynamics viz; environmental flows such as flow over hills, flow of river in a delta, flow around bodies like airfoils and bluff bodies, impinging jet in paint and inkjet printing industry, turbine blade cascade in turbomachinery, pipe and channel flows with contraction or expansion [1]. The pipe flows with contraction or expansion particularly have huge engineering interest. It is widely employed in industrial installations, turbomachinery [16], gas pipelines [17], where small diameter pipe is connected to the larger diameter pipe and vice versa via contraction or diffuser. Typically, the Reynolds number (Re) of such flows is high and the flow qualifies as fully turbulent. Hence, studying strained turbulence in pipe flow has significant engineering implications.

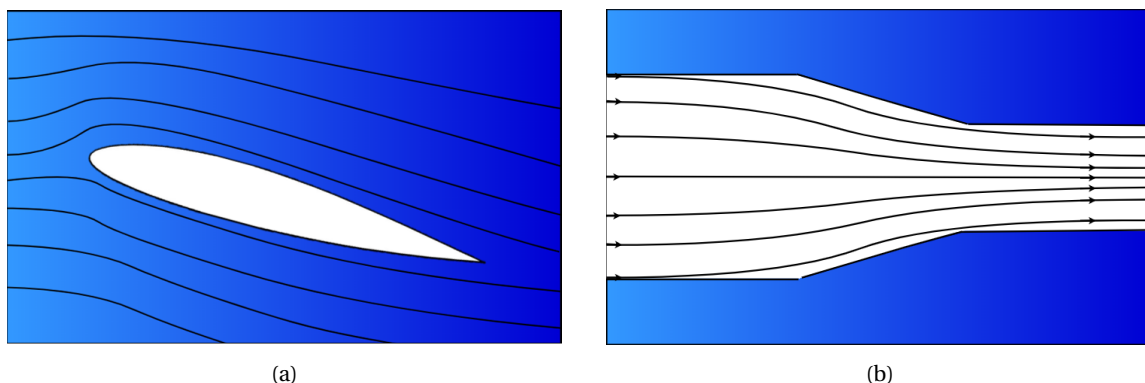


Figure 1.1: Typical examples of flows involving straining-relaxation cycles; (a) Flow over an airfoil. (b) Flow in a pipe with a contraction.

The mean strain can be introduced by the virtue of flow geometry [18]. This can be explained by a few canonical flows as illustrated in figure 1.1. For a turbulent flow around an airfoil, when the flow encounters the leading edge, flow experiences spatial acceleration (positive strain in axial direction), as evident by the squeezing of streamlines. Subsequently, it relaxes in the far-field away from the trailing edge as shown in figure 1.1a. Similarly, in the pipe or channel flows with a contraction, the contraction imposes a mean strain on the turbulent flow as a result of which it is accelerated. The mean strain strains the large eddies via vortex stretching which is analogous to larger eddies straining smaller eddies in the energy cascade process. The energy cascade classically is believed to be the heart of turbulence dynamics. The near isotropic turbulence essentially undergoes stretching resulting in the ordering of its structures i.e. anisotropy is introduced in its structures. Further, when strain is removed downstream as shown in figure 1.1b, turbulence relaxes back to isotropy. Evidently, as turbulence undergoes such a straining-relaxation cycle, there is tremendous turbulence-turbulence interaction along with the interaction of turbulence with mean flow. These interactions are an essential feature of turbulence which gives rise to the mutual transfer of energy from one component to another [1, 2, 18].

Furthermore, at high Reynolds number, the wider range of scales in the flow can result in a complex interaction between the scales and mean flow [19]. Hence, strained turbulent flows are fundamental to understanding turbulence dynamics itself. A thorough understanding of how different scales of turbulence respond to mean strain rate thus will help in gaining better insight into the physical mechanisms involved in rather esoteric yet intriguing turbulent flows.

1.2. Research Theme

This thesis aims at investigating the response of moderately high Reynolds number (Re) turbulent pipe flow subjected to mildly rapid strain imposed by a contraction. The focus is on studying the evolution of Reynolds stresses during straining and subsequent relaxation downstream of contraction with an emphasis on the core region. Further, the response of large and small of scales of turbulence are studied separately to gain insight into the physical mechanisms involved in strained turbulence using high resolution Particle Image Velocimetry (PIV) measurements [20–22]. PIV provides non-intrusive, whole-field velocity data that can be used to estimate spatial structures of turbulence [20, 23]. Furthermore, due to the mild rapidity of strain, linear Rapid Distortion Theory (RDT) (see section 2.7.3) must hold true. Hence, the secondary aim of this thesis is also to assess the validity of RDT for mildly rapid strain.

1.3. Outline of Thesis

The report has the following outline. The chapter 2 of this thesis deals with a brief introduction to turbulent flow and background theories that will set platform for the extensive literature survey is chapter 3. In this chapter, experimental and numerical observations made in the past involving accelerated/strained turbulent flow are summarised to arrive at research questions. Chapter 4 deals with a preliminary experiment performed in the venturi. Further, chapter 5 deals with experiments in the long pipe with contraction and observations made therein. Following this, conclusions of the current work and recommendation for future research are documented in chapter 6.

2

Background theory

This chapter provides knowledge of basic concepts and background theories pertaining to this thesis and turbulent flows in general. In section 2.1, 2.2, 2.3, definitions of various terms are explained that will be used vastly in the later chapters. Next, section 2.4 defines the measure of turbulent scales. The topology of flow under consideration is articulated in section 2.5 which is followed by pre-contraction flow description in section 2.6. The effect of axial strain on the mean flow and turbulence, with emphasis on Rapid Distortion Theory (RDT), is presented in section 2.7. The chapter is finally closed by briefly defining post-contraction flow in section 2.8.

2.1. Turbulent flows

"Turbulence still remains the most important unsolved problem of classical physics" - Richard Feynman (1918-1988).

Last century has generated a plethora of knowledge in the field of turbulent flows with the aid of state-of-the-art experimental and super-fast computing facilities. However, none of the descriptions of turbulent flows have been able to describe it completely [1]. Turbulence is omnipresent in nature with examples such as atmospheric boundary layers, jet-streams in the upper atmosphere, cloud cumulus, water flow in canals, rivers and also in, an industrial setting such as turbomachinery, turbulent flow over aircraft wing in the aerospace industry, turbulent mixing in combustion, chemical processes, turbulent flows in gas pipelines. Hence, understanding this phenomenon is imperative to manipulate it i.e. enhance or suppress it as desired.

The turbulent flows, in general, are characterised by irregularity, diffusivity, dissipation and high Reynolds number [18]. Although chaotic, turbulence is not completely random since it is possible to find a correlation between velocity measured at two nearby points in the flow field as a function of the distance between these two points. Such a correlation would not exist in a completely random process. Such a correlation is a manifestation of turbulent structures i.e. vortex-like structures of varying dimensions [2] sometimes referred to as 'eddies' (see figure 2.1). It is important to distinguish between these structures based on their dimension which is broadly classified as large and small structures. The distinct behaviour of these scales is characteristic to the fundamentals of turbulence dynamics. Secondly, turbulence is diffusive i.e. it has an inherent tendency to smear out or mix. This can also be seen in turbulent jet flow as shown in figure 2.1. Thirdly, turbulence cannot sustain itself and relies on external agents (such as shear in the mean flow) to draw energy from. Without an external agent, turbulence will decay and eventually dissipate via molecular diffusion. Further, the turbulent flows are characterized by high Reynolds number (Re) which is defined as the ratio of inertial forces to viscous forces in the flow. At high Re , there is a greater scale separation i.e. widely different sizes of structures are present. Further, at high Re , the smallest eddy gets progressively smaller while large eddies still scale with fluid dynamic length scale. Hence, high Re turbulent flows are more interesting due to the presence of complex interaction between these different sized structures.

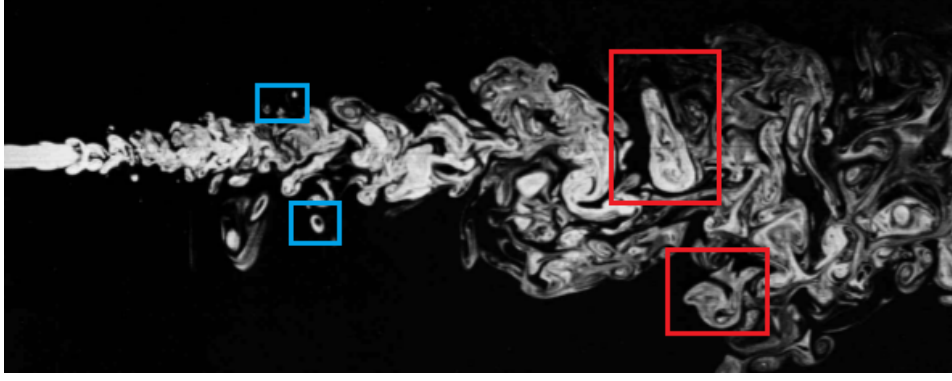


Figure 2.1: Turbulent jet flow showing eddies of different sizes, cyan and red boxes show typical small and large turbulent scales respectively. The image is reproduced from: Van Dyke, An album of fluid motion.

In turbulent flows, an instantaneous flow quantity can be expressed as a sum of ensemble mean and fluctuating component using Reynold's decomposition. Hence, flow quantity can be represented as; axial velocity (u): $u(x, t) = \bar{u} + u'$, radial velocity (v): $v(x, t) = \bar{v} + v'$, azimuthal velocity (w): $w(x, t) = \bar{w} + w'$. Physically, fluctuating component represents turbulent intensity in flow. Further, Navier-Stokes (NS) equations are time-averaged using the above definition of flow quantity to yield Reynolds averaged NS which is a mathematical description of turbulent flows. As a result of above averaging, terms like $\overline{u'v'}$ appear which have the same effect as stress acting on surface and hence is termed as Reynold's stresses [2]. In 2-D, Reynolds stress tensor is given by equation 2.1, where diagonal terms are normal stresses while off-diagonal terms are shear stresses. Throughout this report, $\overline{u'u'}$, $\overline{v'v'}$, $\overline{u'v'}$ will be referred to as streamwise, transverse and shear Reynold's stress respectively.

$$\overline{u'_i u'_j} = \begin{pmatrix} \overline{u'u'} & \overline{u'v'} \\ \overline{v'u'} & \overline{v'v'} \end{pmatrix} \quad (2.1)$$

Also, turbulent velocity fluctuations are used to define turbulent kinetic energy (k) (TKE) which is a key flow parameter in turbulent flows; $k \sim u_i'^2/2$. Having defined the relevant flow quantities, next subsection will focus on the significance of turbulent scale interaction in turbulence dynamics.

2.2. Turbulence scale interaction: The heart of turbulence dynamics

Turbulence at high Re can be thought of as an agglomeration of different sized rotating eddies. For a pipe flows, large scales of turbulence (\mathcal{L}) scale with the fluid dynamic length scale (i.e. pipe diameter D). The smallest scale in the flow is termed as Kolmogorov's scale (η) and has universal behaviour as it depends only on the rate of loss of TKE or dissipation (ϵ) and kinematic viscosity of the fluid (ν). Needless to say that the small scales do not scale with the flow geometry. η in terms of large scale (\mathcal{L}) roughly scales as in the equation 2.2, where $Re = \mathcal{U}\mathcal{L}/\nu$. Evidently, it is very small as compared to large scale at high Re .

$$\frac{\eta}{\mathcal{L}} \simeq Re^{-3/4} \quad (2.2)$$

It is known that the turbulence is fed by the mean flow, i.e. the loss of mean kinetic energy in the flow is gain in turbulent kinetic energy (TKE). In pipe flow, pressure gradient drives the mean flow hence turbulence is fed by the pressure gradient. Turbulence extracts energy from the pressure gradient and supplies it to the large scales. Thus, large scales are energetic. The large scales then strain the smaller scales via vortex stretching and give smaller scales a fraction of their energy. This energy transfer is due to the deformation work performed on vortices by the strain rate ([1]). This can be explained for a single vortex filament as shown in figure 2.2. During vortex stretching, the length of a vortex filament increases, consequently its radius decreases due to constraint on the volume. Further, as the radius decreases its vorticity (ω_x) gets augmented to conserve the angular momentum. If ω_x increases, u' also decreases and v' and w' increase. At the same time, ω_y spins down decreasing u' and w' . The TKE which scales with the square of turbulent velocity fluctuations thus gets affected. Therefore, vortex stretching essentially redistributes turbulent energy within its components

provided there is no loss of energy due to viscous dissipation.

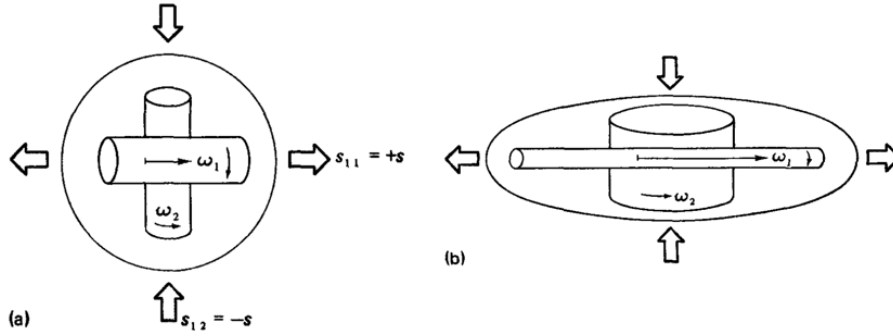


Figure 2.2: Vortex stretching in x direction, (a) before stretching (b) after stretching : strain is positive in x and negative in y or z (The image is reproduced from [1]).

The smaller scales will then strain even smaller scales as the above energy transfer continues. At the same time, small scales due to the large strain in them become dominant in vorticity (or enstrophy). As scales get smaller, gradients in the velocity fluctuations further increase and dissipation starts getting important. Taylor’s microscale (λ) is approximately the length of scale where dissipation starts becoming important (see equation 2.3). At high Re , λ is considerably small as compared to \mathcal{L} but is still larger than Kolmogorov’s length scales (η).

$$\frac{\lambda}{\mathcal{L}} \approx Re^{-1/2} \tag{2.3}$$

As turbulent scales get even smaller they can no longer sustain the strain and get dissipated by molecular or viscous dissipation. This flux of energy from the large to small scales is at the heart of turbulence dynamics and is termed as ‘energy cascade’. The time scale of this process is termed as eddy turn over time (T_E) and is equivalent to the integral time scale of the turbulence. Thus, turbulence has finite temporal scale(T_E) and

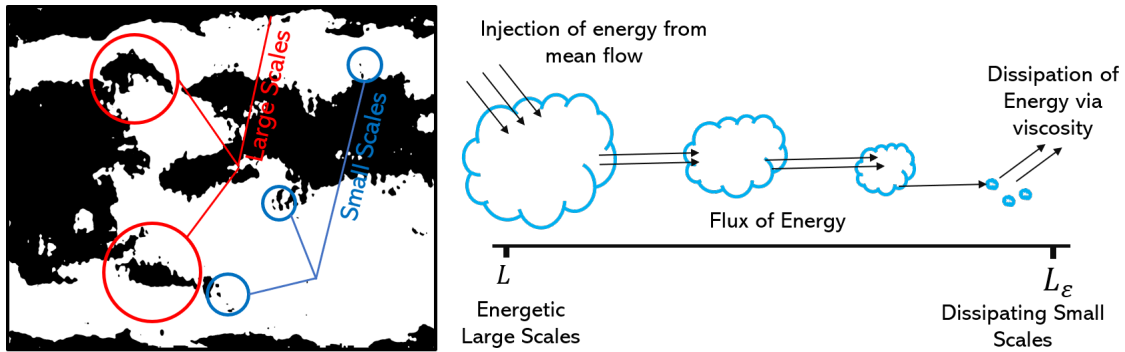


Figure 2.3: A schematic explaining energy cascading process in pipe turbulence.

length scale (\mathcal{L}). This is further manifested in statistical correlation (R_{uu}) between velocity measured at two nearby points in the flow field as a function of the distance between them as shown in the equation 2.4, where $\Delta x = x_2 - x_1$.

$$R_{uu}(\Delta x) = \frac{\overline{u'(x_1)u'(x_2)}}{\sqrt{\overline{u'^2(x_1)}}\sqrt{\overline{u'^2(x_2)}}} \tag{2.4}$$

Note that the energy spectrum is a Fourier transform of correlation function ($R_{uu}(\Delta x)$). Hence, spectral energy function ($E_{11}(k)$) as a function of wavenumber (k) can be computed analogously to power spectrum. Here,

the discrete eddies can be assumed to behave like waves defined by their wavenumber (k) which scales as the reciprocal of length scales ($k \sim 1/\mathcal{L}$). It was Kolmogorov who defined the universality of inertial and dissipative subrange in the turbulent energy spectrum. It is seen that at high enough Re , the energy spectrum function of any isotropic turbulent flow can be expressed by equation 2.5 where ϵ is turbulent energy dissipation, c is a constant.

$$E(k) = c\epsilon^{2/3} k^{-5/3} \quad (2.5)$$

The area under energy spectrum would give an estimate of turbulent energy and hence $\overline{u'^2} \sim kE(k)$, i.e., $\mathcal{U} \sim k^{-1/3}$ ($E(k)$ has been scaled using equation 2.5). If we now return to energy cascade where larger eddies impose strain (s) on smaller eddies, as mentioned before, the turbulent strain scales as ($s \sim \frac{\mathcal{U}}{\mathcal{L}}$). Thus, $s(k) \sim k^{2/3}$, i.e. smaller eddies experience larger strain rates. As a result of straining, energy is transferred to smaller eddies from larger eddies as shown in figure 2.2. However, the energy transfer depends upon the ability of the strain to align eddies such that $\overline{u'^2}$ and $\overline{v'^2}$ become different. Thus, strain essentially introduces anisotropy in the scales of turbulence. The larger eddies are strained by the mean strain and become anisotropic. However, smaller eddies have small time scales and large strain rate, hence they are less prone to become anisotropic by strains of larger eddies. This explains isotropy of small scales i.e., 'local isotropy'. The strain rate thus has to overcome the tendency of eddies to equalize its energy components. This tendency of small scales is termed as the 'return to isotropy'. The typical time scale of this return to isotropy is given by $1/s(k)$ which means that smaller eddies can get rid of strain faster and return to isotropy as compared to that of the larger scales. The above discussion is valid strictly for isotropic turbulence.

2.3. Isotropic turbulence

Homogeneous isotropic turbulence is a special type of simplified turbulence in which statistical properties of turbulence are invariant to translation, rotation and reflection [2]. Isotropic turbulence is essentially homogeneous and will be henceforth referred to as isotropic turbulence only. Isotropic turbulent structures are known to exist at small scales. At this scale, they are so scrambled that preference to any direction disappears and homogeneity appears. By definition, there is equipartition of TKE components (see equation 2.6).

$$\frac{1}{2}\overline{u'^2} = \frac{1}{2}\overline{v'^2} = \frac{1}{2}\overline{w'^2} = \frac{1}{3}k \quad (2.6)$$

where k is the total TKE. Now, correlation tensor (R) can also be simplified using the above mentioned properties. Due to invariance to reflection: $R_{ij}(r) = R_{ji}(r)$ and invariance to rotation: $R_{ij}(r) = -R_{ij}(r)$, from above relations it can be concluded that for isotropic turbulence, correlation tensor has no cross-correlation components and is symmetric. Thus, in isotropic turbulence, dissipation rate (ϵ) can be expressed in terms of single component (see equation 2.7).

$$\epsilon = \nu \overline{\left(\frac{\partial u'_i}{\partial x_j}\right)^2} = 15\nu \overline{\left(\frac{\partial u'_1}{\partial x}\right)^2} \quad (2.7)$$

Recall that when the mean strain rate is imposed on turbulence, temporary anisotropy is induced in the turbulence which will be relaxed as the mean strain gets removed due to its tendency towards equipartition and the return to isotropy. It is of interest to see how isotropy/anisotropy in Reynolds stress evolves during contraction and relaxation. There are multiple approaches to evaluate this. (i) Comparing components of normal Reynolds stress (ratio should be 1 for equipartition). (ii) Comparing $E_{11}(k)$ w.r.t. $E_{22}(k)$ as function of k . (both should coincide for every wavenumber, k for isotropy). (iii) Evaluating Reynolds stress anisotropy tensor (b_{ij}) as given by the equation 2.8.

$$b_{ij} = \frac{\overline{u'_i u'_j}}{2k} - \frac{1}{3}\delta_{ij} \quad (2.8)$$

where the first term on the right-hand side is isotropic stress, δ_{ij} is Kronecker delta function. For isotropic turbulence, all the components of b_{ij} should ideally vanish. Alternatively, Chen et.al. [24] conveniently de-

defined surrogate anisotropy tensor (b_{ij}^s) for a planar (2-D) case as their measurements were planar itself.

$$b_{ij}^s = \frac{\overline{u'_i u'_j}}{2k_s} - \frac{1}{2} \delta_{ij} \quad (2.9)$$

where

$$k_s = \frac{\overline{u' u'} + \overline{v' v'}}{2} \quad (2.10)$$

Thus by definition, $b_{11}^s = -b_{22}^s$. Due to its relevance to the current study (2-D measurements), this definition of anisotropy will be adopted in the subsequent section. Lumley and Newman [25] characterized the structure of turbulence using the second (I_2) and third invariant (I_3) of the anisotropy tensor. This analysis is used in studying return to isotropy. However, invariant analysis essentially requires all three components of velocity. Due to the lack of third component in current measurements, further discussion on this is suspended.

2.4. Turbulent scales: The measure of large and small scales

Since it is intended to study the response of mean strain on the turbulence, studying the distinct response of large and small scale is justified. Hence, it is imperative to discuss the methodologies used to quantify the above responses.

It is known that the large scales are energetic, containing most of the TKE ($\sim u'^2$) while small scales are dominated by enstrophy ($\sim \omega'^2$) or vorticity ($\sim \omega$) as also mentioned in 2.2. Typically, the large gradients in velocity fluctuations are correlated to small scales [26]. In pipe flow, large scales scale with fluid dynamic length scale. Similarly, Taylor's length scales (λ in equation 2.3) and Kolmogorov's length scale (η in equation 2.2) are indicative of small scales of turbulence. The large scale can be estimated by computing the statistical two-point correlation in space (R_{uu}, R_{vv}). R_{uu} is correlation in streamwise direction while R_{vv} is a correlation in transverse (see equation 2.11). The large scale (\mathcal{L}_{uu}) in streamwise direction is area under the R_{uu} vs Δx plot while in transverse direction (\mathcal{L}_{vv}), it is the area under R_{vv} vs Δx plot.

$$R_{uu}(\Delta x) = \frac{\overline{u'(x + \Delta x)u'(x)}}{\sqrt{\overline{u'^2(x + \Delta x)}}\sqrt{\overline{u'^2(x)}}}; \quad R_{vv}(\Delta x) = \frac{\overline{v'(x + \Delta x)v'(x)}}{\sqrt{\overline{v'^2(x + \Delta x)}}\sqrt{\overline{v'^2(x)}}} \quad (2.11)$$

$$\mathcal{L}_{uu} \sim \int_0^\infty R_{uu}(\Delta x) d\Delta x; \quad \mathcal{L}_{vv} \sim \int_0^\infty R_{vv}(\Delta x) d\Delta x \quad (2.12)$$

While it is relatively easier to resolve the large scales of turbulence, limited Spatial Dynamic Range (SDR) of measurement techniques like PIV makes it hard to resolve the small scales accurately. Hence, the approximate measure of small scales is adopted in most of the studies. For sufficiently resolved velocity data, Taylor's microscales (λ) can be estimated by fitting a parabola to R_{uu} near $\Delta x = 0$ and noting its intercept on the abscissa (Δx axis). Secondly, gradient of velocity fluctuation ($\sim (\frac{du'}{dx})^2$) which scales with turbulent energy dissipation (ϵ) can also be used to observe the effect on small scales as dissipation essentially happens at small scales of turbulence [7], [27]. Thirdly, a cut-off filter is imposed on the velocity fluctuations wherein a limit is set on u'_{cf} . u' above u'_{cf} is attributed to large scales and u' below u'_{cf} are attributed to small scales. Alternately, a sub-grid scale filter Chen et.al. [24] can be used on the velocity data but is computationally expensive. Fiskaletti et.al. [28] has shown that the region of intense vorticity corresponds to the region of turbulent energy dissipation (ϵ) which is a small-scale phenomenon. The spatial extent of small scales can thus be estimated by performing a two-point correlation on vorticity as it is dominant at small scales. The area under $R_{\omega\omega}$ vs Δx plot gives the extent of small scales. The advantage of two-point correlation is that it gives a 2-D field of correlation suggesting the shape of structures, i.e., streamwise, radial extent of turbulent structures along with orientation.

$$R_{\omega\omega}(\Delta x) = \frac{\overline{\omega'(x + \Delta x)\omega'(x)}}{\sqrt{\overline{\omega'^2(x + \Delta x)}}\sqrt{\overline{\omega'^2(x)}}} \quad (2.13)$$

$$\mathcal{L}_{\omega\omega} \sim \int_0^\infty R_{\omega\omega}(\Delta x) d\Delta x \quad (2.14)$$

2.5. Flow topology

The pipe flow is a wall-bounded flow driven by a negative pressure gradient across its length. Here, we use certain assumptions, i.e., the flow is (i) statistically steady, (ii) incompressible (fluid volume remains fairly constant), (iii) Newtonian (shear stress (τ) is linearly proportional to shear strain rate ($\frac{dU}{dy}$) via dynamic viscosity (μ)), (iv) high Reynolds number (Re). The Reynolds number (Re) is the most important non-dimensional number used to characterize the turbulent flows as mentioned before. It is defined as the ratio of inertial forces to viscous forces and is of the order of a few thousand in turbulent pipe flows. The flow under consideration is divided into three different regions viz. pre-contraction, contraction and post-contraction as shown in figure 2.4.

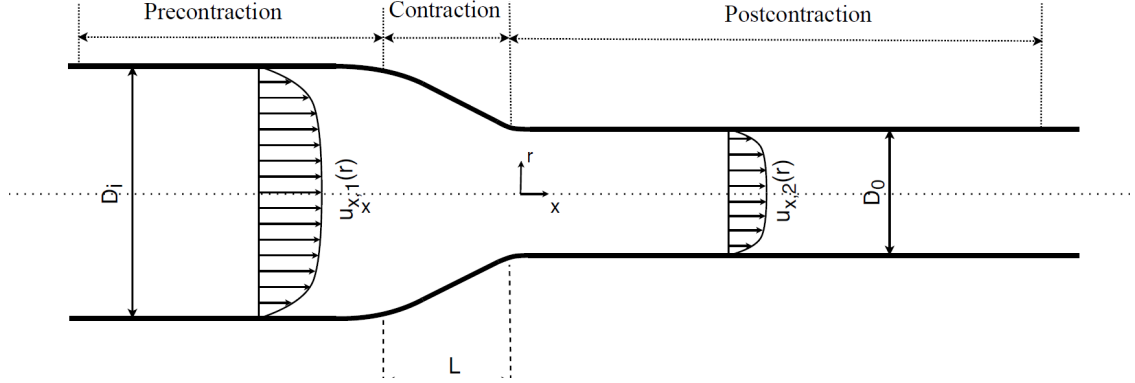


Figure 2.4: The pipe flow with axisymmetric contraction, D_i is the inlet diameter of pipe, D_0 is the outlet diameter of contraction, L is the length of the contraction, $u_{x,1}(r)$ is the fully developed velocity profile in pre-contraction region, $u_{x,2}(r)$ is the fully developed velocity profile in pre-contraction region, post-contraction.

2.6. Pre-contraction: Straight pipe

This part constitutes fully developed turbulent pipe flow with diameter D_i and bulk velocity $U_{b,1}$ defined by equation 2.15, where $\overline{u}_1(r)$ is the mean axial velocity profile as a function of radial distance r . The bulk velocity is used to define Re as mentioned above (see equation 2.15).

$$U_{b,1} = \frac{2\pi \int_0^{D_i/2} \overline{u}_{x,1}(r) r dr}{\pi D_i^2/4}; \quad Re = \frac{U_{b,1} D_i}{\nu} \quad (2.15)$$

The turbulent pipe flow when given enough length from the inlet ($\sim 40D$) will get fully developed. This means that the mean flow does not have a gradient along the axial direction ($\partial \overline{u} / \partial x = 0$). Here, turbulence is assumed to be stationary and horizontally homogeneous, i.e., for mean velocities $\partial / \partial t = 0$ and $\partial / \partial x = 0$. Further, the mean flow is axisymmetric ($\partial / \partial \theta = 0$). The driving pressure gradient acts uniformly over the whole cross-section of pipe. However, flow velocity has to be zero at the wall due to no-slip boundary conditions. Hence, mean velocity profiles get bulged in the core region and have higher gradients closer to the wall as shown in figure 2.5.

To understand this, differential equations that govern the turbulent pipe flow subject to the above assumptions are introduced. Statistically, velocity and pressure are expressed as the sum of its mean and fluctuations. Thus, velocity and pressure are expressed as $u_i = \overline{u}_i + u'_i$, $p = \overline{p} + p'$ and standard Navier Stokes equations are averaged over time to yield Reynolds Averaged Navier-Stokes (RANS) equations as also mentioned before. The continuity and the Reynolds averaged equation for mean axial velocity reduces to

$$\frac{1}{r} \frac{\partial r \overline{v}}{\partial r} = 0 \quad i.e. \quad \overline{v} = 0 \quad (2.16)$$

$$-\frac{1}{\rho} \frac{\partial \overline{P}}{\partial x} + \frac{\nu}{r} \frac{\partial}{\partial r} \left(r \frac{\partial \overline{u}}{\partial r} \right) - \frac{1}{r} \frac{\partial r \overline{u'v'}}{\partial r} = 0 \quad (2.17)$$

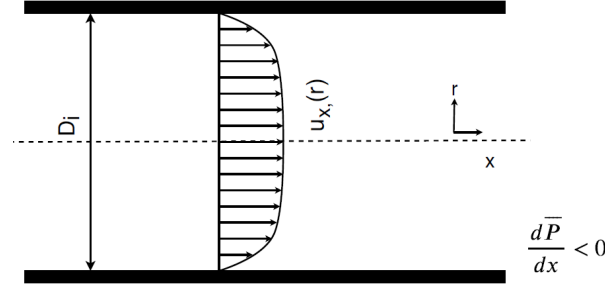


Figure 2.5: Fully developed pipe flow with velocity profile ($\overline{u_x(r)}$), diameter D_i , pressure gradient ($\frac{d\overline{P}}{dx}$).

Using gradient diffusion law, we can express Reynolds shear stress as $\overline{u'v'} = -\nu_t \frac{\partial \overline{u}}{\partial r}$, where ν_t is the turbulent kinematic viscosity, ν is the molecular kinematic viscosity, ρ is the density of fluid, r is the radial distance measured from centre of the pipe. The total shear stress (τ_t) can be expressed as a sum of turbulent shear stress and viscous shear stress.

$$\frac{\tau_t}{\rho} = -\overline{u'v'} + \nu \frac{\partial \overline{u}}{\partial r} = (\nu + \nu_t) \frac{\partial \overline{u}}{\partial r} = -\frac{r}{2\rho} \frac{\partial \overline{P}}{\partial x} \quad (2.18)$$

Since $\frac{\partial \overline{P}}{\partial x}$ is constant, net shear stress (τ_t) varies linearly with radial distance (see equation 2.18). This is one of the features of fully developed turbulent pipe flows. $\tau_t(r=R)$ is the wall shear stress (τ_w) and is extensively used in defining near wall flow (boundary layer).

$$\tau_w = -\frac{R}{2} \frac{\partial \overline{P}}{\partial x} \approx \rho u_\tau^2 \quad (2.19)$$

Since near the wall, flow is shear dominated, we define wall friction velocity (u_τ) as a velocity scale in this region. Similarly, distance from the wall (y) is expressed as wall units (y^+) where each wall unit is expressed in terms of near-wall parameters, i.e., ν and u_τ as shown by equation 2.20.

$$u_\tau = \sqrt{-\frac{1}{\rho} \frac{R}{2} \frac{\partial \overline{P}}{\partial x}} \quad ; \quad y^+ = \frac{u_\tau y}{\nu} \quad (2.20)$$

Turbulent eddy viscosity (K) is used to express turbulent shear stress in terms of velocity gradient via gradient diffusion law as mentioned above. Further, K is expressed as given by equation 2.21, where \mathcal{L} , \mathcal{U} are typical turbulent length and velocity scales.

$$K = \mathcal{L}\mathcal{U} \quad (2.21)$$

Now, according to Prandtl mixing model, \mathcal{U} can be expressed as $\mathcal{U} \sim \mathcal{L} \frac{\partial \overline{u}}{\partial r}$. Hence, eddy viscosity can be written as $\mathcal{L}^2 \frac{\partial \overline{u}}{\partial y}$, where \mathcal{L} is the length scale of turbulent eddies. In pipe flows, near the centre of the pipe, eddies are longer and near the wall, eddy size is limited by the influence of the wall [2]. Hence, fully turbulent pipe flow in radial direction can be divided into four different regions viz. viscous sublayer, buffer region, log region, core region, such that region closest to the wall is viscous sublayer and furthest from the wall is core region.

In the core region, the turbulence length scale scales with the pipe radius. Hence, mean velocity in the core region is expressed as equation 2.22 where u_0 and β are constants. This region is marked by dominant turbulent stresses over molecular diffusion.

$$\overline{u} = u_0 - \frac{2}{3} \frac{u_\tau}{\beta} \left(1 - \frac{r}{R}\right)^{3/2} \quad (2.22)$$

In the wall region, characteristic length scale of eddy (L) scales with distance from the wall, i.e., $L = ky$ (y is measured from the wall) where k is a "Von Karman" constant. The velocity profile in this region is given by equation 2.23 and is commonly known as log region. In this region, molecular diffusion is small as compared to that of turbulent diffusion and spans from $y^+ = 30 - 80$.

$$\overline{u} = \frac{u_\tau}{k} \log\left(\frac{y}{y_0}\right) \quad (2.23)$$

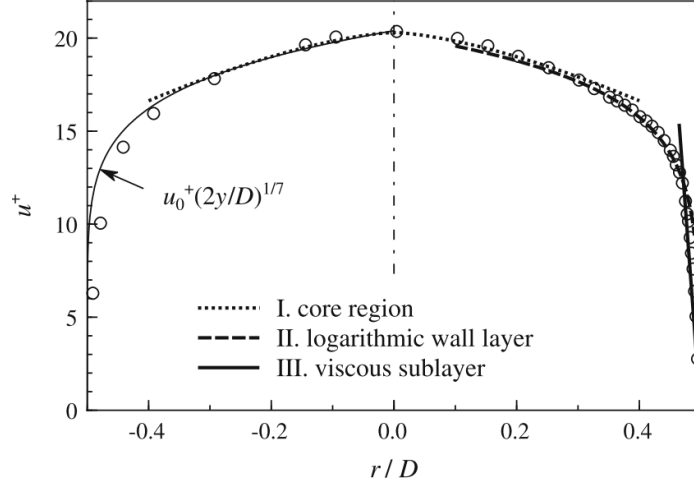


Figure 2.6: The dimensionless mean velocity profile ($u^+ = \frac{\bar{u}}{u_\tau}$) in a turbulent pipe flow as a function of r ; showing different regions as discussed above equation 2.22,2.23,2.24 (taken from [2]).

Very close to the wall, eddy viscosity scales as $K \sim k u_\tau y$ (equation 2.21). Thus, K becomes progressively small close to the wall and viscous diffusion becomes dominant. In this region velocity varies linearly as a function of wall distance and is referred to as viscous sublayer spanning from $y^+ \sim 0 - 5$. Equation 2.24 gives a mean velocity profile in this region.

$$\bar{u} = \frac{u_\tau^2 y}{\nu} \quad (2.24)$$

In between log and viscous sublayer, there also exists a buffer region where both turbulent and viscous diffusion play roles and spans from $y^+ = 5 - 30$. See figure 2.6 for the complete profile.

2.7. Contraction: The effect of axial strain on the pipe flow

The strain can be defined as the spatial gradient imposed on the mean velocity. In general, strain consists of two main components i.e. pure stretching, shear. Depending on the presence of these components a strain rate can be classified as (i) pure stretching, (ii) pure shear. In this study, we consider an axisymmetric contraction, hence, the strain rate is irrotational. Mathematically, irrotational and axisymmetric strain rate tensor (\bar{S}_{ij}) in a cartesian coordinate system can be defined by equation 2.25. Needless to say, the axisymmetry is obeyed faithfully only near the axis of the pipe.

$$\bar{S}_{ij} = \frac{d\bar{u}}{dx} \begin{pmatrix} 1 & 0 & 0 \\ 0 & -1/2 & 0 \\ 0 & 0 & -1/2 \end{pmatrix} \quad (2.25)$$

In a wall-bounded flow such as pipe flow, the strain can be imposed by the change in the cross-section area. An increase in cross-section area would impose negative mean strain in the axial direction, however, a decrease in cross-section area would lead to positive strain in the axial direction respectively. This can be achieved by a diffuser and a contraction respectively. The contraction will thus accelerate the flow due to positive strain and diffuser will decelerate the flow due to negative strain. In this research, we focus more on the contraction downstream of a straight pipe. The contraction has length L and area based contraction ratio C , where C is defined as D_i^2/D_0^2 as shown in figure 2.4.

2.7.1. The effect of axial strain on the mean flow

The contraction will act as a constriction to the flow passage, hence, an extra pressure gradient is required to push fluid through the contraction. The contraction imposes acceleration on the mean flow, hence bulk

velocity at the end of contraction will be increased by the multiple of C to satisfy mass continuity. For simplicity, if one follows a streamline from pre-contraction to contraction, Bernoulli's theorem suggests that pressure will be decreased at the end of a contraction as compared to the start of contraction. Thus, an added pressure drop is developed across the contraction. This pressure gradient is assumed to act uniformly over the cross-section of the mean velocity profile (see figure 2.6). Thus, the axial mean velocity profile gets flatter in the core. This flattening leads to the breakdown of classical log-law in the log-region of near wall flow. Due to the strain, the boundary layer close to the wall also experiences a Favorable Pressure Gradient (FPG). The severity of the pressure gradient is quantified by a non-dimensional number called acceleration parameter (K) and is defined as shown in the equation 2.26, where U_∞ is the free stream velocity in BL, ν is the kinematic viscosity of the fluid. A very severe acceleration is known to result in the relaminarization of turbulent flow. For articulation, the reader is directed to subsection 3.2.

$$K = \frac{\nu}{U_\infty^2} \frac{dU_\infty}{dx} \quad (2.26)$$

2.7.2. The effect of axial strain on turbulence

The way in which the mean strain (\bar{S}) acts on the turbulence is quite interesting. It scales with the reciprocal of time. Hence, the reciprocal of strain corresponds to the time for which mean strain acts on the turbulence. In the previous subsection 2.2, \mathcal{U} and \mathcal{L} were introduced as a typical velocity and length scales of turbulence. Thus, turbulence time scale or eddy turn over time is defined as $T_E = \frac{\mathcal{L}}{\mathcal{U}}$, which can also be expressed in terms of TKE (k) and dissipation (ϵ). It is also relevant to recall that k scales with \mathcal{U}^2 and ϵ scales as $\frac{\mathcal{U}^3}{\mathcal{L}}$. Therefore, $\frac{k}{\epsilon} \sim \frac{\mathcal{L}}{\mathcal{U}}$. The reciprocal of T_E is the strain due to large scale turbulence.

Now, if the mean strain rate ($S = d\bar{u}/dx$) imposed on the turbulence due to contraction is larger than the turbulent strain itself, turbulence does not get enough time to cascade energy from large scales to small scales. Under this condition, the strain would be termed as 'rapid'. A non-dimensional strain rate parameter is introduced (s^*) which characterises the rapidity of strain as given by the equation 2.27.

$$s^* = ST_E = \frac{Sk}{\epsilon} \quad (2.27)$$

If $s^* \gg 1$ strain rate is rapid. [7] suggests that mean strain is rapid in the true sense only when the time for which it acts on turbulence is smaller than the smallest time scale of turbulence (Kolmogorov's time scale). However, this criteria is almost impossible to satisfy in an experiment. Hence, we shall adopt the previous definition of rapid strain. Further, for this research we define surrogate non-dimensional strain rate s^{*s} (see equation 2.28), where D is the pipe diameter and $u_{c,in}$ is the centreline velocity of pre-contraction pipe flow measured at $D/2$ before the start of contraction. Note that $\frac{D}{u_{c,i}}$ is representative of eddy turn-over time (T_E), hence its usage physically is justified.

$$s^{*s} = ST_E = \frac{SD}{u_{c,i}} \quad (2.28)$$

The understanding of rapid strain rate brings us to Rapid Distortion Theory (RDT) which will be explained in the following section.

2.7.3. Rapid Distortion Theory (RDT)

This section highlights the history of rapidly strained turbulent flow and Rapid Distortion Theory (RDT). Prandtl in 1933 [3] was the first to propose that turbulence subjected to sudden contraction can remove irregularities in the flow. In his work, he derived expressions for the reduction in streamwise turbulent intensity ($\overline{u'}/U$) and increase in lateral turbulent intensity ($\overline{v'}/U, \overline{w'}/U$), assuming that strain imposed by contraction was rapid. With great insight Taylor [29], proposed that the effect of contraction on turbulence can be studied by considering its effects on vorticity. Since turbulence is a collection of vortex filaments, a single vortex filament was considered to give qualitative insight into the effects of strain on turbulence. It was assumed that velocity fluctuations in the streamwise direction (x) was due to vorticity in the directions perpendicular to x -direction (transverse directions: r, θ). Similarly, fluctuations in transverse directions (r, θ) are due to vorticity

in the streamwise direction.

For an axisymmetric contraction, when turbulence passes through it, vortex filament aligned with the direction of mean strain (x) gets stretched in x -direction by a factor of C (area based contraction ratio) and compressed in r and θ direction by a factor of $1/\sqrt{C}$ as shown in the figures 2.2, 2.7. The volume of vortex filament should be conserved hence its radius decreases in x -direction by \sqrt{C} and increases by the same factor by \sqrt{C} for vortex filaments oriented in r and θ directions. As per conservation of angular momentum, for an inviscid and incompressible flow, the strength of vortex (product of vorticity (ω) and cross-sectional area of a filament $\sim r^2$, where r is the radius of vortex filament) should remain constant.

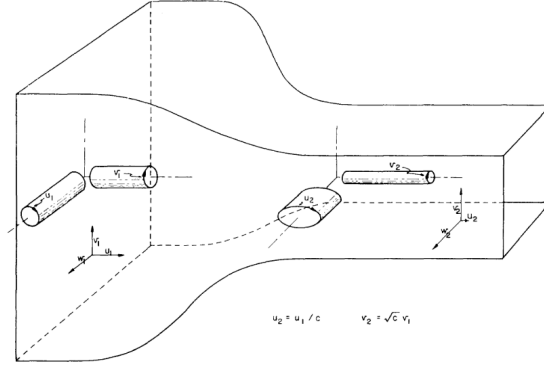


Figure 2.7: Wind tunnel with axisymmetric contraction showing vortex stretching [3].

Consequently, vorticity spins up in x -direction and spins down in other two directions. Knowing that peripheral velocity of vortex filament ($r * \omega$) is a measure of velocity fluctuation, it can be asserted that streamwise fluctuations should reduce ($1/C$) and transverse fluctuations should increase (\sqrt{C}) inside the contraction. Thus, a mutual exchange of energy is a consequence of vortex stretching. It is worthwhile to notice the similarity with the energy cascade made in the previous chapter (see figure 2.2).

Ribner and Tucker [30] and Batchelor and Proudman [4] independently recognized that the turbulence has finite spatial (\mathcal{L}) and time correlations (\mathcal{T}_E) which give rise to turbulent strain ($\frac{1}{\mathcal{T}_E}$). Thus, the mean strain rate ($S \sim \frac{d\bar{u}}{dx}$) can be superimposed on this existing turbulent strain rate(s) possibly creating larger strain. When the mean strain is rapid, i.e., time for which strain acts is much lesser than the integral time scale of turbulence (eddy turn over time, \mathcal{T}_E) ($s^* \gg 1$), then turbulence interacts strongly with the mean flow but only weakly with itself. Such small time scales do not allow turbulence to cascade energy down to the smallest eddy. Under such conditions, the effects of viscous dissipation and non-linear effects (like inertia) can be neglected. Thus, Reynolds stress equations can be linearized and simplified. Further, each Fourier mode evolves independently when these equations are pushed in Fourier space due to linearisation. This approach was first formalized by [4] and was termed as Rapid Distortion Theory (RDT). For detailed review of RDT, reader is referred to Hunt et. al. [31], Savill [32], Pope [18].

From the definition, $s^* \gg 1$ characterises rapid stain while $s^* < 1$ describes non-rapid strain. Note that strain and acceleration can be used interchangeably in this context. Under the assumption of rapid strain, scaling law : $(\frac{d\bar{u}}{dx}) \gg \frac{\mathcal{U}}{\mathcal{L}}$ holds true and governing differential equations for Reynold's stress can be simplified to equation 2.29, where $p^{(r)}$ is the rapid part of pressure fluctuations.

$$\frac{Du'_j}{Dt} = -u'_i \frac{\partial \bar{U}_j}{\partial x_i} - \frac{1}{\rho} \frac{\partial p^{(r)}}{\partial x_j} \quad (2.29)$$

[4] gave expressions for normal Reynolds stresses given by equation 2.30, 2.31, where $\overline{u_i u_i(0)}$ defines pre-contraction turbulence statistics and $\alpha^2 = 1 - C^{-3}$. See figure 2.8.

$$\frac{\overline{u'_1 u'_1}}{\overline{u'_1 u'_1(0)}} = \frac{\overline{u' u'}}{\overline{u' u'(0)}} = \frac{3}{4} C^{-2} \left[\frac{1 + \alpha^2}{2\alpha^3} \ln \frac{(1 + \alpha)}{(1 - \alpha)} - \alpha^{-2} \right] \quad (2.30)$$

$$\frac{\overline{u'_2 u'_2}}{\overline{u'_2 u'_2(0)}} = \frac{\overline{v' v'}}{\overline{v' v'(0)}} = \frac{3}{4} C + \frac{3}{4} C^{-2} \left[\frac{1}{2} \alpha^{-2} - \frac{1 - \alpha^2}{4\alpha^3} \ln \frac{(1 + \alpha)}{(1 - \alpha)} \right] \quad (2.31)$$

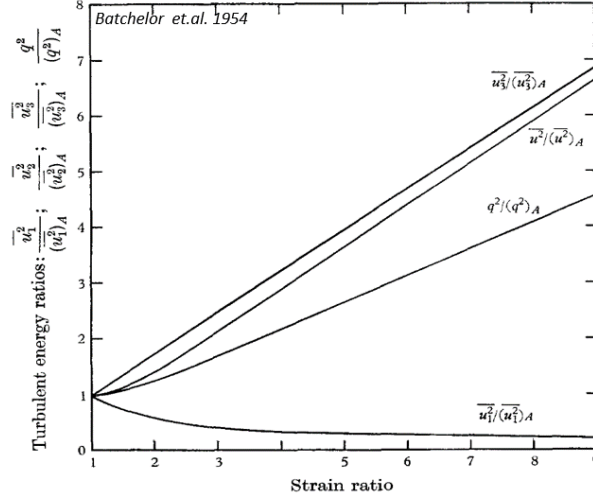


Figure 2.8: Normal Reynolds stress variation normalised with pre-contraction turbulent statistics with contraction ratio (strain ratio) predicted by RDT [4].

Similarly, the vorticity equation under the same scaling argument and assumptions reduce to equation 2.32. The term on the RHS of equation 2.32 is a vortex stretching term which is a fundamental mode of energy redistribution or transfer in turbulence dynamics (as also shown in figure 2.2).

$$\frac{D\omega}{Dt} = \omega_i \frac{\partial \overline{U}_j}{\partial x_i} = \omega_i \overline{S}_{ij} \quad (2.32)$$

Although RDT is a simple linear theory, it requires to satisfy criteria such as [4]: (i) The initial turbulent intensity should be low. (ii) Initial turbulence must be isotropic. (iii) The spatial scale of turbulence should be smaller than the spatial scale of the mean velocity gradient. (iv) The mean strain should be homogeneous within the contraction. However, there is experimental and numerical evidence of its applicability even when the above criterion is relaxed [33], suggesting its robustness. Further experimental and numerical observations made in strained turbulent flows with emphasis on RDT have been summarised in detail in chapter 3.

2.8. Post-contraction

The post-contraction region is again a straight pipe section of a smaller cross-section area depending on the contraction ratio (C). In this region, there is no mean velocity gradient in the axial direction, hence, the strain is suspended. As a result turbulence has a tendency to go back to an initial fully developed state. This being a wall bounded flow, the flow close to the wall is relaxed by boundary layer development which is reminiscent of a developing pipe flow. At sufficient distance downstream of contraction (about $40D$), flow is expected to again reach a fully developed state. However, care needs to be taken to make sure that flow does not separate post-contraction as the separated flow can introduce complex undesirable phenomena like jet flapping. In the post-contraction region, the pipe diameter is given by D_0 , $U_{b,2}$ bulk velocity of flow defined by equation 2.33, where $u_2(r)$ is the mean velocity profile as a function of radial distance r .

$$U_{b,2} = \frac{2\pi \int_0^{D_0/2} \overline{u_2(r)} r dr}{\pi D_0^2/4}; \quad Re = \frac{U_{b,2} D_0}{\nu} \quad (2.33)$$

Note that the mass continuity holds throughout the pipe flow assuming incompressibility of water. Thus, $U_{b,1}D_i^2 = U_{b,2}D_0^2$. In the core of the pipe, the response of turbulence will be different. Here, anisotropy induced in the turbulence due to the contraction will be relaxed. The large scale phenomenon is governed by the equipartition of kinetic energy and small scales phenomenon is governed by the return to isotropy. The reader is further referred to section 3.1 for details.

3

Relevant experimental and numerical observations: A literature review

This chapter contains an extensive literature review carried out before arriving at research questions. Three broad subjects are deemed important. The effect of rapid strain on turbulence is dealt with in section 3.1. The spatially accelerated wall-bounded flow is explored in section 3.2 while temporally accelerated wall-bounded turbulent flow is reported in section 3.3. This is followed by a discussion in section 3.4 leading to research objectives and questions in section 3.5. Note that the reader may directly visit Discussion (section 3.4) to avoid dense literature, where the summary of open issues is presented.

3.1. The effect of rapid strain on turbulence

This section will review the literature on the rapid straining of homogeneous turbulence and subsequent relaxation. This problem has been studied extensively in grid-generated turbulence with contraction along the centreline of a wind tunnel.

Townsend [34] performed experiments in wind tunnel where planar strain ($s^* \lesssim 2$) was imposed on a grid-generated turbulence of mesh-based Reynolds number (Re_m) ~ 5850 to 11700 via contraction of $C \sim 4$. Surprisingly, the turbulent fluctuations in all three directions (streamwise: u' , transverse: v', w') were seen to decrease along the contraction. Thus, contradicting inter-component energy transfer resultant by vortex stretching [3, 29]. It was observed that the mean strain made turbulence highly anisotropic inside the contraction. Further, it was concluded that the structure of turbulence under distortion was substantially independent of eddy interaction and the energy containing eddies of turbulence are relatively stable, slow moving structures. The presence of these stable structure was attributed to slow tendency to equipartition of energy during relaxation phase. It was also claimed that the small eddies were anisotropic and the anisotropy of small scales was not due to the anisotropy of larger scales but was due to mean strain acting on them directly. Further, small scales relaxed to isotropy faster than large scales in the post-contraction region. However, the Reynolds number (Re) in the study was limited to lower value.

Hence, Tucker and Reynolds [35] attempted to redo the experiments performed by [34], but at a higher strain rate ($C = 6, s^* \sim 2.8$) and higher Re ($\sim 10^5$). While comparing results with RDT, viscous dissipation was taken into consideration as proposed by [30]. Inside the contraction, velocity fluctuations qualitatively followed linear RDT albeit at the end of the contraction, u' was seen to increase and v' to decrease. Since there was no production of turbulence downstream, an increase in u' was attributed to the mutual transfer of energy from transverse to the streamwise component of turbulent energy. Uberoi et.al. [5, 13] extensively studied isotropic grid-generated turbulence subjected to different axisymmetric contraction of $C = 4, 9, 16$ corresponding to strain rates of ($s^* \sim 5, 20, 200$) in a wind tunnel using Hot Wire Anemometry (HWA). However, Re under consideration was limited to $14,000$. It was shown that normal Reynolds stresses qualitatively followed trend suggested by linear RDT. However, streamwise velocity fluctuations were underpredicted and transverse velocity fluctuations were overpredicted by RDT which was attributed to non-rapidity of strain rate in

this experiments resulting in the presence of turbulence-turbulence interaction neglected in linear RDT.

Uberoi and Wallis [36] and Comte Bellot [37] conducted similar experiments in wind tunnel to make grid-generated turbulence more isotropic using mild contraction ($C \sim 1.27$) downstream of grids. [36] found that the contraction resulted in equipartition of turbulent energy. However, downstream of contraction, flow had a tendency to revert to the initial anisotropic state. On the other hand, [37] found that the isotropic state achieved inside the contraction persisted even downstream of contraction. Such contrasting results instigated researchers to investigate the effects of initial turbulence anisotropy and shapes of contractions on turbulence evolution inside contraction and post-contraction. Attempts were also made to incorporate certain effects like initial anisotropy [35], inhomogeneous strain [38], initial large-scale turbulence [39] in RDT.

Hussain and Ramjee [6, 40] studied the effect of contraction ratio ($C = 11, 22, 44.5, 64, 100$) and shape on a free-stream turbulence in a circular pipe for $s^* \sim 1$ and $Re_m \sim 234$. They have reported a monotonic decrease in turbulent intensities along the centreline ($u'/u, v'/u, w'/u$) of the contraction. However, absolute turbulent fluctuations and net turbulent kinetic energy were seen to qualitatively agree with linear RDT. Further, it was shown that RDT is valid only for a small contraction ratio ($C < 4$) (see figure 3.1). Inside the contraction, normal Reynold's stress profiles remained flat for most of the radial distance. They also reported very high turbulent velocity fluctuations near the wall as compared to the core region in the post-contraction region possibly due to the severely sheared inner layer that has to re-develop as flow tries to relax back to fully developed state.

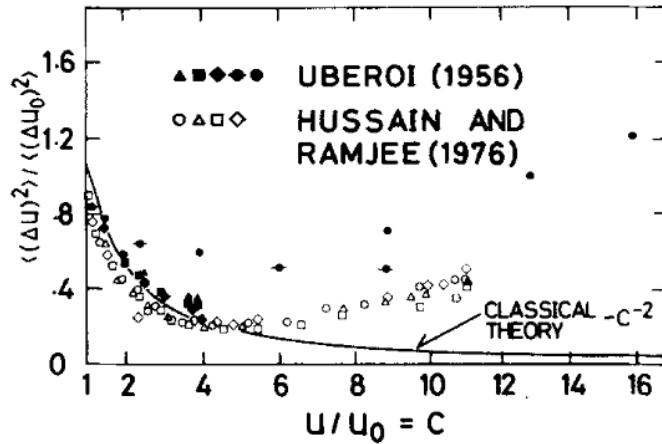


Figure 3.1: The comparison of Rapid Distortion Theory (RDT) with Uberoi et. al. [5] and Hussain et. al. [6].

Tan-atichat et.al. [41] extensively studied grid turbulence in wind tunnel subjected to axisymmetric contraction and generated ample of data for rapid strain rates $s^* \sim 5 - 7$ and $Re < 8700$ using HWA measurements. Several parameters were studied viz. $C, L/D$ ratio of contraction, Re , various pre-contraction length scales. It was asserted that if the initial grid turbulence was dominated by the small scale then longitudinal length scales grew larger than transverse scales. On the other hand, if initial turbulence was large-scaled, then transverse length scales grew bigger than longitudinal scales. Apparently, as strain rate increased, the largest streamwise length scales got smaller than for smaller strain case but transverse length scales increased monotonically with strain. It has been shown that a net increase of TKE is directly proportional to the length scale of incoming turbulence. In the short contraction (smaller L/D ratio), return to isotropy was almost perfect (based on the velocity fluctuations). Downstream of contraction, coherence between u' and v' is quite high as compared to straight section indicating that there is non-linear energy transfer between the components. This coherence is found to be stronger when initial turbulence is small-scaled. Further, the energy spectrum shows energy shifts to smaller eddies downstream of the contraction.

Ertunc and Durst [14, 42] have showed the validity of RDT even with large strains. They performed experiments in a wind tunnel with axisymmetric contraction ($C = 4, 15$), ($s^* \sim 1 - 70$). The experiments were per-

formed at low Re ($\sim 15-50$). At high s^* , it was observed in previous studies [5, 13, 35, 41] that streamwise component of velocity fluctuations u' decreases inside the contraction and then increases in post-contraction region. However, RDT predicts monotonous decrease of u' . Upon investigation, the contamination in turbulent statistics were contributed to; (i) Fluctuations in mass flow rate which could occur due to vibrations in pump and can amplify downstream as turbulence is strained. (ii) Electronic noise in measurement system (HWA) and (iii) Limited length of the probe wire which could be insufficient to resolve the flow structures undergoing shrinkage in transverse and lateral direction. Once these contaminations were removed normal stresses were seen to agree well with RDT even at high contraction ratio ($C = 14$).

Along with experimentalists, the problem of rapidly strained turbulence has also received generous attention from numerical fluid dynamists and applied mathematicians. Tsuge [43] asserted that Uberoi's [5] results for turbulent fluctuations in post-contraction region at high contraction ratio were erroneous because of uncontrolled acoustic noise in the tunnel. Apparently, the agreement of [5] with RDT was better due to incoming small scales and low-intensity turbulence. However, in [6] agreement with RDT is not good due to non-rapidity of mean strain and low Reynolds number (see figure 3.1).

As opposed to wind tunnel experiments, Hultgren et.al. [44] performed numerical simulations of pipe flow with different contractions ($C = 1.25, 2, 4$). The results for normal Reynolds stress qualitatively matched with RDT. The Reynolds shear stress ($u'v'$) is seen to increase with C along the radial direction. Thus, the correlation between streamwise and radial velocity fluctuations were seen to increase with C . Furthermore, it was seen that post contraction, 1-D energy spectrum in streamwise direction $E_{11}(k)$ shifts right (to smaller scales) and radial spectrum $E_{22}(k)$ shifts leftwards (towards larger scales) as also seen by [41]. Lee [27] performed DNS to study the effect of very rapid strain ($s^* \sim 35$) on homogeneous turbulence. Turbulence was seen to reduce to two-component state inside the contraction, also referred to as disk-shaped turbulence as given by Anisotropy Invariant Map (AIM) of Lumley [25]. It was observed from simulation results that vorticity (or enstrophy) increases inside the contraction ($\omega'^2 \sim C^2$). The anisotropy of turbulent scales based on b_{ij} were seen to match well with RDT predictions. Thus, it was claimed that RDT should be valid for $C > 4$. Also, anisotropy tensor for vorticity and Reynolds stress were plotted individually to study the effect of strain on small scales and large scales respectively. The former was seen to increase before later suggesting small scales respond faster to the applied strain.

Zusi and Perot [45, 46] performed DNS to study the effect of axisymmetric and plane strain on isotropic turbulence and successive relaxation to isotropy. The Re used were rather small and non-dimensional strain (s^*) was limited to 3.5. The return to isotropy is hypothesized to take place in two stages viz. recovery and return. The recovery is immediately after the strain has been removed where anisotropy is seen to increase and assume a peak. But during the slow return phase, it starts relaxing back to isotropy. This recovery phase is not taken into consideration for various return to isotropy models leading to the modeling errors. Kida and Hunt [47] performed theoretical studies to study the interaction between turbulent scales and the interaction of turbulence with mean flow. It was seen via anisotropy tensor that anisotropy of small scales decrease when turbulence is subjected to rapid strain much in contradiction with previous findings [5, 27, 41, 43, 44]. It was reported that small isotropic scales interact with large scale anisotropic eddies and small eddies get preferentially stretched in the direction parallel to the domain boundary (pipe walls in pipe flow). Thus, large anisotropic scales make small scales more anisotropic suggesting that small scales have a memory of large scales.

Chen et. al.[24] studied turbulence subjected to a cycle of planar straining and de-straining in a water tunnel via particle image velocimetry (PIV). The Reynolds number Re_λ used in the experiments was ($Re_\lambda = 400$) and s^* varied from 0 to 9.5. The measurements inside the strained region showed that streamwise fluctuations decrease and lateral fluctuations increase. The anisotropy tensor qualitatively matched with RDT predictions but over-predicts it. When production term P_{ij} is plotted along the distorted section, it is found that kinetic energy is indeed given to turbulence by mean flow during straining although during de-straining backscattering of energy takes place from turbulence to mean flow as predicted by RDT. The Sub-Grid-Scale (SGS) model was used to study the effect of distortion on three different scale sizes: 25η , 50η and 100η where η is Kolmogorov's length scale. Anisotropy is seen to increase with the filter scale as seen by Lee [27, 43]. Also, the small scales were seen to respond faster than larger scales to the applied strain.

Non-linear interaction of scales downstream of contraction as mentioned in the theoretical work of Kevlahan and Hunt [33] has been observed experimentally by Ayyalasomayajula et.al. [7]. Experiments like [5] were performed but at higher Re ($Re_\lambda = 40 - 470$) and strain rate (s^*) of 10. It was seen that the longitudinal eddies get suppressed and transverse eddies get amplified as flow approached contraction. The longitudinal energy ($kE_{ii}(k)$) has same magnitude of energy as predicted by RDT albeit peak in energy is shifted to smaller scales (high wavenumber). At the same time transverse energy is overpredicted by RDT but peaks at same wavenumber. It may be important to note that RDT predicts same peak for both components of energy. This shift of peak is more prominent at higher Re . The mismatch in transverse energy is attributed to the acoustic noise in hot wire measurements which ideally can be exacerbated with measurements in water tunnel/pipe. On the other hand, mismatch in longitudinal energy was attributed to non-rapidness of strain and thus non-linear scale interaction. The magnitudes of dissipation spectrum $k^2 E_{11}(k)$ and $k^2 E_{22}(k)$ are similar indicating small scales have returned to isotropy faster than large scales. The ratio E_{11}/E_{22} plotted against wavenumber (k) provides an estimate of length scales (k) affected by mean strain. Evidently, higher strain rate can affect or strain higher wavenumber eddies (small eddies). [33] performed scaling analysis to estimate the scale of K_s up to which the mean strain has its effect. Thus, higher s^* is capable of inducing anisotropy even at smaller scales, where K_η is Kolmogorov's wavenumber.

$$\frac{K_s}{K_\eta} \sim s^{*3/2} Re_\lambda^{-3/2} \quad (3.1)$$

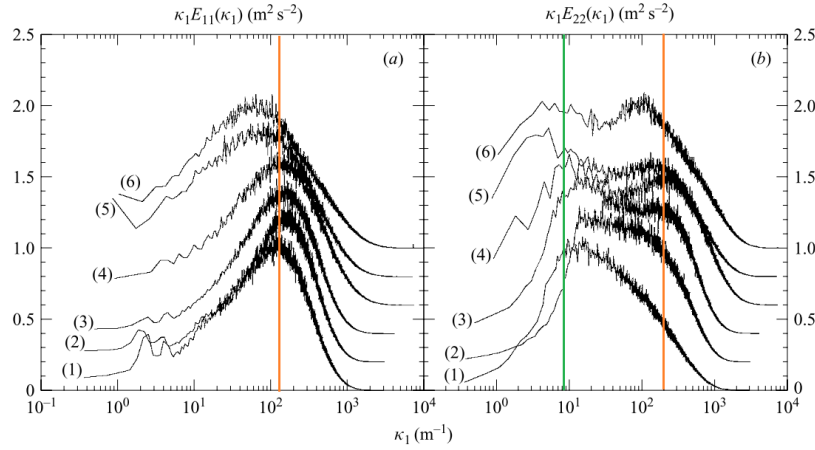


Figure 3.2: Peak shifting in $E_{11}(k)$ and second peak occurrence in $E_{22}(k)$ reported in [7]; (1)-(6) corresponds to disparate grids and Re cases examined. (6) being the largest $Re_\lambda \sim 470$.

As turbulence is relaxed downstream of the contraction, energy in longitudinal direction is seen to increase and decreases in transverse direction. There is a shift of peak for longitudinal energy as seen before which gets bigger with higher Re (see figure 3.2). Surprisingly, transverse spectrum is seen to broaden and has a faint second peak at the same wavenumber as the peak of longitudinal spectrum. This peak is seen to get more prominent at higher Re indicating that there is a complex, non-linear interplay of scales during relaxation. It can be assumed that this interaction is due to the distinct response of different scales to the applied strain, i.e., small scales respond faster to the strain and relax back faster once strain is removed as compared to larger scales. Clay et.al. [48] tried to recreate the above experimental results [7] using DNS to discern the mechanisms behind peak shifting and second peak but at slightly low Re_λ . Here, pressure fluctuation terms were deemed most relevant as also reported by [49]. It was concluded that slow pressure strain neglected in RDT is responsible for peak shift as observed by [7].

Most of the studies on accelerated turbulence were performed in a wind tunnel. Moreover, these studies focused only in the core region with little to no attention to near wall region. Jang et.al. [8] performed experiments and DNS simulation in air pipe ($D = 186\text{mm}$) to study the effect of contraction ($C \sim 2, 4, 8$) on fully developed turbulent flow. The profile of contraction was designed such that mean strain is constant in contraction ($s^* \lesssim 3$). The Re in the experiments were limited to 35,000. Inside the contraction, u' profile showed a steep peak near the wall and decrease in core region. This peak got stronger and shifted towards the wall

with the increase in Re due to thinning boundary layer upon acceleration. Other components (v' and w') were seen to increase in the core region of the pipe. At low C , net production of turbulent kinetic energy was not appreciable due to the fact that net gain in radial and azimuthal direction was not as much as net loss of energy by axial component. The energy partition factor (K^*) is defined as suggested by [34] and is used as a measure of anisotropy.

$$K^* = \frac{2\overline{u'^2}}{\overline{v'^2} + \overline{w'^2}} \quad (3.2)$$

In the straight section, K^* was close to 1 suggesting near isotropy. However, in contraction, K^* drops below 1 indicating a mutual transfer of energy between the components. The budget analysis for normal turbulent stresses reveal that the convection term becomes the dominant production term for u' and production terms acts as a sink term. On the other hand, for v' , production term act as source and convection terms as sink. It shows that several contraction pushes turbulence towards two-state turbulence, i.e., disk shaped in the sense that radial and azimuthal stresses become equal and are greater than streamwise stresses. For small C (~ 2), turbulence state is seen to move close to cusp of AIM indicating that mild contraction can push turbulence towards isotropy [50].

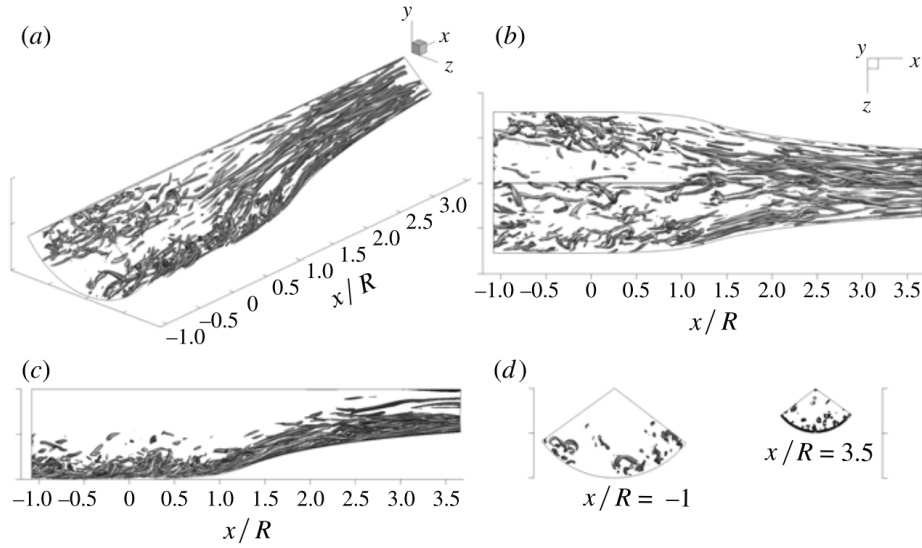


Figure 3.3: Stretching of turbulence structure due to axial strain [8].

The DNS provided unprecedented insight into the turbulence structure. The visualization of swirling strength showed that vortical structures are indeed elongated due to mean strain. The structures were aligned with the mean flow and some were pushed towards the center (see figure 3.3). Chong et.al. [51], Adrian [52] have stated that production of Reynolds stress is related to the ejection and sweep events. Hence, joint pdf of $\overline{u'v'}$ is plotted and seen where it has maximum. This gives event vector where turbulent stresses are produced. It is seen that event vector does not change much with Re but increases with contraction ratio thus proving that radial turbulent stress increases in the core region but Reynolds shear stress does not change much. It turns out that the mean strain transforms the hairpin vortex into double roller eddies in inner and outer regions.

Moene [53] has reported the effect of mildly rapid axial strain ($s^* \lesssim 3$) on turbulence in water pipe flow. By far, this is the only experimental study performed in strained water pipe flows. The measurements have been performed for two Re , i.e., 20,000 and 100,000 using LDA and numerical simulations were done by LES. The experimental data is presented only at post-contraction axial positions of pipe ($z/D = 2.4, 6.9, 11.4, 25.2$), where D is the initial pipe diameter (70mm) albeit no measurements are reported inside the contraction. The contraction resulted in the flattening of mean axial velocity profiles and sharp gradients in the near wall region. The profiles of Reynolds stresses show that it stays almost uniform having very low values as acceleration suppressed turbulence. As the flow relaxed downstream, the region of low turbulence intensity in core

region vanished and peak of $\overline{u'^2}$ shifts away from the wall. The transverse components $\overline{v'^2}$, $\overline{w'^2}$ showed a similar response in the core region. The relaxation process is essentially characterised by the development of TBL. It is seen that for small Re , relaxation takes place faster as it is governed by growth of BL (Blasius's correlation: $\frac{d\delta}{dx} \sim Re^{-0.25}$, where δ is the BL thickness). It is seen that the anisotropy decreases inside the contraction and then starts increasing further downstream. This qualitatively is in agreement with RDT. It is seen that for the most bit, turbulence is axisymmetric (cigar shaped anisotropy) and is closer to isotropy near the axis of pipe. The integral length scales obtained based on autocorrelation function show increase in radial length scales and decrease in axial length scales as predicted by RDT (near the centreline) in the post-contraction region. Further, near the wall ($r/R = 0.9$) L_{zz} increases and L_{rr} decreases along the axial direction. At $z/D = 40$, mean properties and normal Reynolds stresses returned to the fully developed state but not turbulent shear stress.

3.2. Spatially accelerated wall-bounded Turbulence

The majority of literature discussed above (except [8], [53]) report measurements only in the core region of wind tunnel (channel) with little emphasis on near-wall effects. RDT seems to predict turbulence evolution qualitatively well if not quantitatively in the core region of the pipe as evident from only two available studies [8, 53]. However, the pipe flow being wall-bounded, it was deemed crucial to review the effect of the Favourable Pressure Gradient (FPG) on TBL.

The study of BL subjected to acceleration has been carried out in wall-bounded flows like channel flows, wedge flows in the past and it was found that near wall and core-region turbulent structures respond distinctly to the acceleration. The mean velocity gradient due to the acceleration ($\frac{d\bar{u}}{dx}$) creates a Favourable Pressure Gradient (FPG) ($\frac{d\bar{P}}{dx}$) across the BL. An important non-dimensional number acceleration factor (K) or pressure gradient factor is identified and defined by equation 3.3, where ν and ρ is kinematic viscosity and density of the fluid respectively. It (K) quantifies the severity of the acceleration and scales directly with the mean strain.

$$K = -\frac{\nu}{\rho U_\infty^3} \frac{d\bar{P}}{dx} = \frac{\nu}{U_\infty^2} \frac{dU_\infty}{dx} \quad (3.3)$$

One of the most fascinating features of such a flow is that when K approached a critical value, TBL responds in a distinct manner to the imposed acceleration. Below K_{cr} , TBL is seen to become thinner. However, above K_{cr} , the BL was seen to relaminarise [54]. The laminarisation was a result of the domination of pressure forces over slowly responding Reynolds stresses. It is important to realise that the strain rate (s^*) and acceleration parameter (K) directly scale with each other. Hence, rapid mean strain in the wall-bounded pipe flow can potentially relaminarise the BL. However, literature focusing on the combined effects of rapid strain (s^*) and K together has not been identified.

Lauder et.al. [54] studied pipe flow subjected to FPG. However, he measured only the streamwise component of mean velocity (\bar{u}) and streamwise turbulence statistics (u'). It was reported that during relaminarization, streamwise fluctuations $u'/u(x)$ decreased exponentially and its spectrum showed complete similarity along the pipe axis. Badrinarayana [55] performed similar studies in a 2-D channel flow at low Re ($\sim 625 - 1250$). It was seen that as the flow evolved downstream, $\frac{u'}{u(x)}$ decreased and its peak close to the wall shifted away from the wall. This was the effect of the growth of the viscous sublayer due to relaminarization. Turbulent intensities when plotted along the axis of channel showed decay and this decay rate decreased as Re increased. The energy spectrum ($E_{11}(k)$) at the centreline, when normalised with mean velocity showed no change during the decay process. This can be partly due to near similarity in $u'/u(x)$ and $v'/u(x)$. The budget of TKE revealed that the production and advection contribution is balanced by the viscous dissipation during acceleration, which is implicitly supported by a decrease in turbulent quantities.

Patel et.al. [56] defined more non-dimensional parameters such as Δp (equation 3.4) and $\Delta \tau$ (equation 3.5) that showed severity of FPG on a BL (for pipe flow, $\Delta p = 2$, $\Delta \tau = -\frac{4}{Re} (\frac{2}{c_f})^{1/2}$). Δp is the pressure gradient parameter, $\Delta \tau$ is shear stress gradient parameter, u_τ is typical friction velocity and $\frac{\nu}{u_\tau}$ is typical length scale of viscous region, α is the gradient of shear stress in wall region ($\tau(y) = \tau_w + \alpha y$).

$$\Delta p = \frac{\nu}{\rho u_\tau^3} \frac{dP}{dx} \quad (3.4)$$

$$\Delta\tau = -\frac{\nu}{\rho u_\tau^3} \alpha \quad (3.5)$$

The experiments were performed in a pipe with centerbody to induce FPG. Re_θ decreased during the acceleration ($Re \lesssim 6000$) and Δp was varied from 0 to 0.03. The final Re was below the turbulent Re limit. As the flow was accelerated, the mean velocity profiles were seen to approach laminar like parabolic profiles. Further downstream, when FPG was suspended and Re increased, the new fully developed turbulent flow was formed. This criteria for reverse transition in 2D boundary layer flow can be extended to axisymmetric pipe flows too. Using argument that $c_f \sim Re^{-1/4}$ (after Blasius), it can be shown that $\Delta p \sim Re^{-7/8}$, hence, as Re increased, Δp and $\Delta\tau$ goes down. Thus, the effect of FPG is expected to reduce with increasing Re . It was attempted to prove that relaminarisation was not due to the reduction of Re because in the pipe flow, hysteresis does not hold, i.e., if Re is reduced, the transition cannot be expected to occur at same Re if Re was steadily ramped.

Narayanan and Ramjee [57] conducted extensive experiments involving 2D incompressible turbulent boundary layers accelerated by a wedge. They evaluated seven different flow geometries; the first six involved reduction in Reynolds number (set1) while in the last, Re increased with acceleration (set2). It was interesting to note that relaminarisation occurred in set1 experiments but not in set2. The mean velocity profiles showed that highly accelerated profiles are similar to the laminar velocity profiles. These laminar like profiles start developing near the wall and then propagate towards the centre. In the set2 experiment, velocity profiles do not show a tendency towards laminar profiles. In set1, $\frac{u'}{U_\infty}$ showed marked decrease with axial distance, however, set2 showed no difference in $\frac{u'}{U_\infty}$ as flow proceeded downstream. In set1, log-law broke down due to the thickening of the viscous sublayer. It was suspected that this reverse transition is due to low Re (as low as 400) as also reported by [54]. Along the axis, turbulent intensity along with other stresses (v' and $\overline{u'v'}$) was seen to decrease suggesting relaminarisation. It is found that during the reverse transition, three events occur viz. (i) Disappearance of large eddies in BL (ceasing of turbulent bursts), (ii) The breakdown of log-law and (iii) The decay of turbulent fields. Further, these events were characterized by K , Δp and Re respectively.

Narasimha and Sreenivasan [9] divided this problem into four different regimes viz. Initial fully developed, reversion, quasi-laminar, new fully developed turbulence and studied it separately. See figure 3.4.

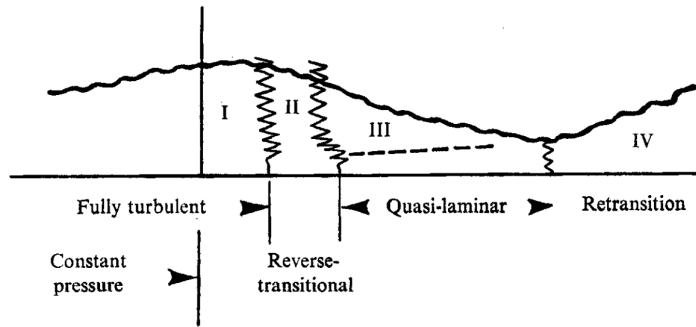


Figure 3.4: Different regimes in accelerated boundary layer [9].

In the reversion region, Reynolds stress was constant, which can be related to the 'stress freezing' as also reported by [58]. As far as turbulence structure was concerned, it was found that u' in the quasi-laminar region is inherited from the previous TBL (frequency scaling matched with energy spectrum), suggesting a delayed response of turbulence to the acceleration. In the core region, RDT could be used to predict u' and v' [8, 9]. Also, on the outer edge of BL, kinetic energy increased as predicted by RDT. However, RDT is less successful in predicting the behavior of v' in the core region mainly due to the vast difference in the size of turbulence scales.

Blackwelder [58] performed experiment in channel flow with the wedge. K was varied from 0 to 4×10^{-6} and Re_θ dropped from 2500-900. Relaminarization was observed with turbulent intensities dropping in the streamwise direction although the absolute value of fluctuations (u' , v') remained nearly constant or showed

a slight increase along the axis of the channel. From the space-time correlation contours it seemed that acceleration has little effect on the large scales in the streamwise direction, however, in the spanwise direction, the correlation was narrowed down. Thus, turbulent structures were modified under acceleration.

[59] performed experiment in parallel plate where acceleration was imposed on TBL using convergent plates at $Re \sim 10,000$ and $K = 8 \times 10^{-6}$. The severely accelerated mean velocity profiles showed overshoot in the near-wall region and flattened behavior in the core region (w.r.t. universal profile: u^+ vs y^+). Thus, log-law broke down (as reported also by [54, 57, 58, 60]). As flow entered the second constant cross-section, post-contraction, it was seen that the viscous sublayer grew thicker for some streamwise distance and then showed a trend towards fully turbulent flow. u' exhibit a sharp increase just after the contraction and then decreased. The energy spectrum showed that large disturbances were produced in the near-wall region that propagate in the core and wall region with some delay. These large structures were not distributed evenly but appeared in groups suggesting the presence of puffs.

Piomelli et. al. [61] numerically studied the effect of acceleration on BL using Large Eddy Simulation (LES) approach. Two geometries were simulated; case 1: ($K < K_{critical}$) and case 2: ($K > K_{critical}$). As the flow accelerated, turbulence was seen to lag w.r.t. the mean quantities. More importantly, structural parameter $a_1 = \frac{\overline{u'v'}}{u'_i v'_i}$, which measures the efficiency with which turbulence extracts Reynolds stress from available kinetic energy decreased significantly in the near-wall region. The BL streaks in strongly accelerated turbulence became more ordered, longer and stable. The stability of streaks was linked to the reduction of turbulent bursts in BL. The velocity fluctuations at the centre remained the same or increased slightly in the streamwise direction as also reported by [6, 56, 58, 59]. This was evident from streaks becoming more stronger. Near the wall, there is a substantial difference in u' and v' such that $\frac{u'}{v'}$ is large (due to the shear layers at the edges of streaks) and at the core, it is almost 1. Thus, two regions are affected distinctly. Local vorticity appeared to be smaller downstream than upstream in spite of expected vortex stretching during acceleration. It is seen that in accelerated flows, the density of coherent structures decreased due to stretching of vortices which can result in smaller eddies that can be dissipated by viscosity. This is followed by the reduction in turbulent burst and no production in turbulence. No difference between the coherent eddies upstream and downstream suggests some kind of equilibrium between viscous dissipation and vortex stretching.

Bourassa et.al. [62] studied the effect of acceleration in a wind tunnel with contraction ($C = 4$) and $Re_\theta \lesssim 4600$. The contraction was designed to ensure $K > 3 \times 10^{-6}$. Hence, the emphasis was on relaminarisation of BL. A delay was observed between the acceleration and response of Reynolds stresses. It was seen that $\overline{u'^2}$ showed dual-layer behaviour, i.e, for $y^+ < 100$, $\overline{u'^2}$ increases with x while in the core region $\overline{u'^2}$ decreased separated by a boundary appearing at $y^+ = 150$ as also reported by [8]. The decay was large in the centre and the peak of $\frac{\overline{u'^2}}{u_\tau^2}$ shifted away from the wall as the flow got accelerated. $\overline{v'^2}$, showed similar dual-layer behavior. Reynolds stress was seen to decrease entirely in the wall-normal direction. Apparently, the peak of production term in spanwise direction shifted few wall units away from the position where it initially had a peak (upstream of contraction). It was seen that turbulence production ($P_{tot} = p_{tot} = \overline{u'v' \frac{du}{dy}}$) does not scale with u_τ due to the lag between Reynolds stress and local mean strains i.e. $\frac{d\overline{u}}{dy}$ change faster than Reynolds stress ($\overline{u'v'}$).

The core region is almost passive to the turbulence production. Several conditional measurements near the wall have been performed to get insight into near-wall dynamics under the effect of acceleration. The quadrant splitting analysis has been carried out where Q2 events are related to the ejection of low momentum fluid away from the wall, Q4 events are related to sweep events (down-draft of a convecting hairpin packet sweeping high-momentum fluid towards the wall). The presence of these events signifies the production of turbulent stresses in the near-wall region. Due to the acceleration and subsequent thinning of BL, these events were found to be suppressed. It was seen that Q4 events completely ceased, however, Q2 events were still active even during relaminarization.

3.3. Temporally accelerated wall-bounded flows

An alternate means of imposing mean acceleration on a wall-bounded flow is by transiently varying the bulk mass flow rate. The literature contains studies on ramp type acceleration (relatively less rapid acceleration) and step type acceleration where rapid acceleration is imposed on wall-bounded flows viz; pipe and channel flow. It was proposed by He and Jackson [63] that the wall-bounded flows when subjected to temporal acceleration showed similar behaviour as that of a spatially accelerated BL discussed in 3.2. Transient acceleration causes thin layers close to the wall to shear. This shear then diffuses into the flow forming time developing BL, causing further changes to turbulent structures. The similarity between spatially accelerated and temporally accelerated turbulence can be drawn w.r.t. the convection velocity scale ($x \approx U_{cont} t$). Hence, such studies are deemed relevant for the current research and worth reviewing.

He et. al. [63] studied the effect of transient acceleration on a fully turbulent pipe with an inner diameter of 50mm. The measurements were performed using Laser Doppler Anemometer (LDA) at $Re \approx 35,000$. In this study, the ramp parameter (γ) is used as a non-dimensional parameter which determines the extent to which ramped flow departs from the pseudo steady flows at corresponding Re . $\gamma \geq 1$ ensures rapid acceleration. This parameter is physically equivalent to the acceleration parameter (K) defined before.

$$\gamma = \frac{D^3}{\nu^2} \frac{dU_b}{dt} \quad (3.6)$$

where D is the pipe diameter, ν is kinematic viscosity, U_b is bulk velocity. The other relevant non-dimensional groups are initial (Re_0) (pre-excursion) and final Reynolds number (Re_i) (post-excursion). [63], in their experiment, maintained $\gamma \sim 6.1$. Similar to spatially accelerated wall-bounded flows, temporally accelerated flows showed dual-layer behaviour. In the core region, mean velocity was lower while it was higher in wall region (w.r.t. pseudo steady state flow). Also, mean velocity profiles flattened in the core region in the initial phase of acceleration, later as time progressed, profiles were seen to match pseudo-steady profiles. The turbulent velocity fluctuations (u' and v') were either constant or increased slowly along the pipe axis. However, it can be seen that after a delay, it increased more rapidly to catch up with steady state. This delayed response of turbulence to acceleration is a signature of accelerated wall-bounded flows [64]. Further, this delay is less in near wall region and relatively fixed. However, in the core region, this delay increases and scales with distance from the wall. Moreover, this delay gets reduced with decreasing rapidness of acceleration. It seems that delayed response originates in the buffer region and then propagates towards the wall via viscous diffusion and in the core region via turbulent diffusion. The near-wall turbulence structures of u' , v' , w' shows distinct behaviour. The delay in v' and w' is higher than u' and there is a rapid upsurge of v' , w' . This could be because u' extract energy directly from the mean flow and redistributes to v' , w' via pressure strain redistribution. It is interesting to note that this time delay can give an estimate of time scales of energy redistribution.

The turbulent velocity fluctuations when normalised with mean velocities show that turbulent intensities ($\frac{u'}{u}$, $\frac{v'}{u}$) get attenuated during acceleration due to delayed response of turbulence. The Reynolds shear stress ($u'v'$) shows similar kinds of delays. However, unlike normal stresses, shear stress stays almost constant during the delay period. It shows upsurge only after the delay. It is seen that velocity profiles respond quickly to the acceleration but Reynolds shear stress responds slowly hence the production of turbulence is delayed. This can be associated with turbulent bursting frequency. Thus, turbulence will not respond until the next turbulent burst has taken place. It has been shown that the delay is a function of an initial Re_0 . Hence, higher Re_0 results in smaller delays. During the developing stage (just after the delay), the history of flow is forgotten and turbulent fields act similar irrespective of Re_0 , provided the acceleration is same. [65] studied turbulence subjected to linear ramp in channel flow. Three different regimes were identified w.r.t. the flow rate excursion (acceleration): pre-transition, transition and relaxation. During pre-transition, u' increases rapidly but v' , w' , $\overline{u'v'}$ stays constant. During transition, v' , w' along with shear stress ($\overline{u'v'}$) increases, further, u' peaks and then decreases. This is due to redistribution of energy from u' to v' , w' .

For a step type acceleration, the response of turbulence, however, is like bypass transition from laminar to turbulent even though the initial flow is turbulent. Greenblat et. al. [66] performed experiments in 48mm pipe with high $Re \sim 35,000 - 82,000$ and rapid acceleration using single component LDA. Three different

non-dimensional parameters have been considered. viz.

$$p^+ = -\frac{\nu}{\rho U_\tau^3} \frac{dP}{dx}; \quad K = -\frac{\nu}{\rho U^3} \frac{dP}{dx}; \quad \lambda = -\frac{a}{\tau_w} \frac{dP}{dx} \quad (3.7)$$

where

$$\rho \frac{du}{dt} = -\frac{dP}{dx} \quad (3.8)$$

Further, three different cases were studied such that first maintains local equilibrium, the second involves a breakdown of local equilibrium and the third is with BL relaminarisation. Four different regimes were identified: (i) steady flow (ii) Initial phase (iii) Final phase (iv) Relaxation phase. During the final phase, while acceleration diminishes, the velocity fluctuation profile is seen to develop unusually. The turbulence production begins in the core region and moves towards the wall (this is not seen in case(iii)). At the same time, the turbulence production in the near-wall region increases. Thus, u' shows a profile with a peak close to the wall which goes closer to the wall with the development of turbulence (closest measurement location was $y^+ \sim 12$). It was maintained that the delay in turbulence regeneration increased with the acceleration rate. The post-generation turbulence propagation rate was the same for all the cases. The peak in turbulent fluctuations (u') shifts towards the wall in case (i) and (ii) while for case (iii), it shifts away from the wall with time. At the end of the excursion, the peak is at the same location for all the cases ($y^+ \sim 130$) but the turbulence was still not fully developed.

[10] addressed the varying ratio of final to initial Re during a step change with DNS. Two broad approaches were taken. In the first, final Reynolds number (based on bulk velocity and half-height of the channel) (Re_1) is fixed to 7400 but initial Reynolds number (Re_0) is varied from 2800 – 5300. In the second approach, R_0 is fixed (2800) and Re_1 is varied from 3100 – 12600. The result of high Re ratio will be discussed in detail here. During initial acceleration, long streaks are seen in the boundary layer and number of hairpin vortices seem to decrease. However, new vortical structures start appearing indicating the generation of turbulent spots and hence the onset of transition.

As time progressed, these turbulence spots grow to occupy more spaces, joining each other until it fills the majority of flow. The profile of u' shows a rapid increase in the near-wall peak values and slow change later. The rapid increase is related to the enhancement of streaky structures. On the other hand, v' and w' does not change much pre-transition but increases when the transition happens. v' is seen to remain constant or decrease slightly for the most part but later increases as reported by [65]. He et.al. [67] extended his DNS study in channel flow (step acceleration) to pipe flows. Apparently, channel flows and pipe flows behave very similar in the wall region ($y^+ \lesssim 12$) but the behavior is different in the core region. The flow Re is ramped from 2600 to 7300 in time small enough to consider it as a step change. The time separation ($\delta t = \frac{tU_0}{r} = 0.22$) is smaller than the integral time scale ($\delta t \sim 0.9$). Hence the acceleration is rapid. The response of turbulence is bypass transition from laminar to turbulent like in channel flow [65]. The large scales perturbations penetrate into laminar boundary layer and produce high and low speed elongated streaks stabilising the BL. Downstream, turbulent spots grow and evolve increasingly filling full span of pipe and become fully turbulent.

As excursion starts, profiles (u') show that low-speed streaks start growing but are confined close to the wall. Further, some isolated patches of high and low speed appear until at the end of excursion these streaks fill up the whole pipe. The contours of swirling strength show the same. The length of streaks evaluated using a two-point correlation show that streaks grow in the size during the pre-transition period and later shrink in size during relaxation. In the core region, there is a difference between channel and pipe flow but they both respond as slugs in the core due to the effect of the pressure gradient. The turbulence appears to be frozen in the core, so that mean velocity does not change in the centre. The turbulence response is very different in core and wall region. Further, u' behaves differently as compared to the v' and w' . Near the wall ($y^+ = 8, 20$), turbulence responds with no delay while turbulence fields show a delay in the the core region which is proportional to the distance from the wall. Other components (v' , w') shows a different behavior as they either decrease slightly or remains constant during pre-transition period. During the transition, they start increasing rapidly before it is fully developed. At the centre of the pipe, turbulence structures do not change. It is reported that turbulence produced during transition is not conventional but a result of streaks which are produced during the bypass transition events.

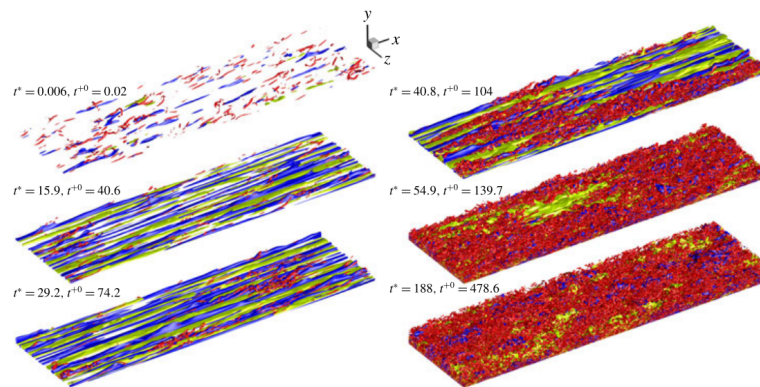


Figure 3.5: figure 1 (a) from [10] Streaks and vortex structures in three-dimensional plots of isosurfaces. Streaks are shown in green/blue and vortical structures are shown in red.

3.4. Discussion

It is seen from the literature that turbulence subjected to rapid strain has been extensively studied numerically, theoretically and experimentally. However, all the experimental studies were performed in grid-generated turbulence in a wind tunnel [5, 7, 13, 14, 34–36, 41, 42, 68]. Moreover, earlier studies have constantly reported an incorrect trend of streamwise velocity fluctuations along the channel axis for high strain rates (high contraction ratio) w.r.t. RDT [5, 13, 34, 36, 41, 68]. Further, this deviation was wrongly attributed to the non-linear interaction of turbulent scales [41] in numerous studies which are unaccounted by linear RDT. This was partially because, these studies were conducted in a wind tunnel (air as working fluid) using HWA which is susceptible to electronic and acoustic noise [42, 43]. Fewer efforts have been dedicated towards researching the physical mechanism behind such non-linear effects except a few recent studies [7, 69]. Only a single study is identified from literature which reports turbulence evolution in rapidly strained pipe turbulence [8]. Hence, strained pipe turbulence and RDT still remain an open issue.

The strained pipe flows with emphasis on turbulent scale interaction during straining and subsequent relaxation have not been explored much, in contrast, to say strained wind tunnel flows despite its prevalence in industrial applications. Moreover, the existing literature contains studies at low Re [8] and the studies at high Re do not report turbulent statistics inside the contraction [53]. In addition to experimental studies, numerical studies of strained flows are limited to moderate Re [8, 45, 46, 53]. Therefore, experiments at higher Re are warranted.

There exists a plethora of literature on spatially accelerated boundary layers (BL with FPG) as described in section 3.2. They provide a good insight into the turbulent structure and their evolution when BL is subjected to acceleration, albeit the emphasis is limited to boundary layer relaminarization under excessive acceleration close to the wall [9, 54–59, 62, 70, 71]. The temporally accelerated turbulent pipe flows are also well reported in the literature (see section 3.3) w.r.t. transition and BL relaminarization. The observations indicate that spatially accelerated wall-bounded flow behave similar to transiently accelerated flows [63] although the existing studies are limited to $Re < 35,000$ [10, 63, 65, 67, 72]. Thus, experiments at higher Re need to be undertaken. It might also be important to note that existing measurements in pipe flow and channel flow with contraction were performed with a single point measurement technique such as LDA, HWA, thus compromising on spatial turbulent structures and non-intrusiveness respectively. PIV, being a whole field measurement technique, overcomes above limitations. Further, spatial turbulent structures can be well resolved with PIV.

3.5. Research objectives and questions

The first objective of this thesis was to design, fabricate and assemble an axisymmetric contraction downstream of an existing long straight pipe [12, 73, 74] suitable for performing optical measurements such as PIV. Later, characterize the rapidity of strain achieved with the contraction. From discussion in section 3.4, two

primary zones of interest were identified (i) Inside the contraction (straining) (ii) Downstream of contraction (relaxation). Since pipe flow is wall-bounded, the effects of the wall are expected to again yield two more regions of interest viz. inner region (near-wall) and outer region (core) [75]. The following research questions are identified and attempted to address in this thesis with an emphasis on core region:

What is the effect of mildly rapid strain ($s^{*s} \sim 3.2$) on moderately high Reynolds number pipe turbulence ($Re \lesssim 47,700$);

Inside the contraction:

- How do Reynolds stresses and stress anisotropies evolve inside the contraction?
- How distinct is the effect of strain in the core and near-wall region?
- How good are the predictions of RDT along the axis of contraction?
- What is the effect of strain on the large and small scales of turbulence, separately?

In the post-contraction region:

- How do Reynolds stresses evolve in the post-contraction region?
- How do large turbulent scales evolve in the post-contraction region?
- Is there non-linear interaction in the post-contraction region due to a larger inertial sub-range at higher Re ?

4

Flow in a venturi: A preliminary experiment

This chapter reports planar PIV measurements performed in the venturi. It begins with the motivation for performing current measurements in section 4.1. This is followed by a brief overview of the experimental facility and details of measurement technique in section 4.2. Further, the results and discussions are presented in section 4.3.

4.1. Motivation

Prior to performing experiments in the long pipe with designed contraction, it was decided to perform preliminary experiments in the venturi for three main reasons. Firstly, the venturi is composed of a contraction followed by a diffuser wherein contraction imposes mean strain or spatial acceleration on the incoming turbulent pipe flow while diffuser imposes deceleration on the flow. Thus, the venturi would enable us to study turbulence evolution when strained by a large contraction ($C \sim 1 - 9$) in addition to milder contraction ($C \sim 1 - 3$) in chapter 5. Secondly, the venturi has been used extensively to study cavitation dynamics using various flow measurement modalities such as shadowgraphy (Jahangir et.al. [11]), X-ray imaging (Dash et.al. [76]) and Magnetic Resonance Velocimetry (MRV) (John et.al. [77]). Hence, the in venturi is characterised using quantitative measurement technique such as Particle Image Velocimetry (PIV). PIV being a relatively matured technique could also provide reliable benchmark data for direct comparison with upcoming measurement techniques such as MRV. Thirdly, the venturi is made of Polymethyl methacrylate (PMMA) and it was imperative to assess the applicability of PIV (particle images quality) in a varying cross-section PMMA test section. Following the success of this, a similar material would be employed to fabricate the contraction shown in chapter 5 (figure 5.2).

Therefore, PIV measurements were performed in the venturi with the following objectives; (i) To inspect mean and turbulent flow statistics in venturi. (ii) To perform PIV test measurement in varying cross-section PMMA test section. (iii) To troubleshoot encountered optical anomalies such as reflections in the particle images. (iv) Use learnings of this experiment for further experiments in the long pipe facility (chapter 5).

4.2. Experiment setup

4.2.1. Flow facility

The layout of the flow facility is shown in figure 4.1. The flow loop consists of a moderately long, straight, smooth-walled pipe of inner diameter $D = 50$ mm and outer diameter of 60 mm made of plexiglass. The working fluid is water at room temperature ($18^\circ\text{C} \pm 1^\circ\text{C}$) and ambient pressure (~ 1 bar). The flow is driven by a centrifugal pump. Upstream of the test section, an inlet length of around $40D$ is available which ensures that turbulent pipe flow is fully developed before the venturi inlet. The pressure taps upstream and down-

stream of the test section are used to measure the pressure drop across the venturi. The bulk flow rate is measured upstream of the test section with a magnetic inductive flow meter from KRONHE Altometer B.V. Note that this flow facility was designed and constructed to study cavitating flows hence, it is a closed-loop facility to allow pressurization by operating a vacuum pump. For detailed information on the flow loop refer to Jahangir et.al. [11].

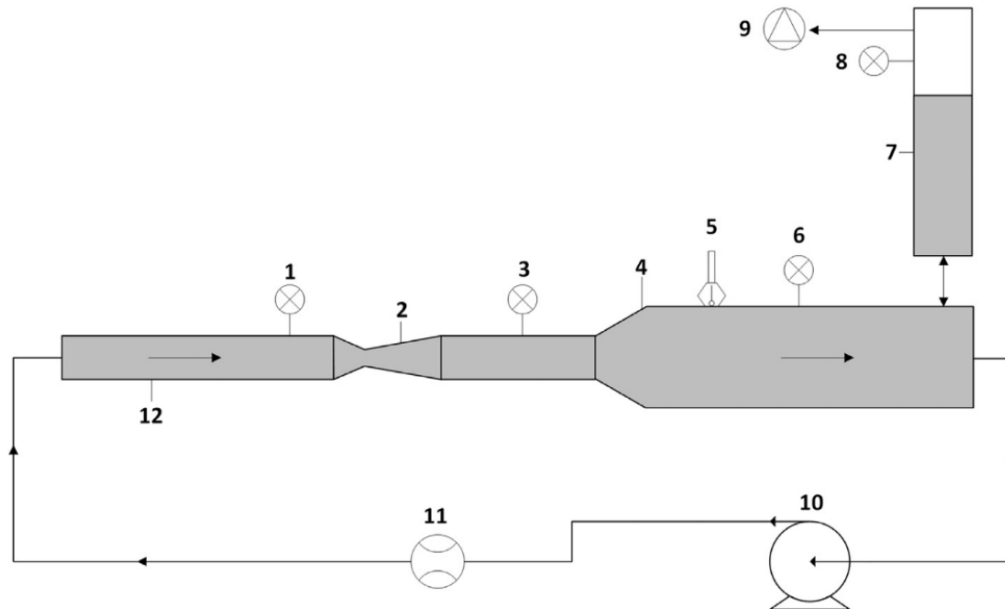


Figure 4.1: Schematic diagram of closed flow loop (flow is from left to right). Part 12: Inlet section of length $40D$, 2: Venturi test section, 4: Pressure recovery section, 5: Temperature sensor, 9: Vacuum pump 10: centrifugal pump, 11: Flowmeter, 1,3,6,8: Pressure ports (taken from: Jahangir et. al. [11]).

The venturi in figure 4.2 is made out of PMMA as mentioned before and has an inlet diameter of 50 mm. The total axial length of the venturi is 170 mm. The convergent section has an axial span of over $1D$ with an opening angle of 18 degrees and a throat diameter of 16.6 mm such that area based contraction ratio is 1 : 9. The divergent section is almost 120 mm long with an opening angle of 8 degrees. See figure 4.2, 4.5. The venturi geometry was designed to trigger cavitation at the throat without flow separation in the adverse pressure gradient of divergent section. Henceforth, the convergent and divergent section will be referred to as CS and DS respectively.

4.2.2. Measurement technique: Planar PIV

Planar PIV was employed to get quantitative and qualitative information on the flow in venturi. PIV is a non-intrusive whole field flow measurement technique wherein the flow is seeded with tiny hollow glass tracer particles having a mean diameter of $12 \mu\text{m}$ and a nominal density of $1.1 \pm 0.5 \text{ g/cm}^3$ (Sphericell 110P8, Potter Industries). The particles are expected to follow the flow faithfully due to low particle Stokes number $< O(10^{-1})$. The $r-x$ plane of the venturi is illuminated with a thin laser sheet of thickness $\sim 1 \text{ mm}$ which is formed by passing a Gaussian laser beam through a series of optics such as plane mirrors, spherical convex lens and plano-concave (cylindrical) lens. The laser sheet is introduced from the top (w.r.t. venturi) and lies in $r-x$ plane as mentioned before, cutting through the axis of venturi (see figure 4.3). The dual-head Nd:YAG laser (Litron Laser Ltd.) used is capable of producing a laser with per pulse energy of 100 mJ at a wavelength of 532 nm. The images are taken by a LaVision scientific-CMOS 16 bit camera placed perpendicular to the laser sheet. The sensor size of the camera is $2560 \text{ pixels} \times 2160 \text{ pixels}$ at a pixel pitch of $6.5 \mu\text{m}$. The Programmable Timing Unit (PTU) synchronises camera with laser pulse triggers. A macro-Nikkor objective lens of F105 mm at $f\# = 11$ is fitted on the camera producing an optical magnification of ~ 0.29 . The set $f\#$ ensures that the particles are imaged over 3–4 pixels [20] at a good image intensity. The laser pulse separation (Δt) is

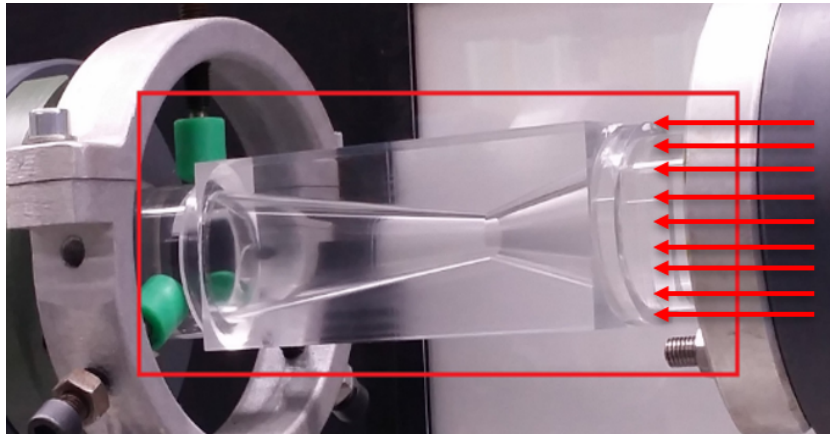


Figure 4.2: Venturi test section (red arrows show flow direction) ([11]).

a very important parameter in PIV and is set to achieve particle image displacements between 8 to 13 pixels (see table 4.1). The image acquisition frequency is set to 10 Hz and 1000 image pairs are acquired for each measurement.

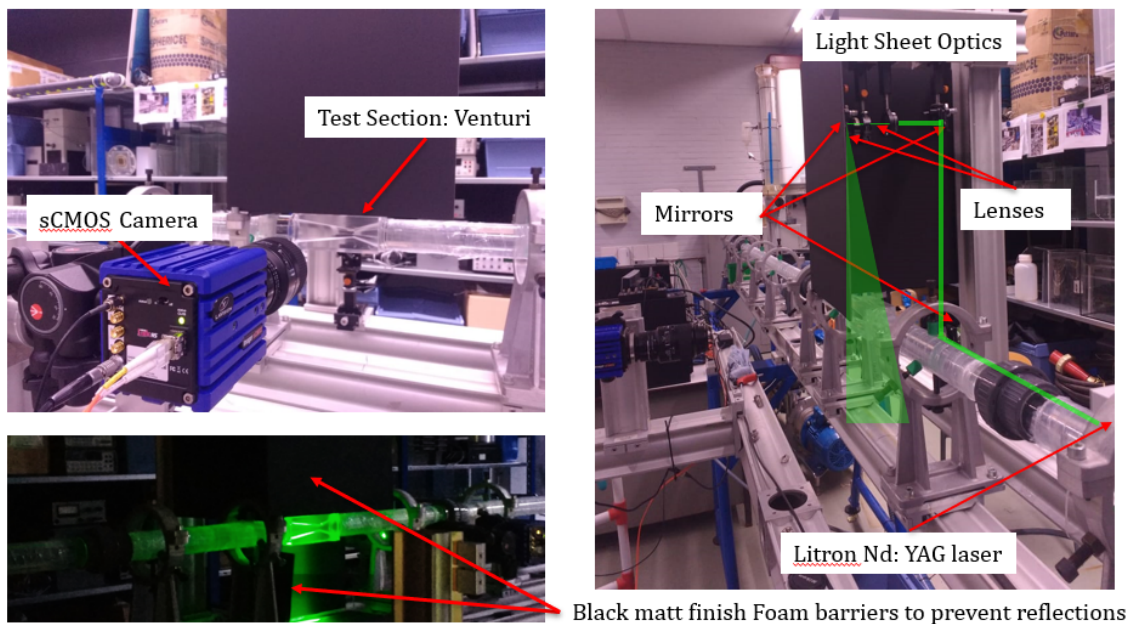


Figure 4.3: Experimental setup and planar PIV measurement system.

The raw images are enhanced using the following image processing operations: (i) The background noise and reflections are removed by subtracting a time-averaged image. (ii) Image intensity variations are smoothed out with a min-max filter of length 7 pixels. The processed images are used to evaluate the velocity vectors using commercial package DaVis 10.0.5. Multi-pass vector evaluation is done with interrogation window size reducing from 48×48 (pixel²) with 50% overlap to 24×24 (pixels²) with 75% overlap. Median filtering with universal outlier detection [78] is applied to the vector fields to remove spurious vectors. The holes left after removing spurious vectors are filled by linear interpolation of neighboring vectors. The first and second choice vectors together added to 99%. This resulted in a spatial resolution of 0.536 mm and a vector spacing of 0.134 mm. For a flow of Reynolds number $\sim 35,000$, the spatial resolution achieved corresponds to $\sim 28\eta$, where η is Kolmogorov's length scale. The histogram of the fractional part of particle image displacement (in

pixels) was generated to inspect any bias towards integer pixel displacements. This plot showed that there was no significant peak-locking error in the measurements. While setting up the experiment, special care was also taken to block reflections from surrounding objects in particle images using black matt screens (see figure 4.3). This yielded a raw particle image as shown in figure 4.4a. A sample averaged velocity vector field is as shown in figure 4.4b.

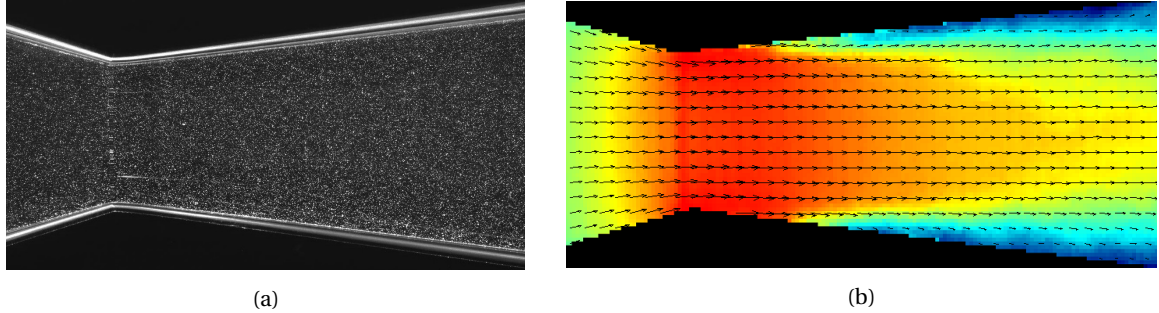


Figure 4.4: (a) A typical raw particle image. (b) A Typical time-averaged velocity vector field (Note that every fourth velocity vector is shown for the sake of clarity); The flow is from left to right.

Whilst performing PIV measurement for flow with local velocity gradient (such as in venturi), care must be taken to get sufficient particle image displacements (in pixels). This becomes even more important for turbulent statistics because actual velocity fluctuations are found by subtracting the mean flow field from instantaneous vector fields. The particle image displacement resulting in velocity fluctuations could be smaller than 0.1 pixels which is at the noise level of PIV measurement. It might be a good idea to have a smaller FOV to reduce bias in velocity data (as a result of averaging) due to the effect of the local velocity gradient on the cross-correlation interrogation window. The smaller FOV will have smaller local velocity gradients, hence, the lowest particle image displacement can be higher and the highest particle image displacement is limited to $1/4^{th}$ cross-correlation interrogation window size. Thus, the absolute value of velocity fluctuations can stay above the noise level, although, this can compromise spatial resolution of the measured data especially flow close to the wall.

4.2.3. Design of experiment

The major focus of experiments was evidently on the convergent section of the venturi due to its relevance to the current research. The measurement campaign was designed such that the measurements would be performed for three fields of view (FOV) as shown in figure 4.5. However, due to unforeseen circumstances and time constraints, only one FOV could be completed (figure 4.5b). The author is aware that current FOV is not the most ideal FOV for studying strained turbulence as flow could be measured only in the last 20% of contraction. It was still chosen because the flow in venturi could be more completely characterized in this configuration. The relevant non-dimensional numbers are plotted along the axis of CS as shown in figure 4.6.

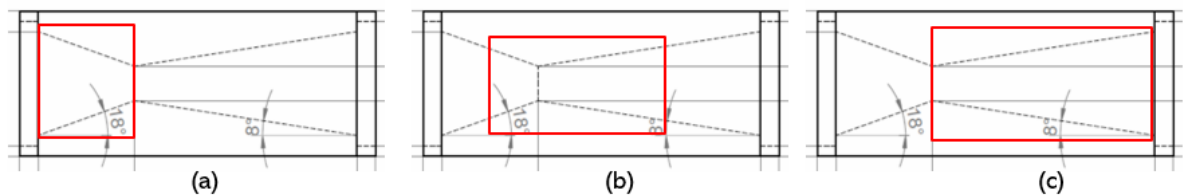
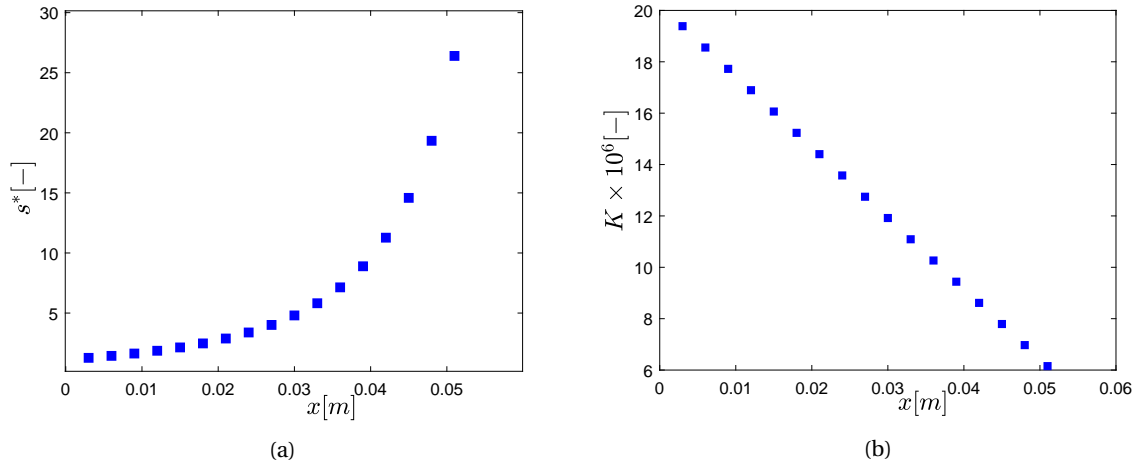


Figure 4.5: Designed measurement campaign with different FOVs (red box show schematics of various FOVs).

The non-dimensional strain rate (s^*) essentially depends on the contraction geometry, while the acceleration parameter (K) is a function of contraction geometry and flow Re . Hence, for a given s^* , the measurements were performed for three different non-cavitating Re (defined based on inlet flow diameter). See the test ma-

Test #	Flow Rate [m ³ /s]	Re	Laser Pulse Separation (Δt [μ s])
01	0.0004	10,000	130
02	0.00136	35,000	45
03	0.00235	60,000	27
04	0.00280	71,300	21

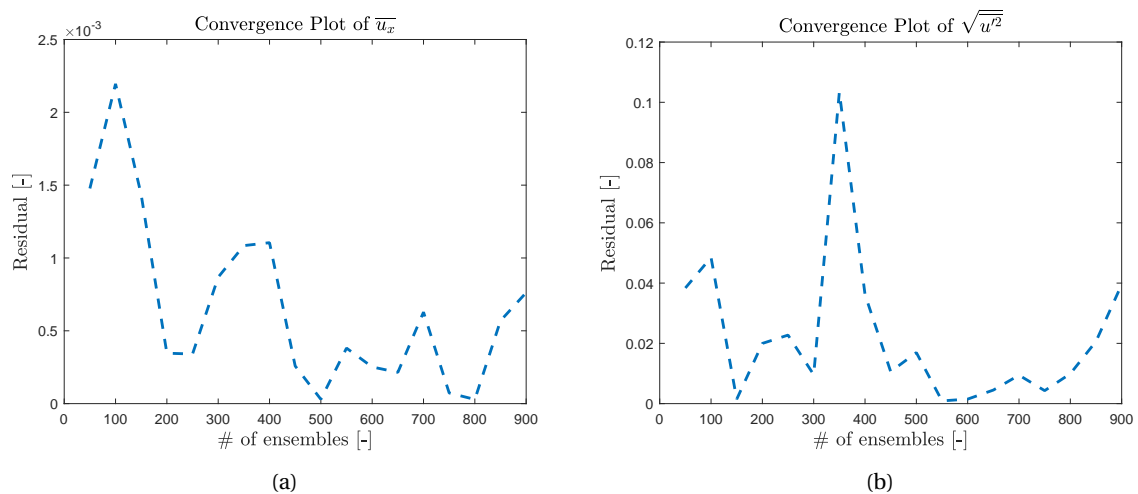
Table 4.1: Test matrix for experiments in venturi

Figure 4.6: (a) Non dimensioned strain rate (s^*). (b) Acceleration parameter (K) along the axis of convergent part of venturi for $Re = 60,000$. See 2.26, 2.27 for definitions Note that $x=0$ corresponds to the inlet of CS, $x=0.051$ to throat.

trix in table 4.1. It was observed that for $Re > 72,000$, cavitation commenced.

4.2.4. Remark

The convergence test of mean velocity data over 1000 ensembles revealed that the mean flow statistics barely converged. However, turbulent statistics for 1000 ensemble did not converge (see figure 4.7). This is a major setback in current experiments, however, the experiments could not be repeated due to the unavailability of the experimental facility. The author suspects that the flow facility being a closed-loop, loop could have had disturbances.

Figure 4.7: (a) Convergence plot of mean velocity at a point (Centreline of the CS). (b) Convergence plot of streamwise velocity fluctuations at a point (Centreline of the CS). Note that residual is defined on the basis of old value (0) and new value (i) of the quantity such that Residual = $(i - 0)/0$.

The velocity-time trace showed the existence of large structures or disturbances in the flow. Furthermore, the measured pressure signal also showed disturbances of similar time scales as that of velocity disturbances (see figure 4.8). It is suspected that in 100 seconds (measurement time), sufficient disturbances have not passed through the measurement plane. Hence, the data is not converged. However, the exact reason for these disturbances in the flow loop is not known yet. Two-point correlation of velocity fluctuations were

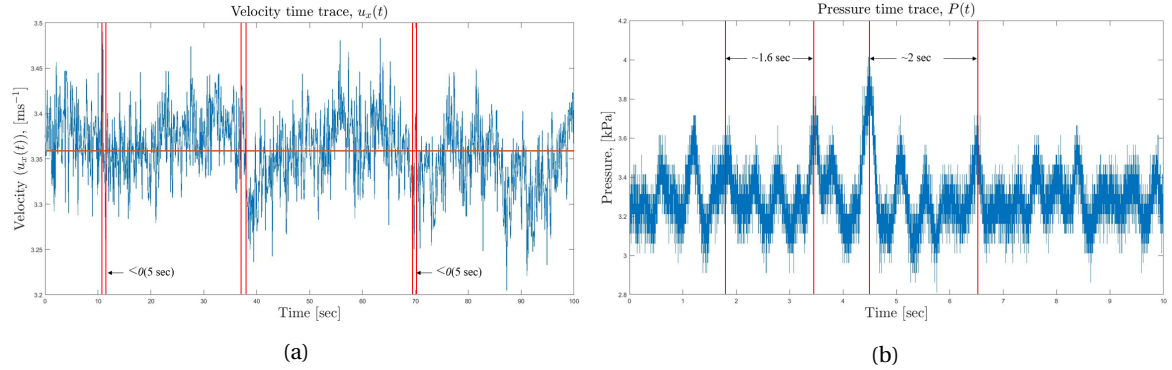


Figure 4.8: (a) Velocity-time signal measured at a point on the axis of CS by PIV. (b) Pressure time signal measured by pressure transducer upstream of venturi.

evaluated in longitudinal (R_{uu}) and transverse direction (R_{vv}) to estimate the response of large scales to the spatial acceleration (in CS). It was observed that flow disturbances in streamwise direction resulted in local bulk acceleration of the flow and hence, correlation maps (R_{uu}) were not reliable as shown in the figure 4.9a. Similarly, two-point correlation of out-of-plane vorticity ($R_{\omega\omega}$) was evaluated to discern the effect of strain on small scales of turbulence. It showed that small scales were smaller than the physical dimensions of the PIV Interrogation Window (IW) hence, the correlation existed only over the length of IW and employed moving mean filter's kernel size (5×5 , pixel²) as shown in figure 4.9b. The resolution achieved in the measurement is evidently not enough to get information on the smallest scales of turbulence.

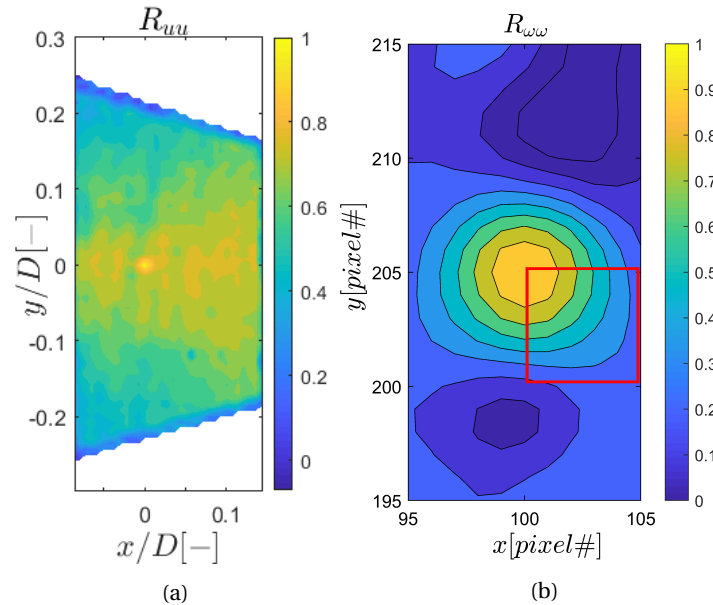


Figure 4.9: (a) Two-point correlation of velocity fluctuations(R_{uu}) for $Re=35,000$ in CS. (b) Two-point correlation of vorticity ($R_{\omega\omega}$) for $Re=35,000$ in CS. (Red boxes indicate the PIV cross-correlation interrogation window).

4.3. Results and discussion

The results are presented and discussed separately for the CS and DS of the venturi with an emphasis on CS of venturi. Furthermore, vector fields were evaluated separately in CS and DS due to the slight difference in the magnification caused by different opening angles of CS and DS. Refer to Appendix 1 for details. While showing axial evolution of different flow quantities, three radial profile are chosen in CS such that L_1 is 42.4 mm, L_2 is 46.41 mm from the venturi inlet upstream of the throat. L_3 is close to the throat. Similarly, in DS, four profiles are chosen such that L_4 is 57.8 mm, L_5 is 67.3 mm, L_6 is 76.3 mm, L_7 is 85.8 mm from the venturi inlet. See figure 4.10 for articulations. The radial distance (r) is non-dimensionalized w.r.t. local radius (R) such that r/R varies from -1 to 1 . While plotting the axial variation of flow quantities, zero on x-axis corresponds to the inlet of venturi (see figure 4.10).

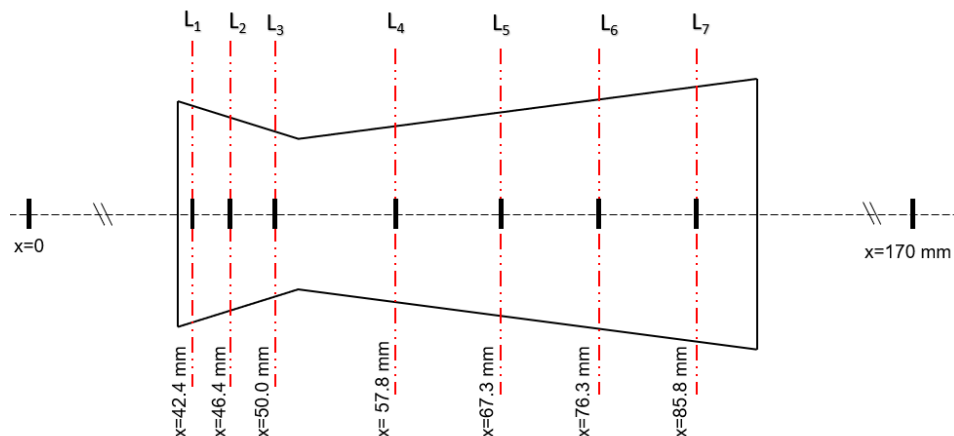


Figure 4.10: Schematic of measurement domain showing various radial profiles over which data has been shown in this section. Note that the flow is from left to right with 0 being the inlet of venturi and 170mm being the exit of the venturi.

4.3.1. Mean flow

First, we examine the mean flow characteristics in the venturi ensemble averaged over time. In the positively strained region (CS), the mean velocity along the axis of venturi is seen to increase as expected due to the acceleration. The mean velocity has a sharp peak at the throat and then starts to decrease in the DS as shown in figure 4.11. The centreline velocity is compared with the bulk velocity in the venturi which is calculated using mass conservation. The measured and calculated centreline velocity in CS match fairly well but the measured velocity is slightly higher than the calculated values. Further, the axial centreline velocity displays near similarity when normalised by incoming bulk velocity (U_{in}) at different Reynolds numbers (Re). Hence, the measurements are consistent with each other.

In the DS, measured centreline velocities are higher than the bulk velocity. Further, the near similarity in $u(x)/u_{in}$ is invalid because in DS, there exists an adverse pressure gradient leading to adverse flow separation. Due to flow separation near the wall, an effective cross-section area for flow is reduced resulting in higher centreline velocities. Further, this deviation is more pronounced at lower Re , i.e., (10,000, 35,000) since at high Re (60,000, 71,300) flow can still stay attached. This can qualitatively be seen in instantaneous flow visualization shown in figure 4.12 and 4.13. In figure 4.12 ($Re \sim 10,000$), flow separation is much more than in figure 4.13 ($Re \sim 60,000$) as evident from larger recirculation zones (blue zones with negative velocities).

The flow in DS is complex due to flow separation in the BL and the jet formation in it. The jet exhibits flapping or the 'Coanda effect', where jet intermittently snaps from the pipe wall and wraps around the opposite wall's curvature. Further, the flow can be highly three dimensional due to this effect. This is seen in figure 4.12 (d, e) and figure 4.13 (c, d). For $Re = 10,000$, the effect is more severe than at $Re = 60,000$ due to larger extent of recirculation zone in the former. No evident periodicity is observed in the jet flapping phenomenon at current

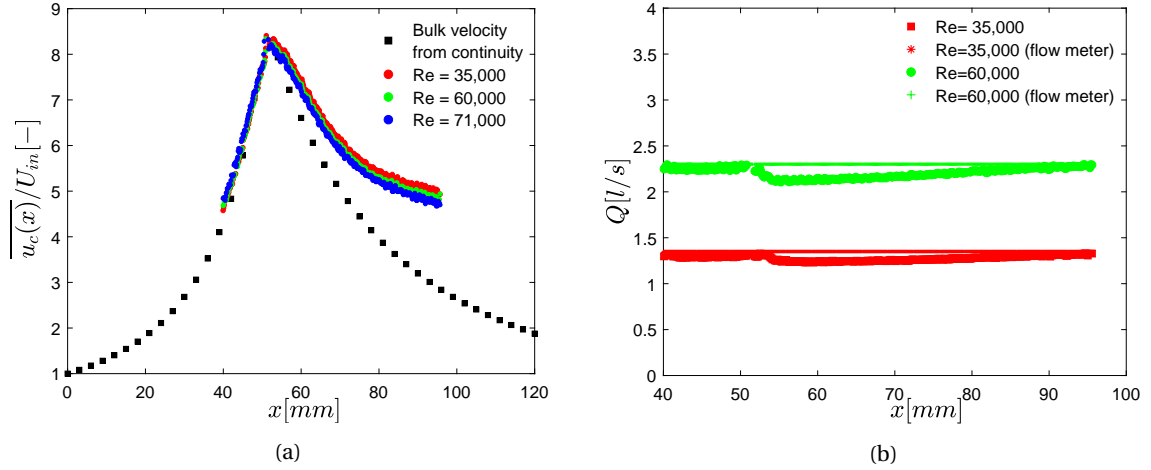


Figure 4.11: (a) Mean axial velocity $u(x)$ normalised by inlet flow velocity U_{in} in the straight pipe upstream of venturi vs. axial distance along the centreline of venturi. (b) Mass of fluid passing through each cross-section of venturi compared with mass flow rate measured by flow meter.

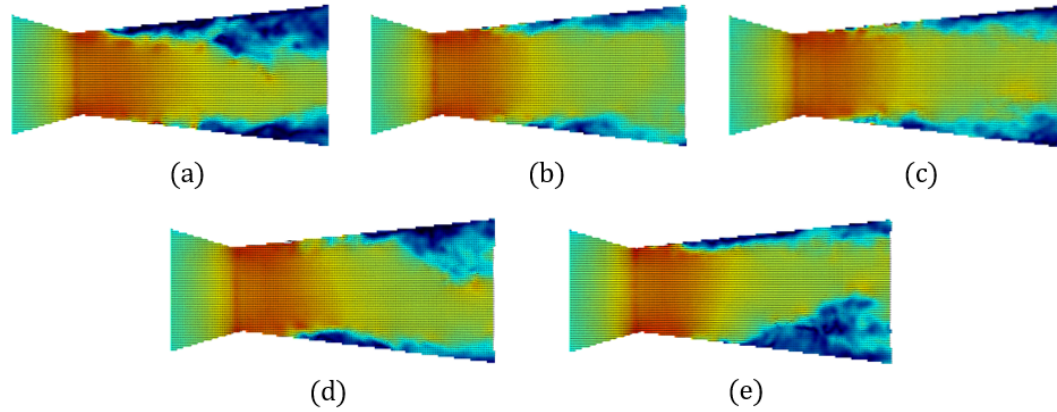


Figure 4.12: Instantaneous velocity contour plots as the function of time qualitatively showing flow separation in the DS for $Re = 10,000$ (a) $t = 1$ sec (b) $t = 2$ sec (c) $t = 3$ sec (d) $t = 4$ sec (e) $t = 5$ sec.

measurement frequency (10 Hz). Due to continuity, mass crossing each cross-section in venturi should be conserved. The mass flux through venturi is calculated by integrating measured velocity profile ($\overline{u(x)}$) along the local radii ($R(x)$) (equation 4.1) and shown in the figure 4.11b.

$$\dot{m}(x) = 2\pi\rho \int_0^{R(x)} \overline{u(x)} r dr \quad (4.1)$$

This is then compared with the mass flow rate measured by the flowmeter. As can be seen in the CS, mass flux computed by integrating the mean velocity profile ($\overline{u(x)}$) is almost constant but slightly lower than flowmeter reading. This is because the accelerated boundary layer gets very thin and axial velocity profile ($\overline{u(x)}$) very close to the wall could not be resolved accurately by the current measurement technique. Hence, the mass calculated by integrating $\overline{u(x)}$ appears slightly less. However, at the beginning of the DS, a small amount of mass is missing. The reason for this is not well known, but the author suspects it could be because jet flapping in and out of the measurement plane or even back and forth along the axial direction of venturi. Alternatively, it could be a manifestation of a severally accelerated mean velocity profile that could not be measured near the wall resulting in mass under-estimation. The above argument is further corroborated by more mass missing at higher Re .

The mean axial velocity profiles have been plotted at various vertical lines (L_1 to L_7), see figure 4.10. The

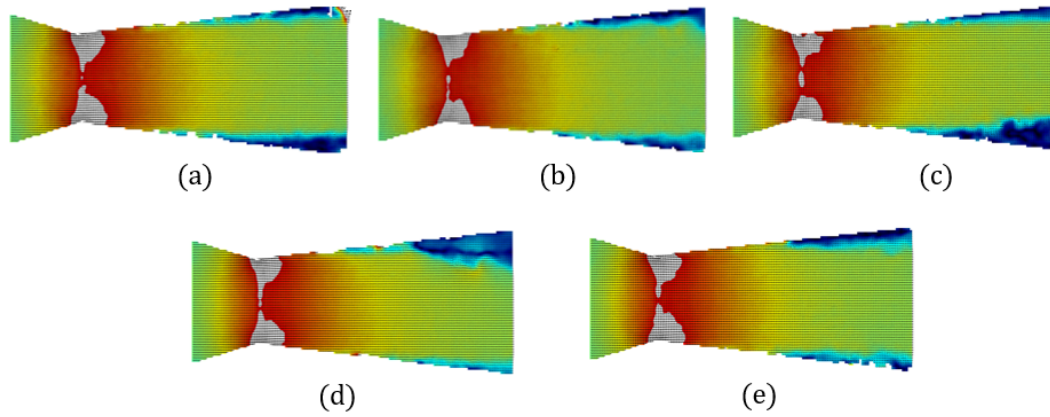


Figure 4.13: Instantaneous velocity contours as the function of time qualitatively showing flow separation in the DS for $Re = 60,000$ (a) $t = 1$ sec, (b) $t = 2$ sec (c) $t = 3$ sec (d) $t = 4$ sec (e) $t = 5$ sec.

velocity profiles exhibit similar behavior at all Re , hence data for only $Re = 35,000$ case is shown. In the CS, due to the acceleration, BL becomes very thin. Hence, the profile close to the wall could not be resolved by planar PIV (see figure 4.14a). This is due to (i) finite spatial resolution of PIV, (ii) strong velocity gradient across the cross-correlation interrogation window, (iii) glaring close to the wall, (iv) curvature of the pipe, (v) tracer particle settling on the wall. The velocity profiles in the contraction get flatter than fully turbulent velocity profiles in pipe flow (see figure 4.15a). This is because the pressure gradient due to contraction acts uniformly over the entire cross-section of the pipe (CS of venturi). However, due to the no-slip boundary condition of the wall, the velocity close to the wall has to go to zero. Thus, the mean axial velocity profile flattens out to satisfy the boundary condition. This in turn increases the mean velocity gradient very close to the wall. The flattening of the mean velocity profile results in a breakdown of log law [79]. This could not be verified because the linear velocity profile very close to the wall could not be measured inside the CS due to the reasons specified above. Further, Clauser-plot method could not be used to calculate friction velocity as log-law itself is known to be invalid in BL with pressure gradient (Harun et.al. [79]).

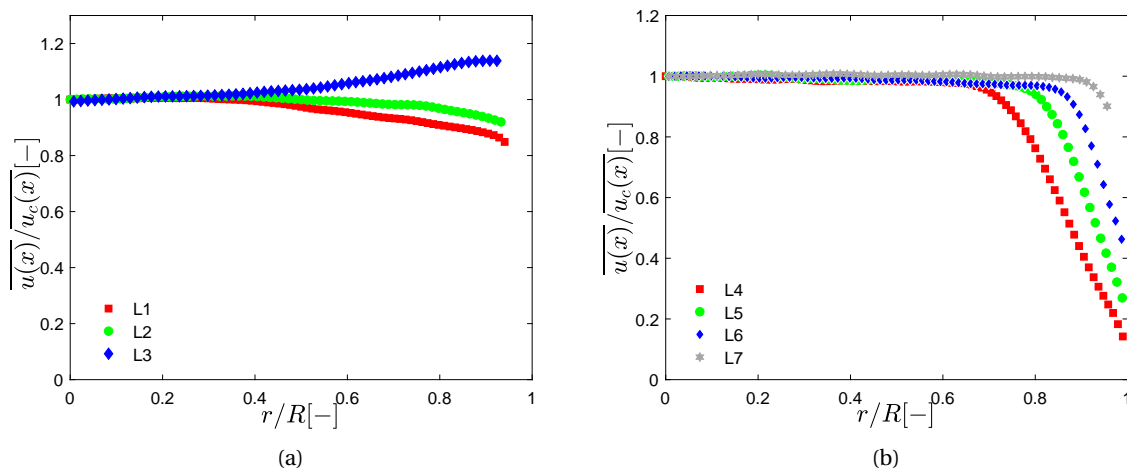


Figure 4.14: (a) Mean axial velocity $u(x)$ plotted along radial direction for L_1, L_2, L_3 for CS for $Re = 35,000$. (b) Mean axial velocity $u(x)$ plotted along the radial direction for L_4, L_5, L_6, L_7 for DS for $Re = 35,000$. For inset see figure 4.10.

Very close to the throat, maximum velocity does not occur at the centre but occurs near the wall. This is a typical velocity profile at nozzle throat [80]. In the DS, mean velocity profiles are uniform in the core region except near the wall as it resembles plug flow profiles. The radial portion for which velocity is uniform reduces as we move downstream of the throat. Further downstream of the throat in DS, the mean axial velocity

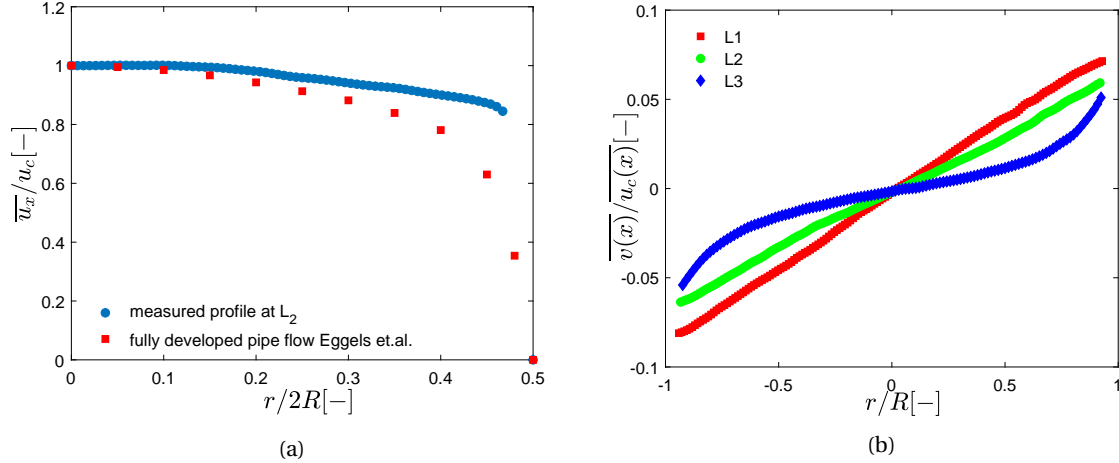


Figure 4.15: (a) Measured mean axial velocity profile (normalised by centreline velocity) inside contraction at L_2 for $Re= 35,000$ compared with fully developed axial velocity in straight pipe for $Re= 5,300$ (figure 2 in Eggels et.al. [12]). (b) Mean radial velocity profile $v(x)$ in CS at L_1, L_2, L_3 for $Re = 35,000$. For inset see figure 4.10.

profile appears like in jet flow (not shown here) due to the jet formation. There is a sign of swirl in the mean flow due to the tendency of the jet to wrap around the curvature of the pipe (Coanda effect), as also seen in the instantaneous velocity fields (see figure 4.12, 4.13). Few diameters from the outlet of venturi, the mean flow is expected to re-attach again and subsequently return to the fully developed turbulent pipe flow profile.

The profiles of radial velocity are shown in figure 4.15b for CS for $Re = 35,000$. The profile at L_1 and L_2 are almost linear, however, further inside the contraction (at L_3), the radial velocity profile gets distorted and varies as higher-order polynomial along the radius. Ideally, if $d\overline{u(x)}/dx$ is constant in CS of venturi then from continuity, \overline{v} should vary linearly along the radial direction as per equation 4.2.

$$\frac{\partial \overline{u}}{\partial x} = -\frac{1}{r} \frac{\partial \overline{v}}{\partial r} \quad (4.2)$$

It appears that u indeed varies linearly (see figure 4.11a) and hence $d\overline{u}/dx$ is almost constant. However, this trend is not seen further inside the contraction near the throat as \overline{u} profile shows a maximum near the wall and not in the centre of venturi (see L_3 profile in figure 4.14a). Hence, mass continuity results in \overline{v} showing non-linear trends.

4.3.2. Turbulent statistics

The turbulent velocity fluctuations have been normalised by upstream pipe straight centreline velocity (U_{in}) to show the behaviour of absolute velocity fluctuations along the axis of venturi (figure 4.16a). Similarly, velocity fluctuations have been normalised by local centreline velocity ($u(x)$) to show the effect on turbulent intensity (TI) due to the acceleration and deceleration (figure 4.16b). To discern the evolution of Reynold's stress inside CS and DS, the profiles of TI ($u'/u(x)$, $v'/u(x)$), shear stress ($\overline{u'v'}/u(x)^2$) are also shown in the figure 4.19.

Due to the acceleration, TI along the axis of venturi keeps decreasing. This effect is majorly due to the normalisation w.r.t. local centreline velocity ($U(x)$). The absolute value of velocity fluctuations (u' and v'), however, are seen to increase slightly along the axis of venturi in CS. This is counter-intuitive since the author expected decrease in streamwise velocity fluctuations (u') and increase in transverse fluctuations (v') due to expected inter-component transfer of turbulent energy from streamwise to transverse direction via vortex stretching (see figure 2.8) as also predicted by linear Rapid Distortion Theory (RDT). However, it is important to note that the current measurements are not performed at the beginning of contraction. An alternative explanation of this would be: the current contraction is quite strong with local contraction ratio (C) varying from $\sim 4 - 9$. If turbulent structures get stretched excessively due to high C , the velocity gradient will increase immensely and

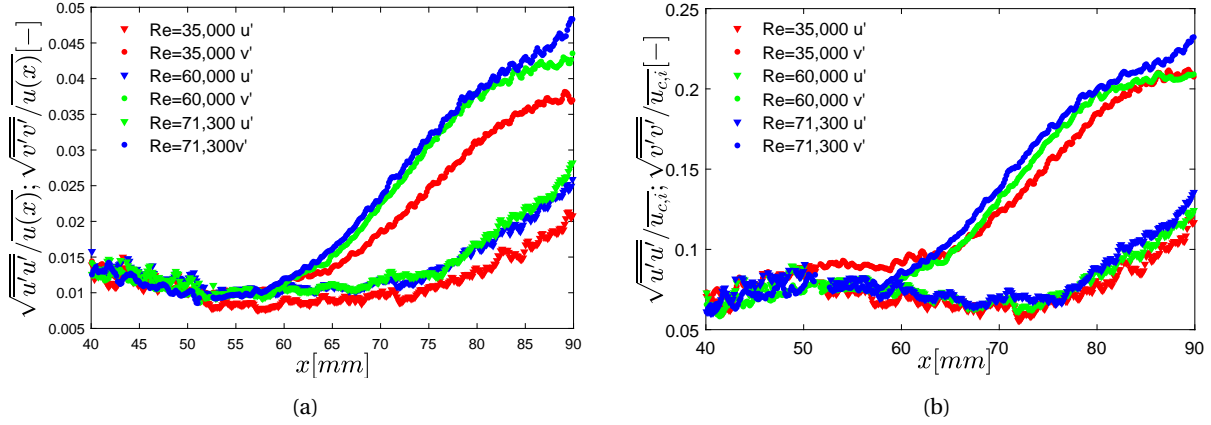


Figure 4.16: (a) Velocity fluctuations (u'), (v') normalised by centreline velocity ($u(x)$) along the centreline of venturi for $Re= 35,000, 60,000, 71,300$. (b) Velocity fluctuations (u'), (v') normalised by incoming bulk velocity (u_{in}) along the centreline of venturi for $Re= 35,000, 60,000, 71,300$.

dissipation may become important. Similar behaviour of turbulent velocity fluctuations was seen by Hussain et.al. [6, 40] in their measurement where only in the initial part of the contraction, RDT was satisfied qualitatively. In the post-contraction region, longitudinal (u') and transverse velocity (v') fluctuations were seen to increase along the centreline. Apparently, RDT is valid only for the initial part of contraction and shows deviation as contraction ratio (C) gets higher ($C > 4$) (see figure 3.1). Further, our data when compared with the data of Hussain et. al. [6] seems to agree well within the scatter of the data (see figure 4.17).

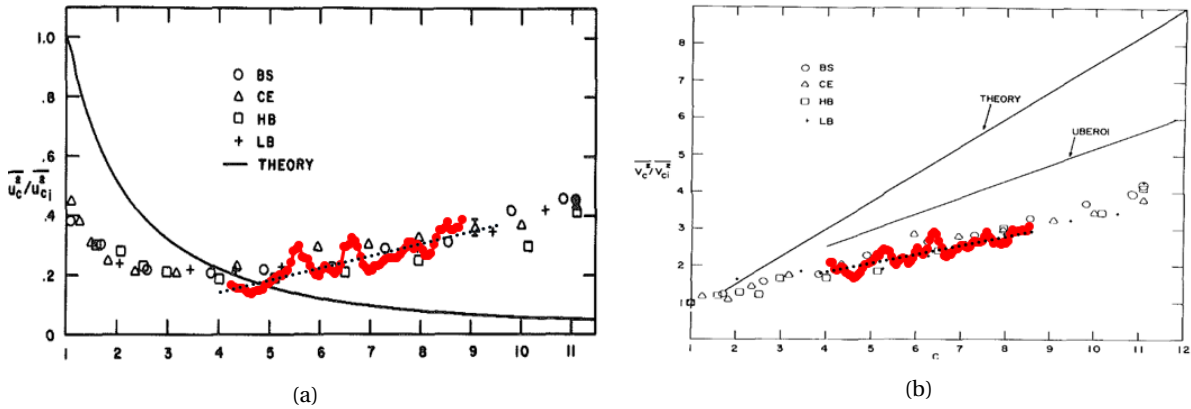


Figure 4.17: (a) Streamwise Normal Reynolds stress as a function of local contraction ratio (C) compared with data of Hussain et.al. [6]. (b) Transverse Normal Reynolds stress as a function of local contraction ratio (C) compared with data of [6]. -o-: current measurement, : trendline through measured data, Theory: Rapid Distortion Theory (RDT) predictions [4], Uberoi: Data from [5]

The shape of profiles of u' , v' , $\overline{u'v'}$ look similar to respective profiles in the fully developed straight pipe but they appear highly attenuated. The TI at the centreline of CS ($\lesssim 1\%$) is considerably lower than found in a typical fully developed pipe flows ($\sim 4 - 5\%$). Note that TI at the axis of CS in our measurements is of the same order as reported by [81] in a venturi. Contrary to normal stresses, absolute shear stress slightly decreases or remain the same as turbulence is accelerated as shown in the figure 4.19b. Evidently, when normalised by local centreline velocity, shear stresses decrease when turbulence is accelerated. Such stress freezing behaviour of Reynolds shear stress has also been reported in spatially accelerated pipe flows [8], spatially accelerated wall-bounded flows [58, 62] and even in temporally accelerated flows [63, 66]. These observations suggest that shear stress is frozen in when strained. This has been mathematically shown in section 4.4

Inside the DS, turbulent fluctuations (u' , v') remain almost constant for a short distance. Later, streamwise

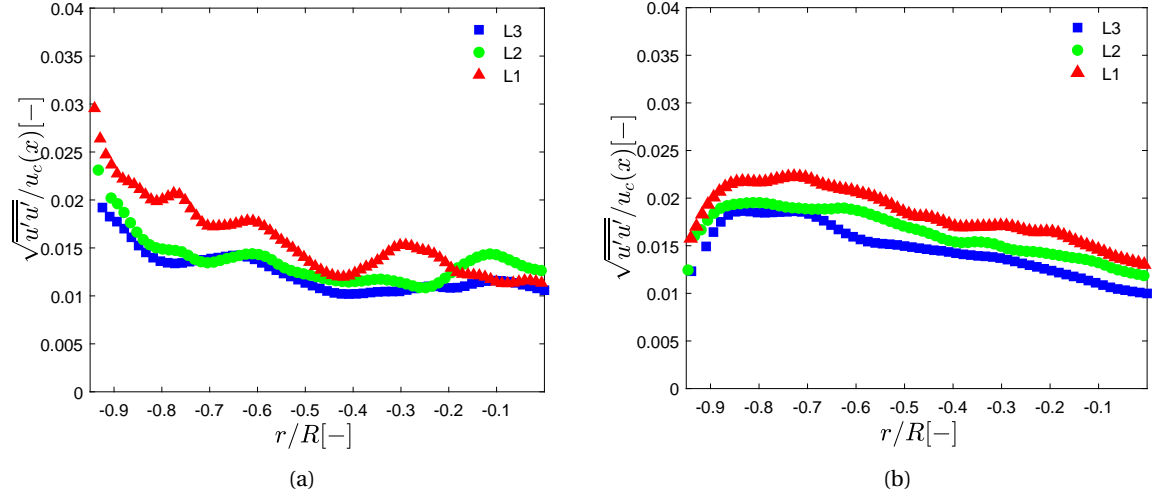


Figure 4.18: (a) Streamwise turbulent intensity at various profiles (L_1 , L_2 , L_3). (b) Transverse turbulent intensity at various profiles (L_1 , L_2 , L_3) for Re 35,000. For inset see figure 4.10.

turbulent fluctuations decrease as transverse velocity fluctuations increase (see figure 4.16b). Further, the increase in v' is at the expense of u' suggesting redistribution of turbulent energy from streamwise to the transverse direction. This trend of velocity fluctuations qualitatively agrees with vortex stretching. See section 2.7.3 for a detailed explanation. However, it is inconsistent that such effect is seen in the DS as such redistribution of turbulent energy is a characteristic of vortex stretching inside the contraction.

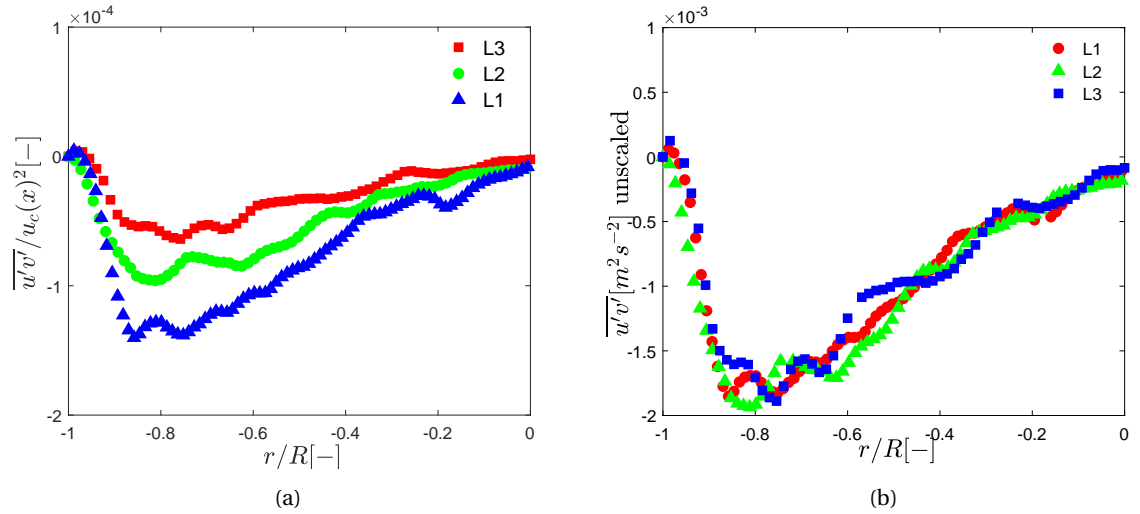


Figure 4.19: (a) Reynolds shear stress ($\overline{u'v'}$) normalised by local centreline velocity square along profiles L_1 , L_2 , L_3 for $Re=35,000$. (b) Absolute Reynolds shear stress ($\overline{u'v'}$) along profiles L_1 , L_2 , L_3 for $Re=35,000$. For inset see figure 4.10.

To verify this, surrogate Reynolds stress anisotropy tensor component (b_{11}^s) [24] is plotted against the centreline of venturi in the figure 4.20. The surrogate anisotropy tensor is conveniently defined for two-dimensional planar measurements with δ_{ij} being Kronecker delta function, $\overline{u_i' u_j'}$ being normal Reynolds stress(s) (equation 4.3).

$$b_{ij}^s = \frac{\overline{u_i' u_j'}}{2k_s} - \frac{1}{2}\delta_{ij} \quad (4.3)$$

$$k_s = \frac{\overline{u_1' u_1'} + \overline{u_2' u_2'}}{2} \quad (4.4)$$

It is seen that the trend of streamwise Reynolds stress anisotropy (b_{11}^s) qualitatively matches with the RDT (Chen et.al. [82]). Inside the CS, b_{11}^s remains very close to zero indicating equipartition of energy in the longitudinal and transverse direction. Inside the DS, b_{11}^s drops to negative values as v' starts to increase at the expense of u' . This is essentially due to the redistribution of turbulent energy from streamwise to the transverse direction. According to RDT, minimum value of b_{11}^s reached is -0.45 [24] before it starts to increase again. However, current measurements show a minimum value of -0.65 . This can be attributed to the apparent energy in the transverse direction because of jet flapping. Thus, DS downstream of contraction is ideally not desired while studying such flows. It can be seen from figure 4.20 that there is a tendency towards equipartition of energy as flow proceeds further downstream (b_{11}^s tending towards zero again).

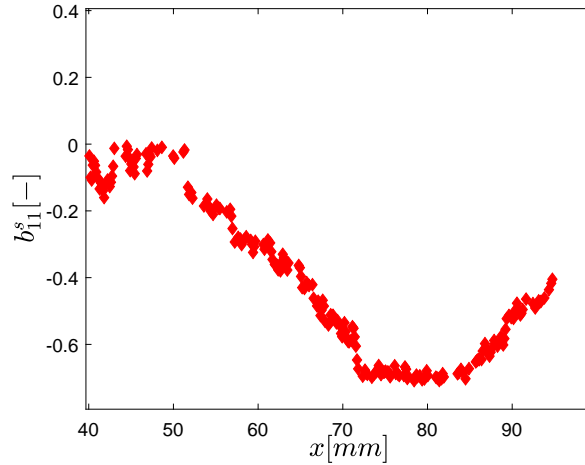


Figure 4.20: Evolution of two-dimensional surrogate of Reynolds stress anisotropy tensor component b_{11}^s along the axis of venturi.

The above observation suggests that the response of turbulence to applied such high strain or acceleration is delayed. Such delayed response of turbulence has also been reported in transiently accelerated turbulence [63, 66, 83] and pulsatile turbulent flows Tu et.al. [64]. This effect is not clear in TI (figure 4.16a) due to the normalisation by local centreline velocity ($U(x)$). If we inspect Reynolds stresses along L_4 profile in figure 4.21 which lies in this region, it is observed that all Reynolds stress profile (u' , v' , $\overline{u'v'}$) become low and uniform in along the radial direction except very near to the wall. This is again a well observed effect of acceleration on turbulence [8, 53, 58, 62, 65, 84]. It seems that mean velocity responds to acceleration without delay but turbulence lags w.r.t. strain and thus mean flow. During the lag, u' , v' increases steadily but $\overline{u'v'}$ stays frozen. Such a response of turbulence was reported by He et.al. [63] in transiently accelerated turbulence. Similarly, [58, 59] have reported slight increase of absolute velocity fluctuations (u'/u_{in} , v'/u_{in}) in spatially accelerated boundary layer flow and converging channel flow respectively. As seen from the figure 4.16b, there is no discernible effect of currently employed Re affecting the response time of turbulence in the core region of pipe. This could suggest that delay is a function of strain rate which is completely dependent on the geometry of contraction and not on flow Reynolds number (Re). However, to test this hypothesis, more experimentation is warranted, possibly with different contraction geometries and significantly higher Re .

Further downstream of the throat in the DS, turbulent fluctuations and TI rise steeply along the centreline of venturi. A look at the radial development of turbulent normal stresses reveal that turbulent intensity in the core stays uniform and low ($\lesssim 4\%$). This region of uniform and low stress erodes as turbulence evolves downstream. Near the wall, stream-wise normal stresses are very high as compared to that of core (of magnitude one order higher). Further, v' is higher than u' (\sim more than twice) in the core region of venturi but near the wall, u' is higher than v' . This is attributed to flow separation and jet flapping prominent in this region as jet snaps from upper to lower wall and vice versa in the transverse direction. From L_4 to L_7 (see figure 4.21), it is seen that all turbulent stresses start to increase slowly from near the wall into the core. However, in this region, turbulence relaxation is masked by the effects of BL separation and jet flapping. Hence, flow separation is absolutely undesirable while studying relaxing turbulence in post contraction region. This along with

other shortcomings in measurement technique itself are eliminated in the next set of experiments reported in chapter 5.

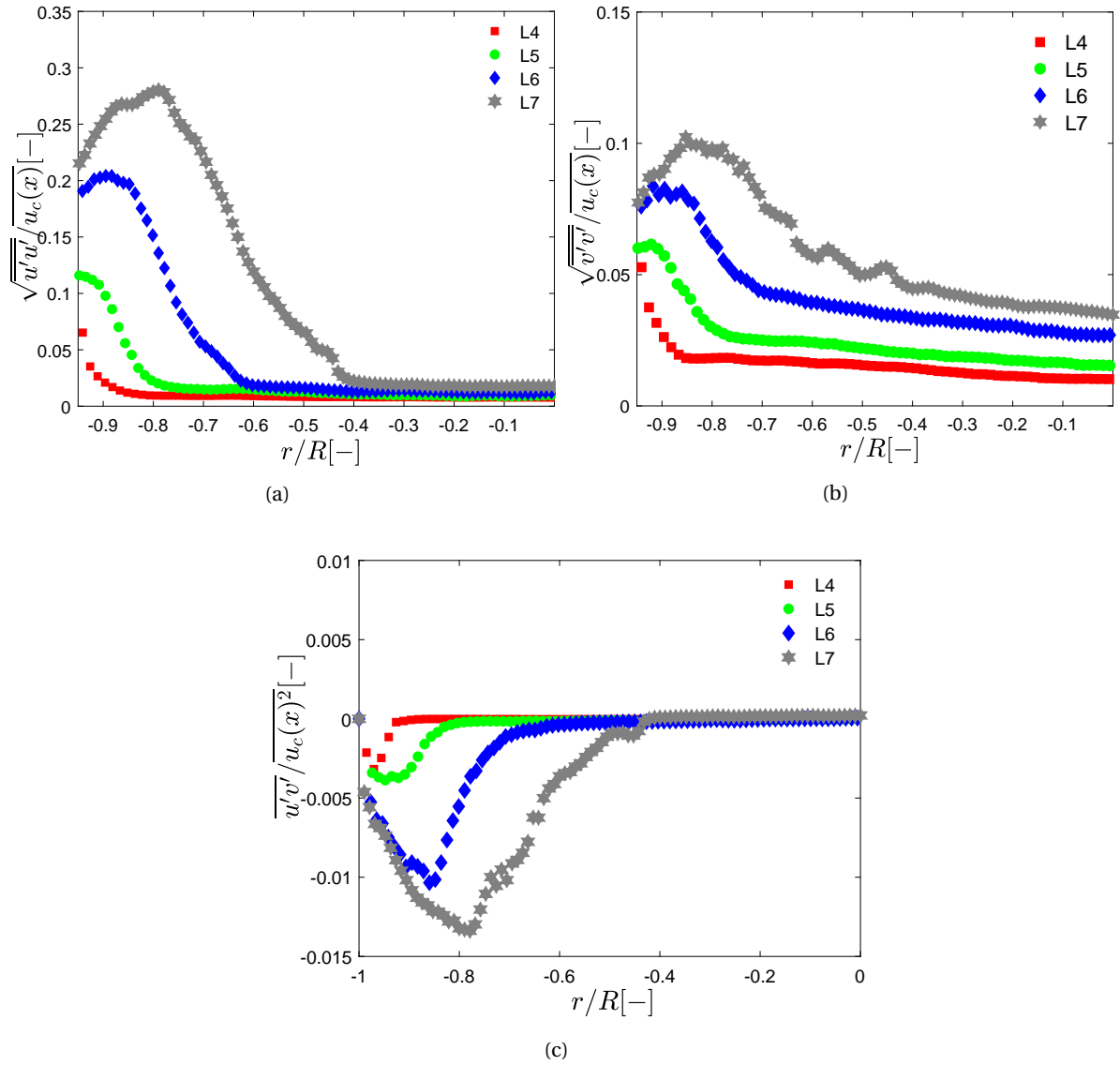


Figure 4.21: (a) Streamwise turbulent intensity at various profiles (L_4 , L_5 , L_6 , L_7). (b) Transverse turbulent intensity at various profiles (L_4 , L_5 , L_6 , L_7) for $Re=35,000$. (c) Reynolds shear stress at various profiles (L_4 , L_5 , L_6 , L_7). For inset, see figure 4.10.

4.4. Mathematical model

This section intends to apply the observed evolution of the Reynolds stresses inside the contraction to the governing differential equations. The fluid flow inside the contraction was modelled using the Reynolds averaged u -momentum equation in cylindrical coordinates (see equation 4.7). The pipe flow is assumed to be axisymmetric, i.e., $\frac{\partial}{\partial \theta} = 0$ and statistically stationary. Further, the focus is in the core region of the pipe, i.e., near the axis of contraction.

Let u , v be the axial and radial velocity component. Further, \bar{u} , \bar{v} be the average quantities. u' , v' be the fluctuating velocity in the respective directions, ρ is the fluid density and \bar{P} is the mean hydrostatic pressure.

$$u = \bar{u} + u' \quad (4.5)$$

$$v = \bar{v} + v' \quad (4.6)$$

$$\underbrace{\rho \frac{\partial \bar{u}}{\partial t}}_{\text{I: unsteady Term}} + \underbrace{\rho \bar{u} \frac{\partial \bar{u}}{\partial x} + \rho \bar{v} \frac{\partial \bar{u}}{\partial r}}_{\text{II: convection terms}} = \underbrace{-\frac{d\bar{P}}{dx}}_{\text{III: Pressure Gradient}} + \underbrace{\mu \frac{\partial^2 \bar{u}}{\partial x^2} + \frac{\mu}{r} \frac{\partial}{\partial r} \left(r \frac{d\bar{u}}{dr} \right)}_{\text{IV: viscous diffusion}} - \underbrace{\frac{\rho}{r} \frac{\partial r \bar{u}' v'}{\partial r} - \rho \frac{\partial \bar{u}' u'}{\partial x}}_{\text{V: Turbulent diffusion}} \quad (4.7)$$

For a statistically stationary flow, $\frac{\partial \bar{u}}{\partial t} = 0$. Moreover, from the experimental results we observe that velocity profile in the core appears uniform/flat like plug flow, i.e., $\frac{\partial \bar{u}}{\partial r} = 0$. Hence, \bar{u} is assumed to be a function of only x (and not r). Eliminating these terms from equation 4.7:

$$\cancel{\rho \frac{\partial \bar{u}}{\partial t}} + \rho \bar{u} \frac{\partial \bar{u}}{\partial x} + \cancel{\rho \bar{v} \frac{\partial \bar{u}}{\partial r}} = -\frac{d\bar{P}}{dx} + \mu \frac{\partial^2 \bar{u}}{\partial x^2} + \frac{\mu}{r} \frac{\partial}{\partial r} \left(r \frac{d\bar{u}}{dr} \right) - \frac{\rho}{r} \frac{\partial r \bar{u}' v'}{\partial r} - \rho \frac{\partial \bar{u}' u'}{\partial x} \quad (4.8)$$

From figure 4.11b, we see that axial velocity in the core varies almost linearly along the axial direction (x) of venturi. Hence, velocity gradient is assumed to be a constant (c_1), and therefore, second derivative is ~ 0 . This is valid only at the axial position slightly away from the throat where \bar{u} peaks at the axis of contraction and not the wall.

$$\frac{\partial \bar{u}}{\partial x} = c_1; \quad \frac{\partial^2 \bar{u}}{\partial x^2} = 0 \quad (4.9)$$

Therefore equation 4.8 after re-arrangements:

$$\bar{u} \frac{\partial \bar{u}}{\partial x} = -\frac{1}{\rho} \frac{d\bar{P}}{dx} - \frac{1}{r} \frac{\partial r \bar{u}' v'}{\partial r} - \frac{\partial \bar{u}' u'}{\partial x} \quad (4.10)$$

$$\frac{\partial (\rho \frac{\bar{u}^2}{2} + \bar{P})}{\partial x} = -\frac{\rho}{r} \frac{\partial r \bar{u}' v'}{\partial r} - \rho \frac{\partial \bar{u}' u'}{\partial x} \quad (4.11)$$

Having eliminated viscous terms completely (term *IV* in equation 4.8), Bernoulli's theorem can now be applied along a streamline in the core of the contraction, i.e.

$$p_1 + \frac{1}{2} \rho U_{in}^2 = p_2 + \frac{1}{2} \rho u^2 = C \quad (4.12)$$

$$\rho \frac{\bar{u}^2}{2} + \bar{P} = C \quad (4.13)$$

where C is a constant computed along the same streamline. Thus, equation 4.11 reduces to equation 4.14

$$-\frac{1}{r} \frac{\partial r \bar{u}' v'}{\partial r} = \frac{\partial \bar{u}' u'}{\partial x} \quad (4.14)$$

From figure 4.16b, we can see that $\bar{u}' u'$ increases steadily along the axial direction. Hence, $\bar{u}' u'$ is assumed to vary linearly in axial direction, i.e., $\frac{\partial \bar{u}' u'}{\partial x} = c_2$. Thus,

$$\frac{1}{r} \frac{\partial r \bar{u}' v'}{\partial r} = -c_2 \quad (4.15)$$

$$r \bar{u}' v' = -\int_0^r c_2 r dr \quad (4.16)$$

$$r \bar{u}' v' = -c_2 \frac{r^2}{2} \quad (4.17)$$

$$-\overline{u'v'} = c_2 \frac{r}{2} \quad (4.18)$$

It can be seen from equation 4.18 that Reynolds shear stress varies as a function of r only in the pipe core. It is bound to be frozen in the core as it does not depend on the axial direction. Further, it varies linearly with radial distance in the core region. This freezing of turbulent shear stress is also observed in the current experimental results. see Reynolds shear stress ($\overline{u'v'}$) as shown in the figure 4.19b.

5

Experiments in long pipe: The effect of mildly rapid strain on turbulence

This chapter deals with experiments in the long pipe to study the effect of mildly rapid strain on pipe turbulence. The experimental setup along with the design of the experiment is explained in detail in section 5.1. To boost the credibility of experimental results, data validation is presented in section 5.2. This is followed by results and discussions in section 5.3.

5.1. Experimental setup

5.1.1. Flow facility

The layout of the flow facility employed in the current thesis is as shown in the figure 5.1. It consists of a smooth-walled, long, straight pipe made out of Polymethyl methacrylate (PMMA). It has an inner diameter (D) of 40.2 mm, outer diameter of 50 mm and total length of 28 m ($700D$). There are thus more than 500 diameters from the flow inlet to the test section ensuring that turbulent pipe flow is fully developed. The working fluid is water at room temperature ($23^{\circ}\text{C} \pm 2^{\circ}\text{C}$) and ambient pressure (1 bar). The entire pipe length (except the test section) is covered with isolating foam which serves as (i) thermal insulation, (ii) insulation against sunlight to prevent algae growth inside the pipe. The flow loop consists of a pump, settling chamber, honeycomb screens, contraction, reservoir and discharge chamber as shown in figure 5.1. The flow is driven by a centrifugal pump. The swirls in the flow generated by the pump as well as other flow disturbances are eliminated by a settling chamber and a series of honeycomb screens made of straws. Further flow disturbances are suppressed by an axisymmetric contraction of contraction ratio 1 : 9.

At about $540D$ from the flow inlet, the test section with contraction is fitted on the pipe via specially designed couplings. The test section is made of a PMMA block where the contraction profile is milled in with precision (see figure 5.2b). The contraction is preceded by a straight pipe section of length slightly over one pipe diameter ($1D$). Further, the length of the post-contraction straight section of a smaller diameter was constrained to $5D$ by the position of calibration vessel. The advantage of PMMA for the test section is that (i) It has high light transmission capabilities ($\sim 92\%$). (ii) The refractive index of PMMA is very close to that of water (~ 1.48). (iii) It can be machined to desirable form. When employing an optical flow measurement technique in pipes, it is often desirable to build a rectangular glass chamber with flat walls around the pipe to mitigate the light bending and lens effects due to the curved pipe wall. The current test section due to its geometry does not need such a chamber. It is attempted to make sure that the inner milled walls of the test section are finely polished to mitigate optical artefacts such as diffraction patterns due to gratings (refer to appendix B D). The mean flow rate is measured downstream of the test section with a magnetic inductive flow meter from KRONHE Altometer B.V. The flow rate is controlled using a potentiometer voltage regulator whose signal can be read on a LabView program. The program also measures the temperature of water via platinum resistance thermometer (PT100) that can be used to evaluate kinematic viscosity of water at that temperature. The kinematic viscosity is then used to compute mean flow Reynolds number (Re). The pipe ends in a

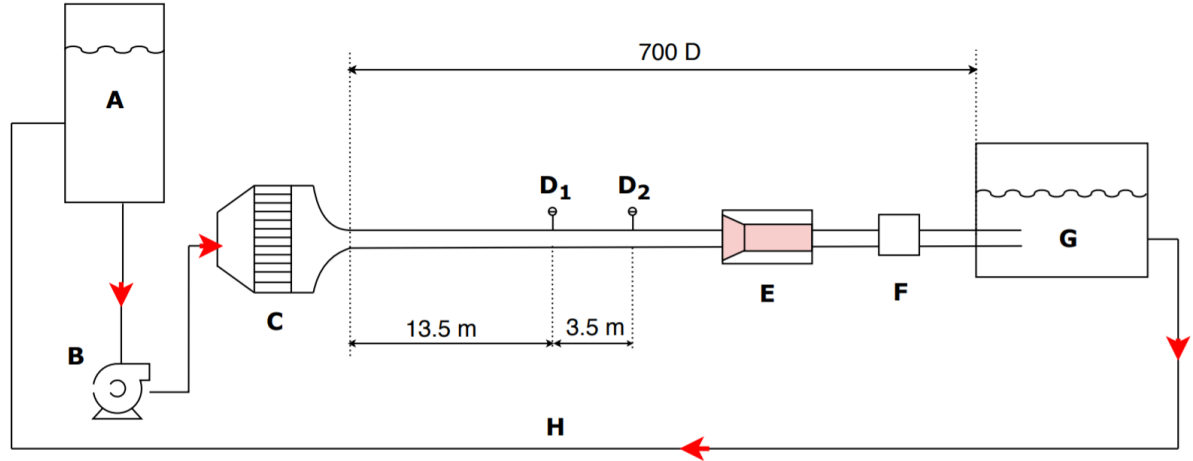


Figure 5.1: Long pipe flow facility at the laboratory for aero and hydrodynamics, Delft (The flow is from left to right). A : Reservoir, B: Centrifugal pump, C: Settling chamber followed by contraction, D_1 , D_2 : Pressure Taps, E: Test Section with contraction, F:Flowmeter, G: Discharge chamber, H: Return pipe.

discharge chamber where water is collected and recirculated through a return pipe of much bigger diameter: 250 mm. For further details about the flow facility, the reader is referred to Draad et.al. [85].

The pipe is fitted with several pressure taps over which pressure gradient can be measured using variable reluctance differential pressure transducer (Validyne Engineering). The pressure taps are present at locations D_1 and D_2 at a distance of 13.7 m and 17.2 m from the flow inlet respectively (see figure 5.1). Thus, pressure drop is measured over a pipe length of 3.5 m. Darcy-Weisbach friction factor (f_D) is computed from the measured pressure gradient and compared with Blasius friction factor (f_B) correlation for smooth pipes. For fully developed turbulent pipe flow, the measured friction factor (f_D) should concur with f_B . This approach was used to ensure that the turbulent pipe flow is fully developed ahead of contraction.

$$f_D = \left(\frac{dP}{dx} \right) \frac{2D}{\rho U_b^2} \quad (5.1)$$

$$f_B = \frac{0.316}{Re^{0.25}} \quad (5.2)$$

Here, D is the diameter of the pipe, ρ is the density of water at measured temperature, U_b is the bulk flow velocity of the flow computed from measured from the mass flow rate (\dot{m}) ($U_b = \dot{m}/A$), Re is flow Reynolds number, A is the cross-section area of the pipe. As can be seen from the figure 5.3a, measured values of the friction factor (f_D) are slightly higher but well within 2.5% of theoretical values (f_B). Hence, the flow is assumed to be fully developed ahead of the test section. The measured friction factor (f_D) is used to compute friction velocity (u^*) as per equation 5.3. The values of u^* calculated were within 2% of values obtained from Blasius's correlation (see equation 5.2).

$$u^* = \sqrt{\frac{f_D U_b^2}{8}} = \sqrt{\frac{D}{4\rho} \left(-\frac{dP}{dx} \right)} \quad (5.3)$$

5.1.2. Design of contraction

In order to experimentally study the effect of moderately rapid strain on turbulence, certain conditions are desirable viz. (i) The strain rate is rapid ($s^* > 1$). (ii) The strain rate is axisymmetric and irrotational (iii) Low acceleration parameter such that there is no relaminarization in the boundary layer ($K < K_{critical}$). (iv) There is no flow separation in post-contraction region.

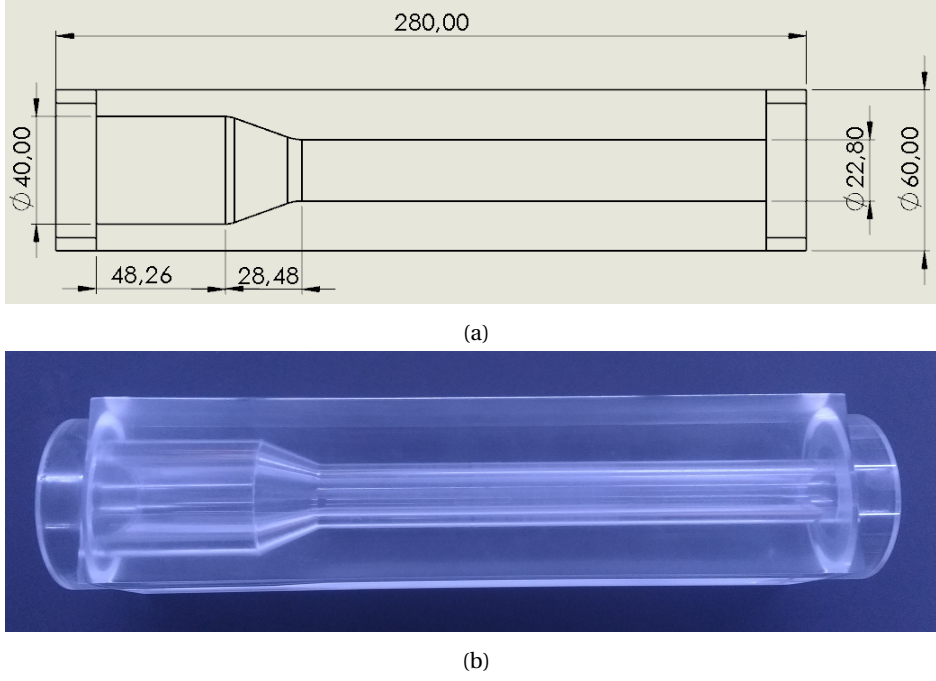


Figure 5.2: (a) Computer aided drawing of the designed test section (all dimensions are in mm). (b) Fabricated Test section with contraction (Component E in figure 5.1) made of PMMA.

Note that the strain rate (s^*) and K both scale directly with the mean velocity gradient ($\frac{d\bar{u}}{dx}$). Hence, rapid strain can lead to a higher value of acceleration parameter (K) leading to BL re-laminarisation which is undesirable (see equation 5.4, 5.6). The imposed mean strain (S) is normalised by the eddy turn over time of turbulence ($T_{\mathcal{E}}$). The design of contraction is approached from basic scaling arguments to satisfy above mentioned criterion. Few assumptions made are: (i) the turbulent kinetic energy (k) scales with \mathcal{U}^2 , (ii) the turbulent energy dissipation (ϵ) scales as $\mathcal{U}^3/\mathcal{L}$, where \mathcal{U} , \mathcal{L} are the turbulent velocity and length scale respectively. We introduce a surrogate non-dimensional strain rate (s^{*s}) defined by equation 5.5, where D is the diameter of pre-contraction straight pipe, $\bar{u}_{c,i}$ is the incoming mean centreline velocity. This was done since centreline velocity of the pipe could be estimated from PIV data with less uncertainty.

$$s^* = \frac{Sk}{\epsilon} \sim \frac{d\bar{u}}{dx} \frac{\mathcal{U}^2}{\frac{\mathcal{U}^3}{\mathcal{L}}} \sim \frac{d\bar{u}}{dx} \frac{\mathcal{L}}{\mathcal{U}} \quad (5.4)$$

$$s^{*s} = ST_{\mathcal{E}} = \frac{d\bar{u}}{dx} \frac{D}{u_{c,i}} \sim \frac{d\bar{u}}{dx} \frac{D}{u} \quad (5.5)$$

similarly,

$$K = \frac{\nu}{U_{\infty}^2} \frac{dU_{\infty}}{dx} \sim \frac{\nu}{u^2} \frac{d\bar{u}}{dx} \quad (5.6)$$

where ν is the fluid kinematic viscosity, U_{∞} is the free stream velocity outside the BL. Hence, U_{∞} scales with u in the centreline of pipe. Now, for the contraction, mean velocity gradient can be approximated as Ertunc et.al. [14]

$$\frac{d\bar{u}}{dx} \sim \frac{u(C-1)}{L_c} \quad (5.7)$$

where C is the contraction ratio, L_c is the length of contraction. Now, in the core region of pipe, $\mathcal{U} \sim u$ and $\mathcal{L} \sim D$. Substituting equation 5.7 in equation 5.4 and 5.6:

$$s^{*s} \sim \frac{d\bar{u}}{dx} \frac{L}{u} \sim \frac{u(C-1)}{L_c} \frac{D}{u} \sim \frac{(C-1)D}{L_c} \quad (5.8)$$

$$K \sim \frac{\nu}{u^2} \frac{d\bar{u}}{dx} \sim \frac{u(C-1)}{L_c} \frac{\nu}{u^2} \sim \frac{(C-1)\nu}{L_c u} \quad (5.9)$$

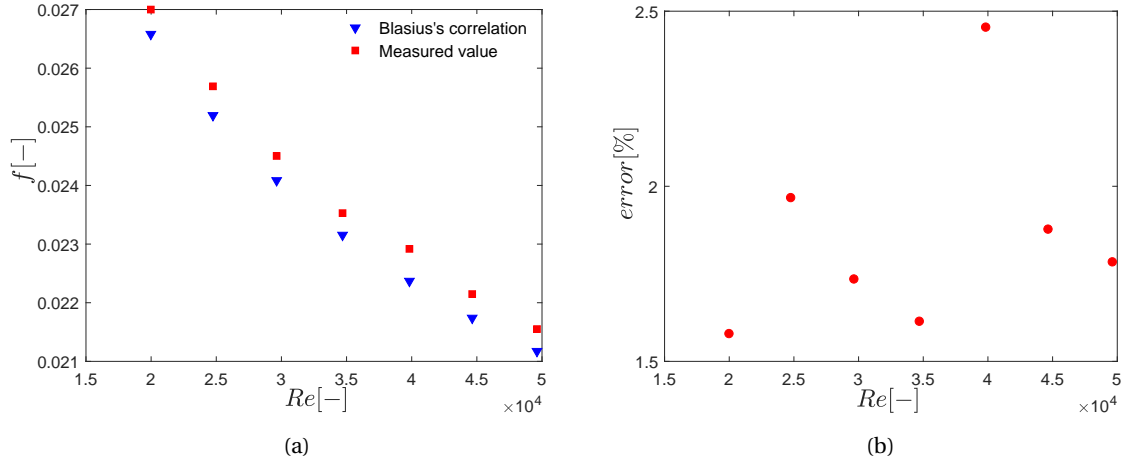


Figure 5.3: (a) Measured friction factor (f_D) compared with Blasius friction correlation for smooth pipes. (b) Relative % error in measurement (f_D) w.r.t. Blasius's theoretical expression (f_B). It might be important to note that different pressure transducers were used for $Re \leq 35,000$ and $Re > 35,000$ to consider working range of sensor.

$$s^{*s} = (K) \times Re \quad (5.10)$$

From equation 5.8, 5.9, it can be seen that non-dimensional strain rate (s^{*s}) is independent of flow condition and is dependent on the contraction geometry only. However, the acceleration parameter (K) is dependent on flow velocity and the contraction geometry. The aim was to increase the strain rate (s^{*s}) without increasing K . The s^{*s} can be increased by having large inlet diameter (D), large contraction (high C) or small contraction length (L_c). However, a large D/L_c ratio is known to result in undesirable flow separation. Furthermore, changing the above parameters to increase s^{*s} also results in a high K which again is undesirable. One way of achieving a high value of s^{*s} without affecting K is to have a higher inlet diameter (D) as K does not depend explicitly on D (see equation 5.9). This compromise was not possible with the current experimental facility as pipe diameter is fixed. Further, equation 5.10 indicates that Re is the deciding non-dimensional number which is limited in the current experimental setup.

Due to the above-mentioned reason and limited time scale of master thesis, it was decided to employ contraction design similar to that of Moene [53]. The final design of contraction is as shown in figure 5.4. The contraction ratio (C) designed is 3, L_c/D ratio is restricted to just over 0.5. The strain rate is mildly rapid ($s^{*s} \sim 0 - 3.2$). Note that the zero is defined at the start of the contraction such that negative x/D corresponds to pre-contraction region as shown in figure 5.4.

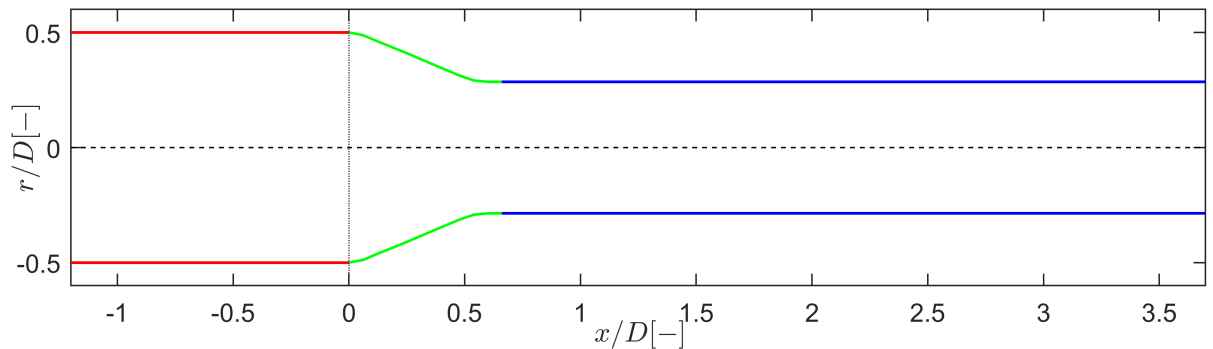


Figure 5.4: The contraction profile is shown in green; radial position vs. axial position. A fifth order polynomial can be fitted through the contraction profile with fit residual of $R^2 \sim 0.9999$.

5.1.3. Design of experiments

It was intended to study the evolution of high Re pipe turbulence when strained by a mildly rapid strain rate. The measurements were performed at three different Re , i.e. $Re_1 = 25,400$, $Re_2 = 34,981$, $Re_3 = 47,775$, where Re is based on the inlet diameter (D) and bulk velocity (U_b) at the inlet. At these Re , the friction velocity (u^*) was 0.0307 ms^{-1} , 0.043 ms^{-1} , 0.057 ms^{-1} respectively. Moreover, the wall unit thickness ($y^* = \nu/u^*$) at corresponding Re was 0.0279 mm , 0.0212 mm , 0.0161 mm respectively, where ν is the temperature dependent kinematic viscosity of water. Further, the measurements are performed separately in different Field of Views (FOVs): (i) To obtain a better spatial resolution with smaller FOV. (ii) To avoid bias in velocity data caused by the finite size of the cross-correlation window due to local gradient of velocity in the axial direction. (iii) To avoid optical artefacts at the region of change of cross-section (see appendix A). The measurements were performed in five different FOVs as shown in figure 5.5, viz. (i) Straight pipe section (red box), (ii) Inside the contraction (bright/emerald green), (iii) Downstream of contraction in straight section (cyan), (iv) Further downstream of contraction in the straight section (blue), and (v) Zoomed-in convergent section (dark/pickle green). Further, measurement over each FOV is a different experiment and hence, attempts were made to maintain the same Re in spite of the different temperatures (see table 5.1). Further, to avoid confusion, Re_1 , Re_2 , Re_3 , despite the slight difference in their exact values for each FOV, correspond to values of 25,000, 35,000, 47,700 in the results and discussion section 5.3.

FOV #	Re_1	Re_2	Re_3
01	25,398	34,981	47,775
02	25,488	35,835	47,799
03	24,371	35,155	46,314
05	25,437	35,483	50,016

Table 5.1: Test matrix for experiments in long pipe.

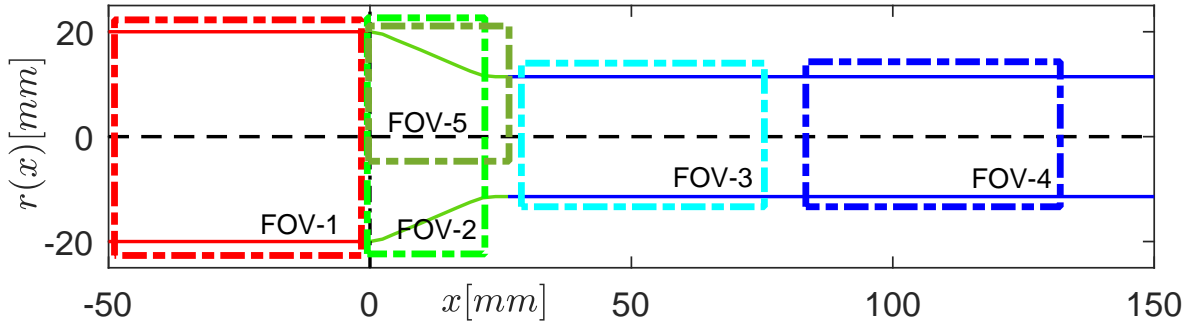


Figure 5.5: A schematic showing different FOVs over which measurements were performed. FOV-1: straight pipe upstream of contraction, FOV-2: Inside the contraction, FOV-3: Downstream of contraction, FOV-4: Further downstream of contraction, FOV-5: zoomed into contraction.

The image magnification obtained is the same for FOV-1 and FOV-2 i.e. 0.5. However, for FOV-3 and FOV-4, image magnification is increased to 0.6. Further, FOV-5 is imaged with a magnification value of 0.7. In a typical planar PIV, particle image magnification is diffraction limited. However, as the object distance decreases geometric magnification becomes important as well. The image magnification (M) is defined as the ratio of image distance (d_i) to object distance (d_o). Thus, magnification can be increased by either increasing d_i or decreasing d_o . In the case of FOV-5, magnification is augmented by placing the adaptor ring between the camera body and lens such that d_i is increased. While setting up the experiment, it was made sure that the camera could be traversed in all three degrees of freedom to set the required FOV easily. Similarly, optics for laser sheet were mounted such that they could be traversed easily to cater to disparate FOVs. The undesirable reflections in the particle images were blocked by black matt-finish screens. However, the reflections close to

the wall and diffused illuminations close to the walls could not be avoided which resulted in the data close to wall being corrupt.

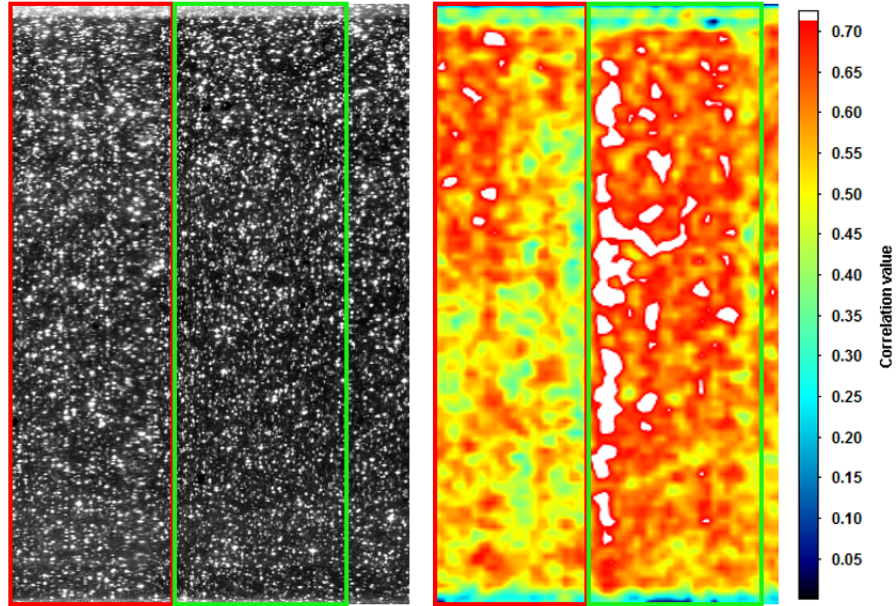


Figure 5.6: A typical particle image with optical artefact in FOV-3. Notice vertical stripping and local distinct blurry appearance of particle images on the left end of particle image (red box). At these corresponding points, cross-correlation coefficient drops to as low as 0.3 resulting in low signal to noise ratio. However, region of relatively good correlation is shown in green box.

At this point, it is important to mention that the particle images were slightly corrupted due to the presence of blurry regions on the inner wall of the test section and grating on the inner wall of the pipe due to the machining tool marks (see figure 5.6). This has resulted in particle images appearing locally bigger. Further, the gratings due to the machining tool marks on the inner surface of the test section have resulted in diffraction pattern of particle images (i.e. multiple particle images of fading intensity in the streamwise direction) and dark strips in the image due to slight divergence of laser sheet about these gratings. All these factors resulted in the loss of correlation and peak locking bias errors in the particle image displacements (mainly due to stretching of particle images). Due to time constraints, it was not possible to send back the test section to the manufacturer given it had already been reworked twice. Hence, to mitigate this effect, the camera was slightly defocused on the particle such that the diffraction patterns appear as one particle, thus particles were imaged over 7-8 pixels mildly stretched in the streamwise direction. This has resulted in a lower resolution of velocity field and a slight peak locking bias error. However, there are few regions within these FOVs (2,3,4) where the correlation peak is distinct and strong (see figure 5.6). The profiles of various quantities presented later were evaluated in such regions. 2-D spatial two-point correlations, however, were evidently corrupted due to the regions of low cross-correlation caused by optical artefacts. This problem was very severe in FOV-3,4. FOV-2,5 had such blur regions but were not as severe as former. Further, FOV-1 was only mildly affected by the optical artefacts. See appendix D for the details. Attempts have been made to get the best possible data with current limitations of the experimental setup.

5.1.4. Measurement Technique: PIV

Planar (2D-2C) PIV is used to get qualitative and quantitative information on the flow. It was intended to resolve large and small scales of turbulence via two-point statistical correlation on velocity fluctuations and vorticity respectively. This requires turbulent statistics to be well converged along with the mean flow statistics. Hence, it was decided to perform low-speed measurements such that each pair of particle images is statistically independent of the next. Further, to resolve small scales, high-resolution imaging was undertaken. The flow is seeded with tiny hollow glass tracer particles having a mean diameter of $12 \mu\text{m}$ and a

nominal density of $1.1 \pm 0.5 \text{ g/cm}^3$ (Sphericell 110P8, Potter Industries). The particles are expected to follow the flow faithfully due to low particle Stokes number ($< O(10^{-1})$) even at the highest Re case. The $r-x$ plane of the pipe is illuminated with a thin laser sheet of width $\sim 50 \text{ mm}$ and thickness $\lesssim 1 \text{ mm}$ which is formed by passing a Gaussian laser beam through a series of optics such as plane mirrors, spherical convex lens and plano-concave (cylindrical) lens. The dual-head Nd:YAG laser (Litron Laser Ltd.) used is capable of producing a laser beam with per pulse energy of 100 mJ at a wavelength of 532 nm. The laser sheet is introduced from the top (w.r.t. pipe) and lies in $r-x$ plane as mentioned before, cutting through the axis of pipe (see figure 5.7).

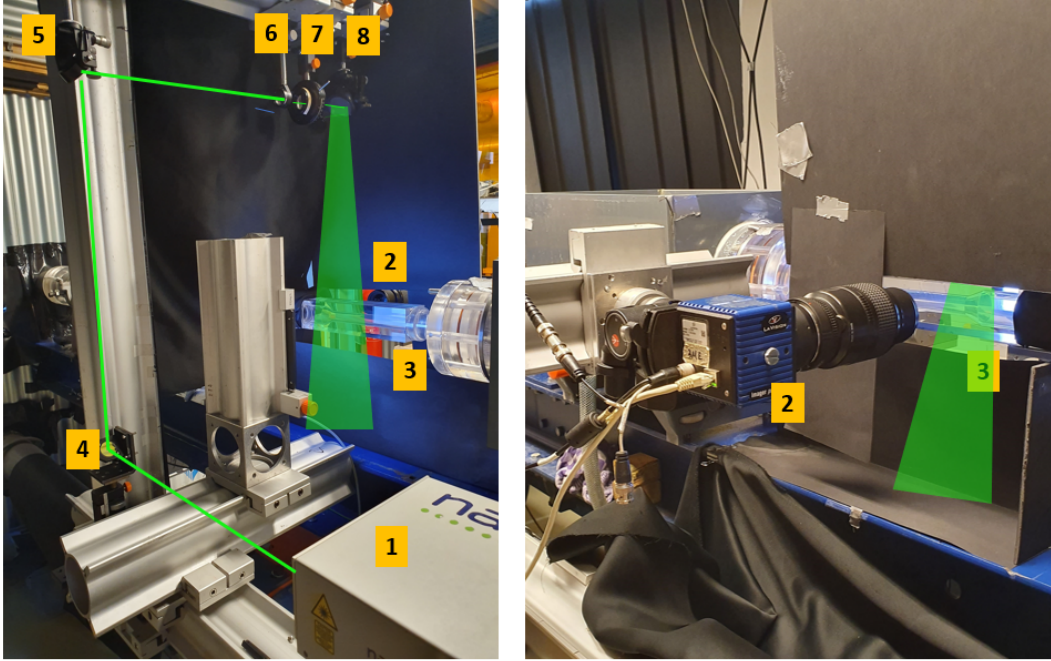


Figure 5.7: Setup for a planar PIV measurement; 1: Dual head Nd:YAG Laser, 2: High resolution camera, 3: Test Section, 4, 5, 8: Plane mirror, 6: Spherical convex lens, 7: Plano-concave cylindrical lens. Note also that the cartoon of laser sheet is shown.

The particle images are taken by a high-resolution LaVision LX pro (16 MegaPixel), 12-bit camera placed perpendicular to the laser sheet. The sensor size of the camera is $4920 \text{ pixels} \times 3280 \text{ pixels}$ at a pixel pitch of $5.5 \mu\text{m}$. The camera is used in combination with F105 mm Micro-Nikkor objective producing optical magnification of $\sim 0.4 - 0.7$ depending on the field of view (see subsection 5.1.3). Note that a ring was placed between camera body and lens in FOV-5 to increase image distance maintaining the same object distance thus enhancing image magnification. The f stop ($f^\#$) of lens is set to 5.6 such that particles are imaged over 3 – 4 pixels [20] at a good image intensity. For the FOV-3 and FOV-4, $f^\#$ was set to 8 so that particles are imaged over 7-8 pixels due to optical artefacts in the test section as mentioned before. The Programmable Timing Unit (PTU) synchronises camera and laser pulse triggers. The laser pulse separation (Δt) is a very important parameter in PIV and is set to produce particle image displacements between 14 to 26 pixels. This is higher than conventional particle image displacements (8-15 pixels) [20]. This was done to resolve turbulent velocity fluctuations well since velocity fluctuations are arrived at after subtracting the instantaneous velocity from mean velocity. Hence, higher particle displacements (in pixels) ensure that velocity fluctuations are above the noise level of PIV ($\sim 0.1 \text{ pixel}$). Further, a larger range of velocity due to the axial velocity gradient requires a higher range of particle image displacements (in pixels). However, this limits the spatial resolution in velocity data, i.e., one can not go down to smaller IW size such as (24×24) or $(16 \times 16) \text{ pixel}^2$. The image acquisition frequency is set to maximum allowable double frame acquisition frequency of the camera (0.7 Hz) and 3000 image pairs are acquired for each measurement.

The raw particle images obtained were enhanced by applying a min-max filter of length 6 pixels to achieve good contrast in particle images. Note that for FOV-3 and FOV-4, the min-max filter of 9 was used due to larger particle image sizes. Further, intensity averaged cross-correlation is performed over the interrogation

window (IW) to evaluate velocity vector fields using DaVis 8.4.0. The maximum particle image displacement (in pixels) of 25 was maintained, thus a multipass cross-correlation was performed wherein the first pass of 96×96 (pixel²) (50 % overlap) was followed by three passes of 32×32 (pixel²) (50 % overlap). This was done to obey one-fourth rule i.e. IW should be at least four times the particle image displacements (in pixels) [20]. For FOV-3,4 final pass of 48×48 (pixel²) with 50% overlap was maintained to acquire acceptable number of valid vectors. Median filtering with universal outlier detection (Westerweel et.al. [78]) was performed over the velocity fields to remove a group of unphysical velocity vector which was later replaced by linear interpolation of neighbouring velocity vectors. No other smoothing filters were applied to the velocity vector fields. Overall, the percentage of good vectors (first and second choice together) were above 98% in all the measurements. The histogram of the fractional part of particle image displacements was plotted to check for any bias towards integer displacements. This confirmed that there were slight peak lock errors in FOV-2,3,4,5 due to the previously mentioned optical artefacts. Finally, the vector spacing of 0.209 mm in FOV-1,2. 0.207 mm in FOV-3,4 and 0.143 mm in FOV-5 is achieved. A sample instantaneous velocity vector field in FOV-1 and FOV-5 is shown in figure 5.8

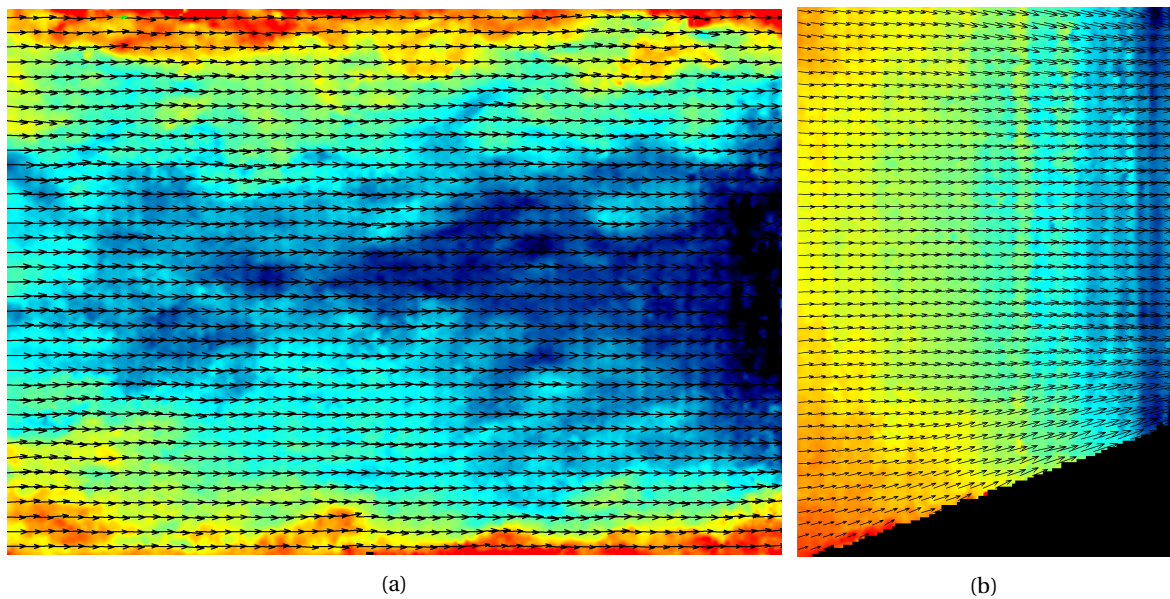


Figure 5.8: (a) Instantaneous velocity vector field in FOV-1. (b) Instantaneous velocity vector field in FOV-5. Note that every fourth vector is shown in the field for the sake of clarity and the flow is from left to right.

5.2. Data validation

To assess the reliability and quality of the data measured in this thesis, mean and turbulent statistics in the fully developed straight pipe section ahead of contraction (FOV-1) were compared with the widely accepted benchmark data generated by Toonder et.al. [73]. Toonder's data at $Re = 24,580$ has been accepted as a reference data and compared with the current measurement at $Re = 25,400$ (current Re is higher by 3.3%). The profiles are plotted around half a diameter before the contraction starts ($x/D = -0.45$ to -0.5). Further, the profiles are spatially averaged over multiple radial slices (along the axis). The mean axial velocity (\bar{u}) and its fluctuations u_{rms} ($\sqrt{u'u'}$), v_{rms} ($\sqrt{v'v'}$) have been normalised by wall friction velocity (u^*) computed from the pressure drop measurements (see section 5.1). Moreover, Reynold's shear stress is normalised by the square of friction velocity (u^{*2}). The radial distance from the center of the pipe (r) is normalised by pipe radius (R) for outer scaling whereas the wall-normal distance (y) is normalised by wall unit thickness ($y^+ = \frac{yu^*}{\nu}$) for inner scaling. Note that, ν is the temperature-dependent kinematic viscosity of water.

The mean axial velocity matches fairly well with the reference data in the core region of pipe but is lower by 1.6%. The deviation from reference data increases towards the wall ($r/R = 0.8$, $y^+ = 130$), where the mean velocity is lower by 2.8%. The turbulent statistics show a higher deviation as compared to mean statistics as expected. For streamwise velocity fluctuations, the measured value is lower by 11.1% at the center of the pipe

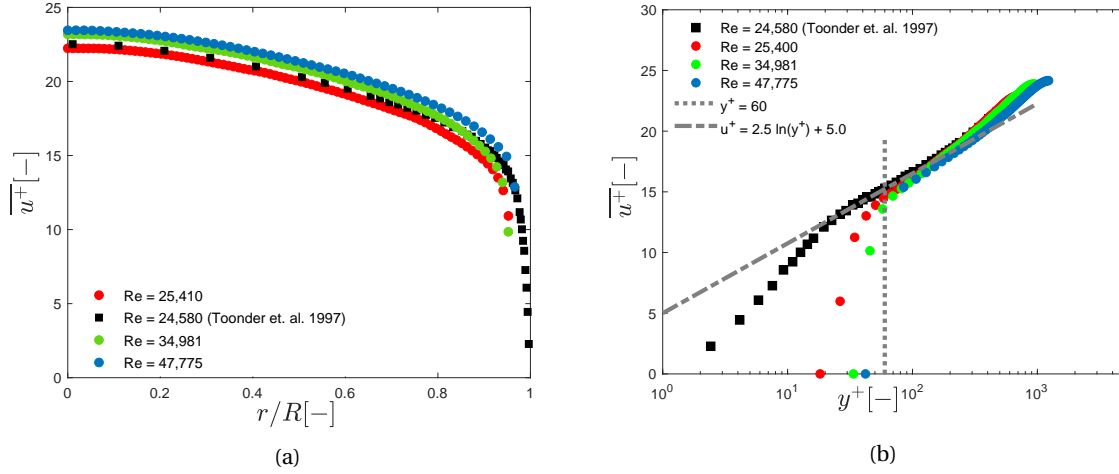


Figure 5.9: (a) Mean axial velocity profile ($\overline{u^+} = \frac{\overline{u}}{u^*}$) vs radial distance ($\frac{r}{R}$) (outer scaled with pipe radius). (b) Mean axial velocity profile ($\overline{u^+}$) vs wall normal distance (y^+) (inner scaled with wall units).

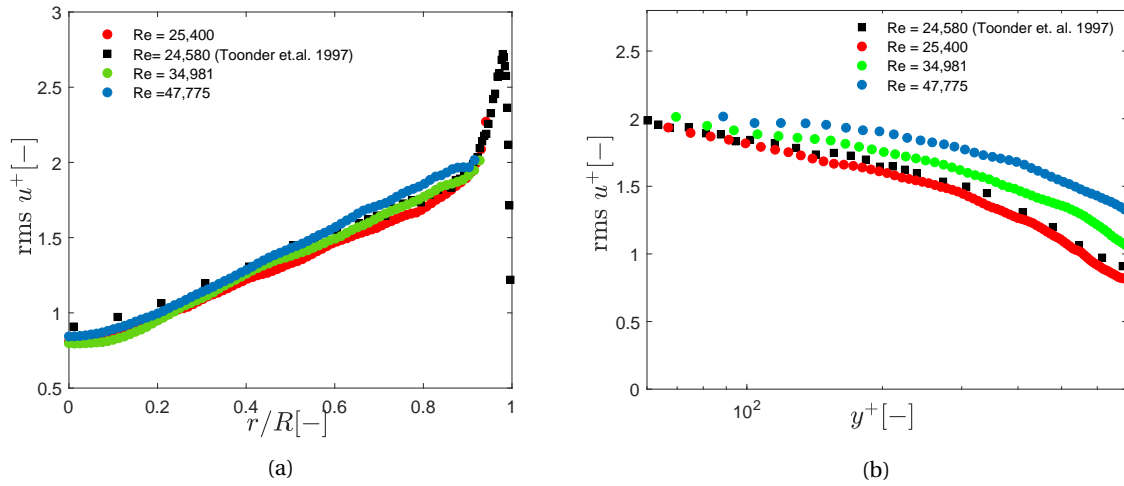


Figure 5.10: (a) Stream-wise velocity fluctuation, ($\text{rms } u^+ = \frac{\sqrt{u'u'}}{u^*}$) vs radial distance ($\frac{r}{R}$) (outer scaled with pipe radius). (b) Rms u^+ vs wall normal distance (y^+) (inner scaled with wall units) at different Re .

whereas, at $r/R = 0.81$, the deviation is within 3.5%. Similarly, for transverse fluctuations, at the centre of the pipe, the measured value is lower by 3.3% and closer to the wall ($r/R = 0.81$), the values are within 5.7%. The Reynolds's shear stress in the core region of the pipe has good agreement with the deviation of less than 0.5%, however, closer to the wall ($r/R = 0.8$), measured shear stress is lower by almost 8%.

It is seen that the measured data is consistently lower than the reference data of [73] with higher deviation close to the pipe walls. This under-estimation can be attributed to the bias error due to spatial filtering in the cross-correlation IW itself. Further, the region close to the pipe wall could not be measured or well resolved due to reasons such as: (i) Large velocity gradients, (ii) Finite interrogation window size, (iii) Possible bias in detecting pixel displacement near the wall due to spatial averaging over the IW itself and hence in velocity, (iv) Glaring close the pipe walls, (v) The curvature of wall, (vi) Settling of PIV particles on the pipe walls.

The random error in the measured data can be quantified by the time-averaged two-point correlations as a function of axial separation. The absence of an appreciable sharp noise peak at zero separation ensures that measurement has low random noise (see figure 5.13a). Further, at all Re , the spatial extent of correlation (R_{uu}) is symmetric and spans up to one pipe radius. This confirms a well-known hypothesis that large scales

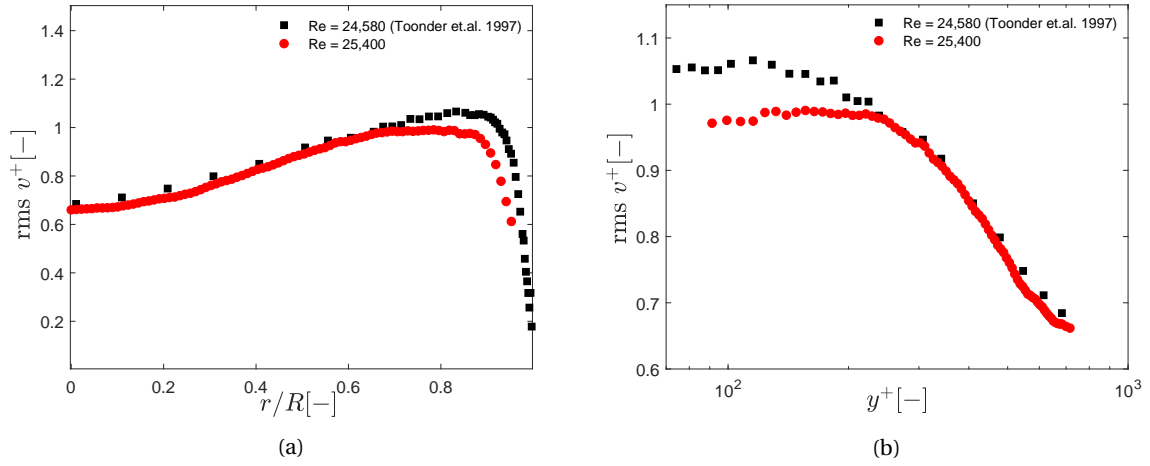


Figure 5.11: (a) Transverse velocity fluctuation ($\text{rms } v^+ = \frac{\sqrt{v'v'}}{u^*}$) vs radial distance ($\frac{r}{R}$) (outer scaled with pipe radius). (b) Rms v^+ vs wall normal distance (y^+) (inner scaled with wall units)

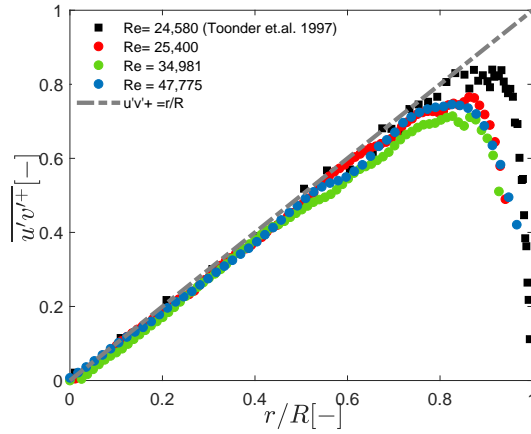


Figure 5.12: Reynolds shear stress normalised by u^{*2} ($\overline{u'v'^+} = \frac{\overline{u'v'}}{u^{*2}}$) vs radial distance normalised by pipe radius (outer scaled) at different Re .

of turbulence scale with fluid dynamic length scale, i.e., pipe diameter (D) in pipe flows irrespective of flow Re . The long tails in correlation could not be measured due to the smaller extent of FOV-1 constraint by the test section itself. (see figure 5.5). The correlations on out of plane vorticity ($R_{\omega\omega}$), which are a measure of small scales, show that as Re increases (see figure 5.13b), $R_{\omega\omega}$ decreases and hence small scales get smaller. Moreover, these correlations have long tails of positive correlation which are signature of a spatially organised small scales alongside large scale turbulent structures in the form of sheets or layers (Eisma et.al. [86], Gul et.al. [87]). Despite few data points contributing to the vorticity correlation, the data can be trusted since it spans over multiple cross-correlation IWs. Having assessed the qualitative and quantitative consistency of measured data in straight pipe, turbulence subjected to strain is discussed in the following section.

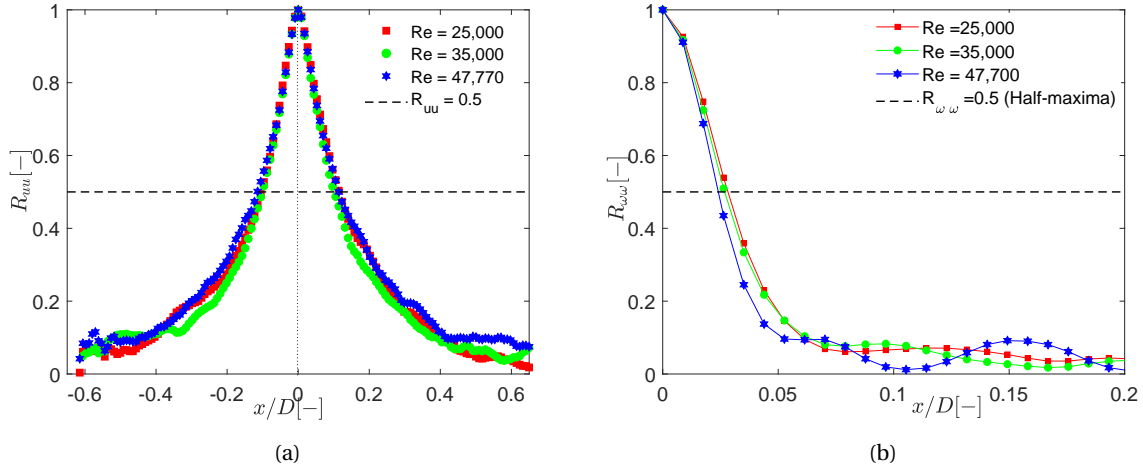


Figure 5.13: (a) Two-point correlation of velocity fluctuations (R_{uu}) vs axial separation. (b) Two-point correlation on out of plane vorticity ($R_{\omega\omega}$) vs axial separation. Both the quantities have been normalised by their respective covariance.

5.3. Results and discussions

This section presents the results of experiments performed in turbulent pipe flow strained by axisymmetric contraction producing irrotational mildly rapid strain. As opposed to large contraction ($C \sim 4 - 9$) in chapter 4, contraction employed here is milder i.e. ($C \sim 1 - 3$). Naturally, the first step is to characterise the rapidity of strain imposed by contraction on the turbulence. Since the bulk velocity could not be measured with good accuracy inside the contraction using PIV measurements, centreline velocity estimated with low uncertainty is used throughout this section as a measure of outer scale velocity. Further, axial distance is normalised by the pipe diameter (D) with origin defined at the start of the contraction. As can be seen in the figure

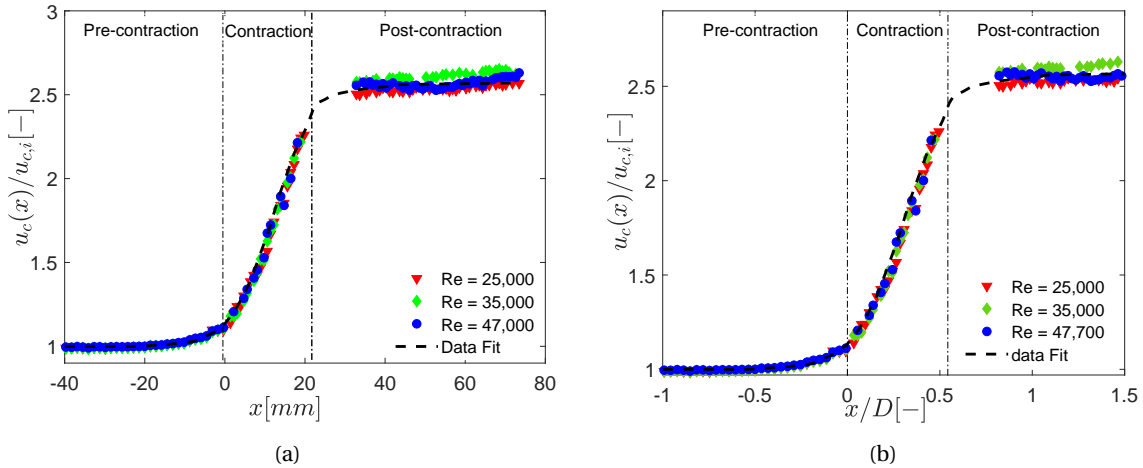


Figure 5.14: Mean axial velocity at the centreline normalised by the incoming centreline velocity at the centre of contraction as a function of axial distance (a) (x) unscaled. (b) scaled (x/D).

5.14, averaged centreline velocity ($\overline{u_c}(x)$) normalised by pre-contraction incoming centreline velocity ($\overline{u_{c,i}}$) starts increasing before the contraction. Approximately, half a diameter ($x = -D/2$) before the contraction, centreline velocity shows an increase. Prior to that, centreline velocity is fairly constant from $x/D \sim -1$ to -0.5 . Hence, in this region, pipe flow is treated as fully developed. Inside the contraction, centreline velocity increases steeply as expected due to the acceleration. Later, in the post-contraction region, velocity increases very faintly before assuming a constant value. The centreline velocity ratio along the axis of contraction is used to define the local contraction ratio (C) along the axis of contraction as $C = \overline{u_c}(x)/\overline{u_{c,i}}$.

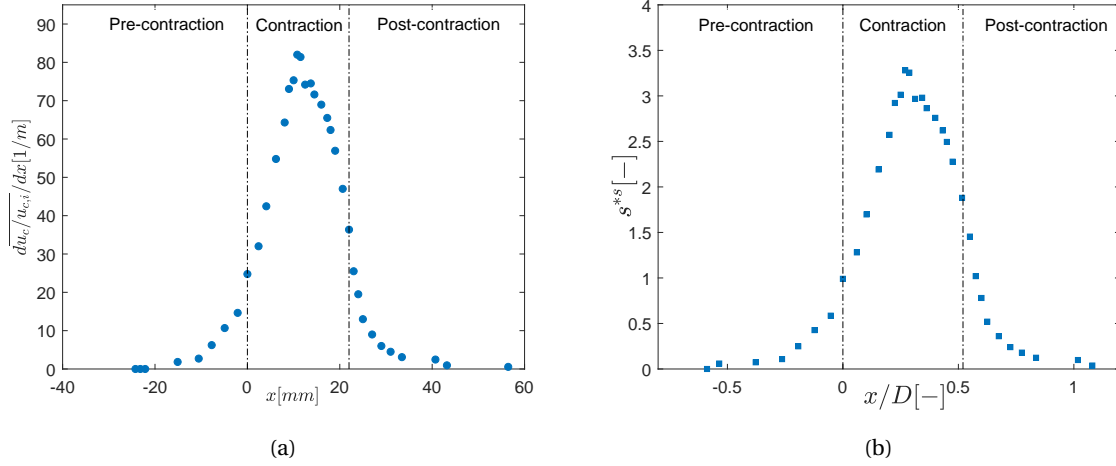


Figure 5.15: (a) The gradient of the mean centreline velocity as a measure of mean strain rate. (b) Non-dimensionalized strain rate (s^{*s}) along the centreline of contraction.

Inside the contraction, C attains a maximum value of almost 2.4, while the area based contraction ratio designed in the geometry was around 3. However, note that the designed contraction ratio (C) is based on the bulk velocity ratio. Further, in the post-contraction region, flow slowly accelerates to a velocity ratio of ~ 2.7 at about $x/D = 1$. This is manifested in velocity gradients as shown in the figure 5.15a. The gradient starts increasing at $x/D \sim -0.5$, gains a maximum inside the contraction followed by a decrease in post-contraction region. However, it does not return to zero velocity gradient until $x/D \sim 1$. As mentioned before, a surrogate of non-dimensional strain rate (s^{*s}) is defined as per equation 5.11 along the axis of the contraction. s^{*s} attains a maximum value of 3.2 as shown in the figure 5.15b. Recall, that the mean strain is rapid when the time scale for which it acts on the turbulence is smaller than integral time scale of turbulence itself i.e. $s^{*s} \geq 1$. Since the value of s^{*s} is greater than 1 but not significantly. Hence, the imposed mean strain rate is mildly rapid if not rapid as per the definition given by [7].

$$s^{*s} = ST_E = S \frac{D}{u_{c,i}} \quad (5.11)$$

5.3.1. The effect of strain on pipe flow statistics

Having established that the imposed strain rate is mildly rapid, the effect of the strain on the mean and turbulent statistics are reported with a preliminary analysis. The data has been presented for three different flow Reynolds number; $Re \sim 25,000, 35,000, 47,700$ to study the effect of Re on turbulence evolution. Further, to study the evolution of turbulence when strained, five different radial profiles have been selected such that L0 ($x/D \sim -0.55$) is in the pre-contraction straight pipe, L1 ($x/D \sim 0.2$), L2 ($x/D \sim 0.46$) are inside the contraction, while L3 ($x/D \sim 0.75$), L4 ($x/D \sim 1.75$) are further downstream of contraction (post-contraction). See figure 5.16 for the schematic. The mean velocity and turbulent velocity fluctuations have been normalised by

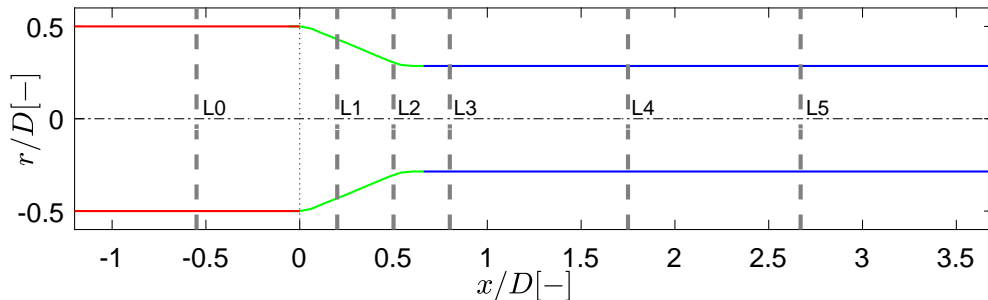


Figure 5.16: A schematic showing axial positions along which profiles have been plotted in the subsequent sections.

the centreline velocity of incoming fully developed pipe flow ($\overline{u_{c,i}}$) or local mean centreline velocity ($\overline{u_c(x)}$). Further, the radial distance (r) at each profile has been normalised by the local radii (R) such that (r/R) always spans from 0 to 1 at every axial location. As mentioned before, flow topology has been divided as pre-contraction, contraction and post-contraction regions. The sole purpose of reporting pre-contraction flow statistics is that it serves as a reference for comparison. The following subsection focuses on the evolution of turbulence inside the contraction while next subsection will deal with the turbulence evolution in post-contraction straight pipe region.

5.3.2. Turbulence evolution by mildly rapid strain rate

First we study the effects of axisymmetric strain on the mean flow. It is seen that the effect of mean strain is to flatten out the mean axial velocity (\overline{u}) profile as shown in the figure 5.17. As a result, the gradient of

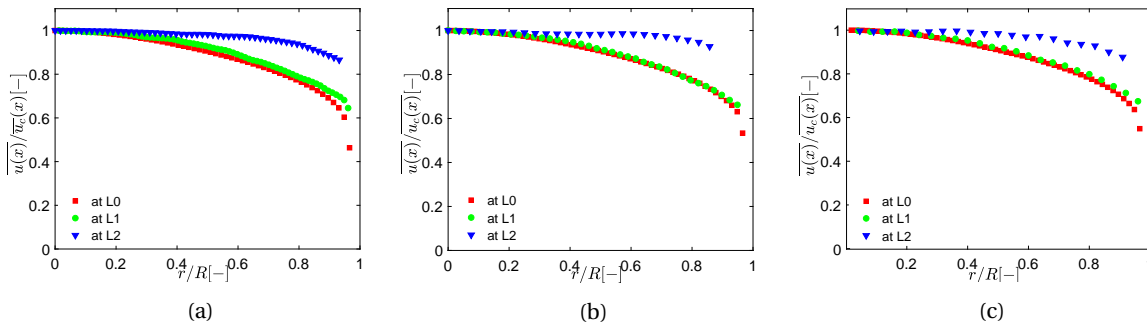


Figure 5.17: Mean axial velocity profile normalised by centreline velocity at different axial positions i.e. L0, L1, L2 for (a) $Re=25,000$. (b) $35,000$. (c) $47,700$.

velocity in the near-wall region increases to conserve the bulk mass and hence velocity. This is due to the added pressure gradient imposed on the flow by contraction which acts uniformly over the entire radius of the pipe in combination with a no-slip boundary condition that has to be satisfied at the pipe wall. Due to the contraction, the mean radial velocity which was zero in the pre-contraction region starts developing from the wall into the core of the pipe. Except for a thin layer close to the wall, the mean radial velocity profile shows an almost linear behaviour along the radial direction (r) at L1 while it is slightly distorted further inside the contraction at L2. However, the linear trend is faithfully followed in the core region (see figure 5.18), where the mean flow is axisymmetric ($\partial/\partial\theta = 0$) and continuity dictates: $\partial\overline{u}/\partial x + (1/r)(\partial r\overline{v})/\partial r = 0$. With almost linear variation of u along axial direction (x) at the centreline, linear variation of radial velocity (v) in the radial direction is justified (see figure 5.14).

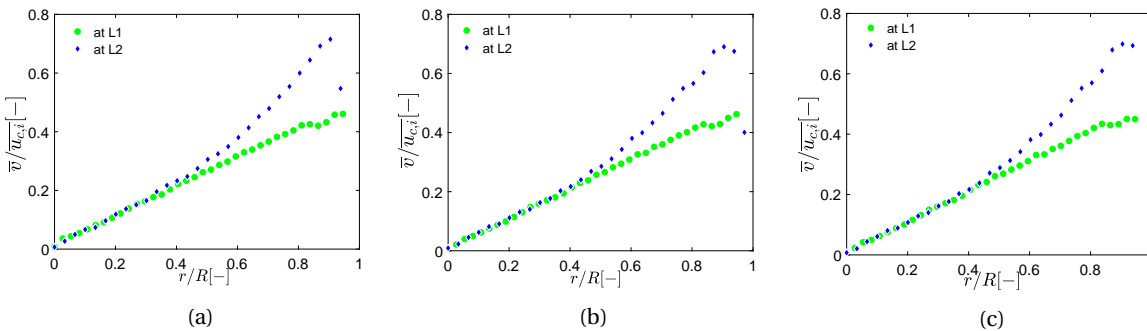


Figure 5.18: (a) Mean radial velocity profile normalised by local centreline velocity at different axial positions L0, L1, L2 for (a) $Re=25,000$. (b) $35,000$. (c) $47,700$.

The presence of axisymmetric contraction significantly affects the turbulent statistics as well. Figure 5.19 shows the evolution of streamwise turbulent fluctuations inside the contraction. It is seen that $\sqrt{u'u'}$ when

normalised by incoming centreline velocity decreases throughout the pipe radius progressively inside the contraction. Further, the turbulent intensity is computed by normalizing w.r.t. the local centreline velocity ($\overline{u_c(x)}$). Evidently, streamwise turbulence intensity decreases inside the contraction continuously as shown in figure 5.20. At the same time, absolute transverse velocity fluctuations ($\sqrt{v'v'}$) when normalised by incoming cen-

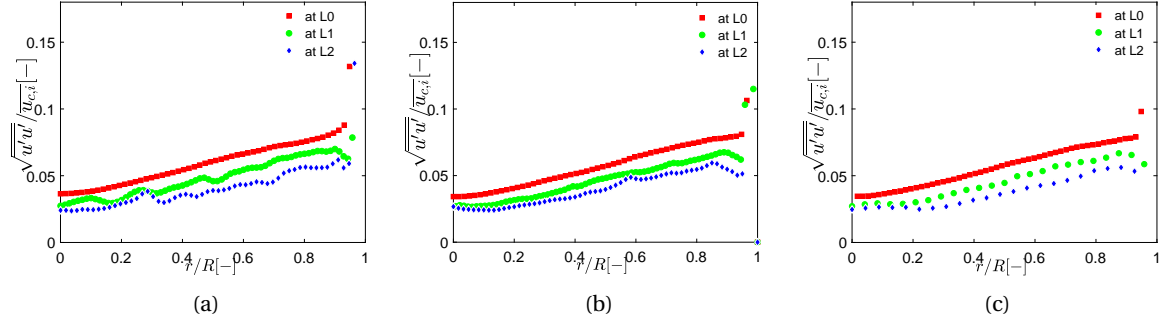


Figure 5.19: (a) Streamwise velocity fluctuations $\sqrt{u'u'}$ (urms) normalised by incoming centreline velocity ($\overline{u_{c,i}}$) at different axial positions i.e. L0, L1, L2 for (a) $Re=25,000$. (b) 35,000. (c) 47,700.

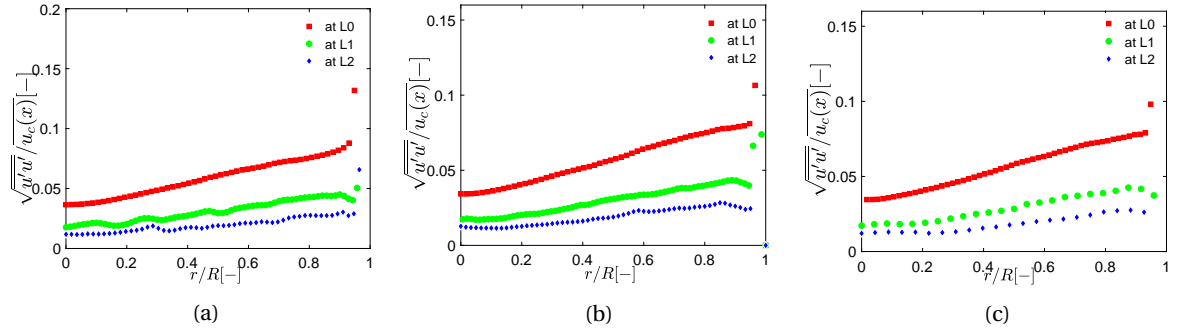


Figure 5.20: (a) Streamwise turbulent intensity $\sqrt{u'u'}$ profile normalised by local centreline velocity ($\overline{u_c(x)}$) at different axial positions L0, L1, L2 for (a) $Re=25,000$. (b) 35,000. (c) 47,700.

treline velocity ($u_{c,i}$) shows a progressive increase throughout the span inside the contraction as shown in figure 5.21. Further, figure 5.22 shows that transverse turbulent intensity ($\sqrt{v'v'}/\overline{u_c(x)}$) progressively decrease inside the contraction. Thus, the net effect of strain or acceleration is to suppress the turbulence (stream-wise and transverse fluctuations), however, this effect is due to the normalization employed w.r.t. local centreline velocity which increases inside the contraction due to the acceleration.

At all the measured Re ($\sim 25,000$, 35,000, 47,700), turbulent fluctuations normalised by $\overline{u_{c,i}}$ or $\overline{u_c(x)}$ display a similar behaviour suggesting that the effect of Re is absent (see figure 5.19, 5.20, 5.21, 5.22). This holds only for the core region of the pipe, however, very near to the wall, no comments can be made due to the lack of data. It appears that the components of normal Reynolds stress ($\overline{u'u'}$, $\overline{v'v'}$) exhibit a distinct response to the strain such that the streamwise component decrease and transverse component increase upon straining. It is important to recall that the square of turbulent velocity fluctuations scale with turbulent kinetic energy (TKE). Hence, this can be attributed to the inter-component mutual exchange of energy as a consequence of imposed strain by the contraction. This increase of transverse component of turbulent energy at the expense of streamwise component is qualitatively in agreement with the linear RDT [4, 30] and previously reported experimental studies in strained wind tunnel [7, 8, 14, 68].

Due to the rapidity of the strain, linear RDT is expected to be valid (see section 2.7.3). In order to quantitatively compare this mutual exchange of energy with the linear theory, normal Reynolds stresses ($\overline{u'^2}$, $\overline{v'^2}$) at the axis of contraction is normalised by the normal Reynolds stresses at the axis of fully developed straight pipe section ($\overline{u_{c,i}^{\prime 2}}$, $\overline{v_{c,i}^{\prime 2}}$) respectively and shown against the local contraction ratio (C) defined before. Note

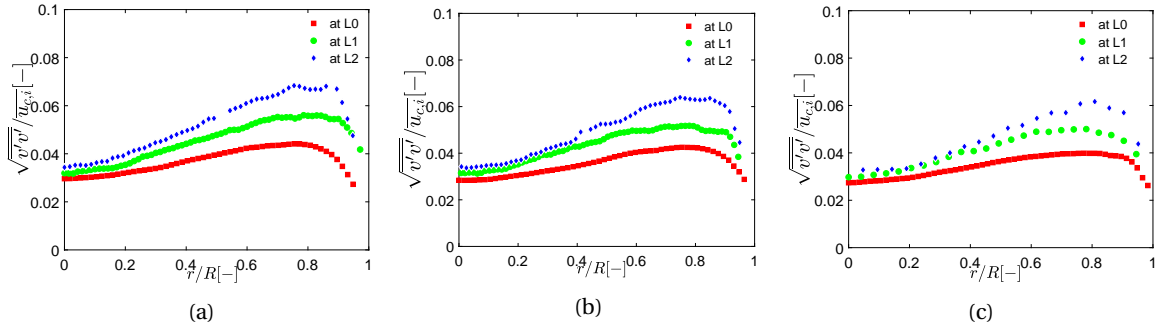


Figure 5.21: (a) Transverse velocity fluctuations $\sqrt{v'v'}$ (rms) profile normalised by incoming centreline velocity ($\overline{u_{c,i}}$) at different axial positions i.e. L0, L1, L2 for (a) $Re=25,000$. (b) $35,000$. (c) $47,700$.

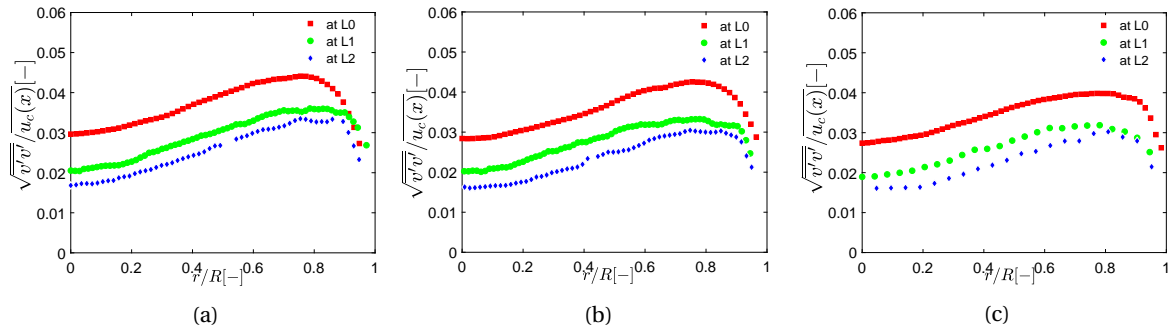


Figure 5.22: (a) Transverse turbulent intensity $\sqrt{v'v'}$ (rms) profile normalised by local centreline velocity ($\overline{u_c(x)}$) at different axial positions i.e. L0, L1, L2 for (a) $Re=25,000$. (b) $35,000$. (c) $47,700$.

that the local contraction ratio is a function of axial distance (x) from the start of the contraction. To facilitate better comparison, the predictions of RDT (equations 2.30, 2.31) are also plotted in the figure 5.23 along with published data of Hussain and Ramjee [6, 40], Uberoi et.al. [5, 13], Ertunc et.a. [14]. The agreement of streamwise normal Reynolds stress is good, however, it is important to realise that the current definition of C is based on centreline velocity when it should be based on the bulk velocity. The contraction ratio based on centreline velocity should be slightly underestimated w.r.t. bulk velocity ratio due to the flattening of the mean velocity profile. However, the trend of $1/C^2$ in streamwise stresses is consistent with RDT. Further, transverse stresses are lower than that predicted by linear RDT, but, once again the linear trend predicted by RDT is maintained. Moreover, the effect of Re is negligible as also suggested by RDT. The observed deviation of current data w.r.t. RDT can be attributed to the assumptions with which RDT is arrived at (see section 2.7.3). The most important reason according to the author is the mild rapidness of strain in the current setup due to which non-linear terms such as viscous dissipation omitted in RDT can become important. Ertunc et.al. [42] has experimentally shown that at high strain rates ($s^* \sim 70$) evolution of normal Reynolds stress agrees well with RDT in a wind tunnel grid turbulence. Further, current data lies in-between data for less rapid strain rate ($s^* \sim 1$ [6, 40]) and more rapid strain rate ($s^* \sim 5, 20, 200$ [5, 13]), thus, suggesting that deviation of transverse Reynolds stress with RDT could be due to the non-rapidness of mean strain rate. Further, pipe flow being wall-bounded and incoming length scales (\mathcal{L}) being of the order of pipe diameter (D), large scales can get confined by wall due to blocking effect [88]. This can limit the inter-component transfer of turbulent energy and even suppress turbulence [39].

Despite the mild rapidity of strain, the degree of closeness of measured data with RDT predictions hints at the robustness of RDT in predicting normal Reynolds stress evolution in the core of pipe when strained as also recognized analytically by Hunt [31]. Further, to gain more insight into the mutual transfer of energy within the components of turbulent, Reynolds stress anisotropy is plotted in figure 5.24. Here, due to the missing third component of normal Reynolds stress ($\overline{w'^2}$), surrogate of stress anisotropy tensor (b_{ij}^s) is defined conveniently as per the equation 2.9. The proximity of b_{11}^s to zero indicates isotropy in the Reynolds stress. The

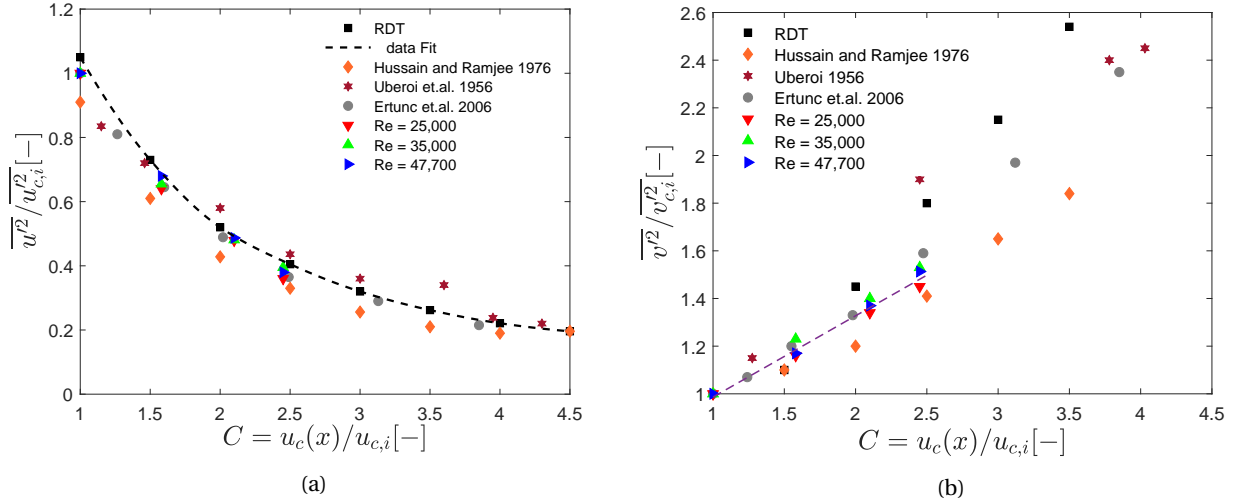


Figure 5.23: (a) Streamwise Reynolds stress evolution inside the contraction at different Re (25,000, 35,000, 47,700) compared with Batchelor and Proudman [4], Uberoi [13], Hussain et al. [6], Ertunc et al. [14]. (b) Transverse Reynolds stress evolution inside the contraction at different Re (25,000, 35,000, 47,700) compared with Batchelor and Proudman [4], Uberoi [13], Hussain [6], Ertunc et al. [14].

trend of b_{11}^s is qualitatively consistent with the predictions of RDT but is slightly higher than RDT prediction due to the reasons specified earlier. The anisotropy changes sign from a positive value of ~ 0.1 in fully developed pipe flow to a negative value of ~ -0.3 as also reported by Chen et al. [24] in the water tunnel grid turbulence. This indicates that the anisotropy of Reynolds stress and turbulence increases appreciably inside the contraction. It is interesting to realise that milder contraction can push turbulence towards equipartition of TKE.

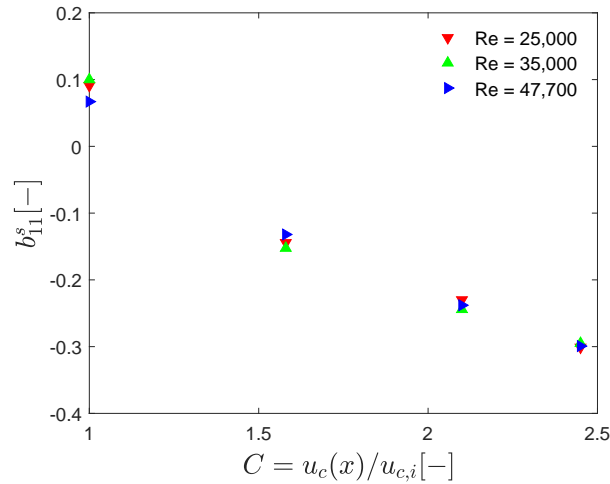


Figure 5.24: Surrogate Reynolds stress anisotropy tensor (b_{11}^s) as a function of local contraction ratio for $Re = 25,000, 35,000, 47,700$.

It was emphasized in section 2.2 that large scales of turbulence are energetic. Hence, to study the effect of strain on the large scales of turbulence, the profiles of TKE are plotted in figure 5.25. For the lack of third component contributing to TKE, it has been defined as $(\overline{u'^2} + \overline{v'^2})$ and normalised by the square of incoming centreline velocity ($u_{c,i}^2$). It can be observed that TKE shows distinct behavior near the axis of contraction and away from the axis. Near the axis, the TKE is fairly constant indicating that the loss of streamwise energy is almost similar to the gain in transverse turbulent energy. This is consistent given the strain is mildly rapid as also reported for smaller contraction ($C \sim 2$) by [8]. For severe contraction as in chapter 4, kinetic

energy increases quite rapidly at the axis of contraction (see figure 4.16b). Away from the pipe axis, it can be seen that TKE shows increase progressively inside the contraction due to the larger increase of $\overline{u'^2}$ and $\overline{v'^2}$. It

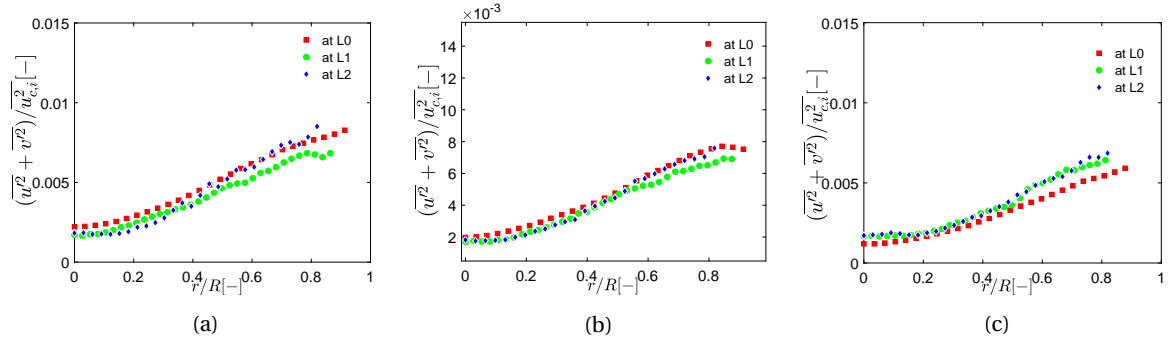


Figure 5.25: The evolution of turbulent kinetic energy inside the contraction at L0, L1, L2 for Re (a) 25,000. (b) 35,000. (c) 47,700.

was also deemed important to evaluate the response of small scales of turbulence to the mean strain. It was established in section 2.2 that the small scales are dominant in enstrophy or vorticity. Hence profiles of rms enstrophy are shown in the figure 5.26. The rms enstrophy profile in a fully developed pipe is consistent with Moin et al. [89] (figure 14). Further, it is observed that the enstrophy increases inside the contraction, however, there is no appreciable difference inside the contraction between the profiles at L1 and L2. The Reynolds shear stress inside the contraction, in the core region remains unchanged or shows a slight increase. However, shear stress in near-wall regions shows an increase further inside the contraction as shown by figure 5.27.

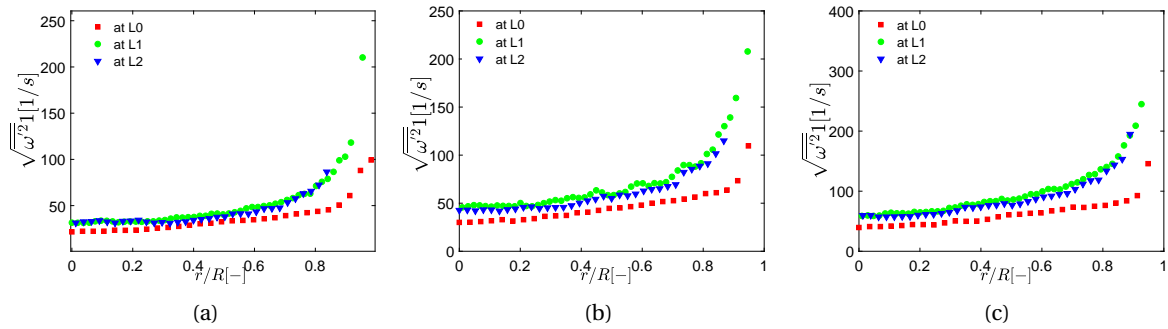


Figure 5.26: The evolution of rms enstrophy inside the contraction at L0, L1, L2 for Re (a) 25,000. (b) 35,000. (c) 47,700.

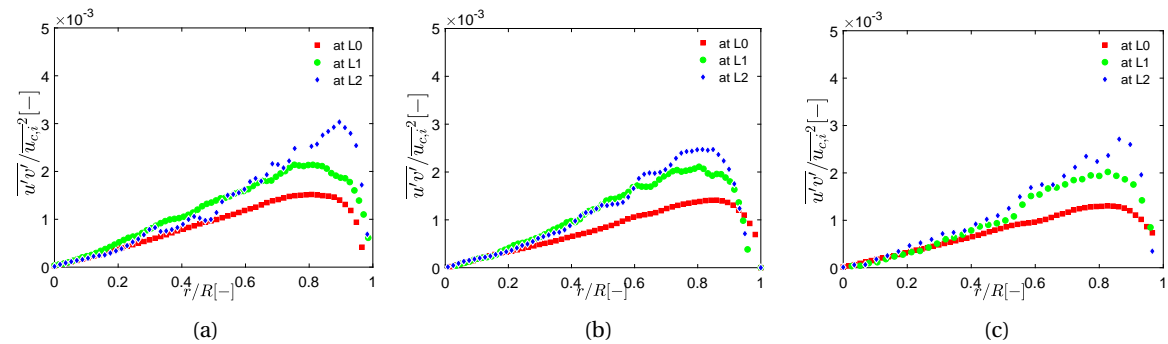


Figure 5.27: The evolution of Reynolds shear stress inside the contraction at L0, L1, L2 for Re (a) 25,000. (b) 35,000. (c) 47,700.

5.3.3. The effect of strain on turbulent structures

The effect of strain on the turbulent structures is qualitatively and quantitatively studied using statistical two-point correlations on the measured velocity data. Such correlations provide information on the shape, size and orientation of averaged turbulent structures (Wallace [90]). Two-point correlation coefficient (R_{uu} , R_{vv}) on the fluctuating velocity components is a measure of large scales of turbulence. Hence, it can be used to study the evolution of large scale structures due to the mean strain. It is defined as given by equation 5.12, where u' and v' are streamwise and transverse velocity fluctuations respectively, (x_0, y_0) correspond to the reference point w.r.t. which correlation is computed. The x-coordinate of the reference point is assigned a local zero for ease of interpretation while y-coordinate is defined zero along the axis of the pipe. Further, the axes have been normalised by pipe diameter (D) to facilitate direct visual comparison of turbulent structures. Note that the flow direction is from left to the right unless specified.

$$R_{uu}(\Delta x, \Delta y) = \frac{\overline{u'(x_0 + \Delta x, y_0 + \Delta y)u'(x_0, y_0)}}{\sqrt{\overline{u'^2(x_0 + \Delta x, y_0 + \Delta y)}}\sqrt{\overline{u'^2(x_0, y_0)}}} ; R_{vv}(\Delta x, \Delta y) = \frac{\overline{v'(x_0 + \Delta x, y_0 + \Delta y)v'(x_0, y_0)}}{\sqrt{\overline{v'^2(x_0 + \Delta x, y_0 + \Delta y)}}\sqrt{\overline{v'^2(x_0, y_0)}}} \quad (5.12)$$

As can be seen in figure 5.28a, 5.29a, inside the contraction, turbulent structures at the axis are not affected

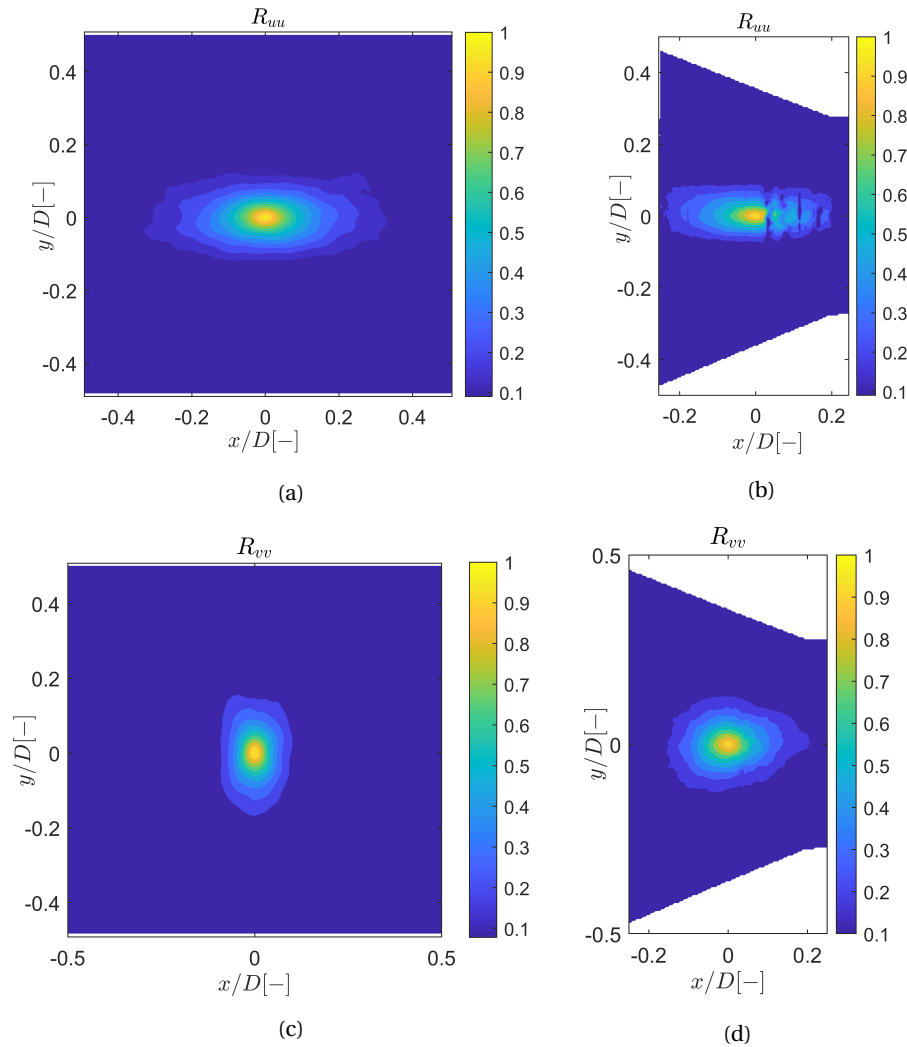


Figure 5.28: Sample two-point correlation coefficient at $Re = 35,000$ (a) R_{uu} in the pre-contraction straight section. (b) R_{uu} inside the contraction (the artefacts in correlation is due to the optical anomaly; see appendix D). (c) R_{vv} in the pre-contraction straight section. (d) R_{vv} inside the contraction. The flow is from left to right.

appreciably along the streamwise directions, rather it appears faintly small in the streamwise direction at

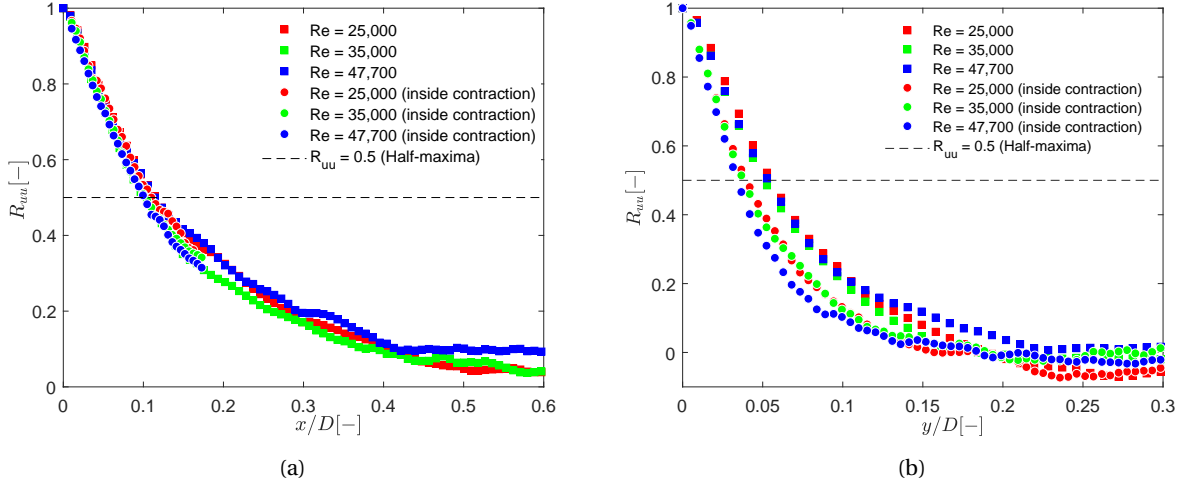


Figure 5.29: R_{uu} at the axis of the pipe and contraction (a) along streamwise direction, (b) along the radial direction at $Re = 25,000$, 35,000, 47,700

the highest Re . This is consistent with the earlier observations made in TKE profiles (see figure 5.25) which remained fairly constant inside the contraction along the axis of the contraction. However, in the radial direction, they appear to have compressed. This is clearly observed in figure 5.28b, 5.29b along the half-maxima line to the normalised correlation function. Further, the correlation is integrated along the radial direction to get the estimate of the length scale of structures as per equation 2.12. It is intended to see if there is any correlation of the extent of compression experienced by large scales w.r.t. local contraction ratio (C). The ratio of this length scales (c_s) is defined by equation 5.13.

$$c_s = \frac{\int_0^\infty R_{uu} dy \Big|_{pre-contraction}}{\int_0^\infty R_{uu} dy \Big|_{contraction}} \quad (5.13)$$

It is seen that the radial extent of large scales decrease by a factor of 1.40 for $Re = 25,000$, 1.36 for $Re = 35,000$

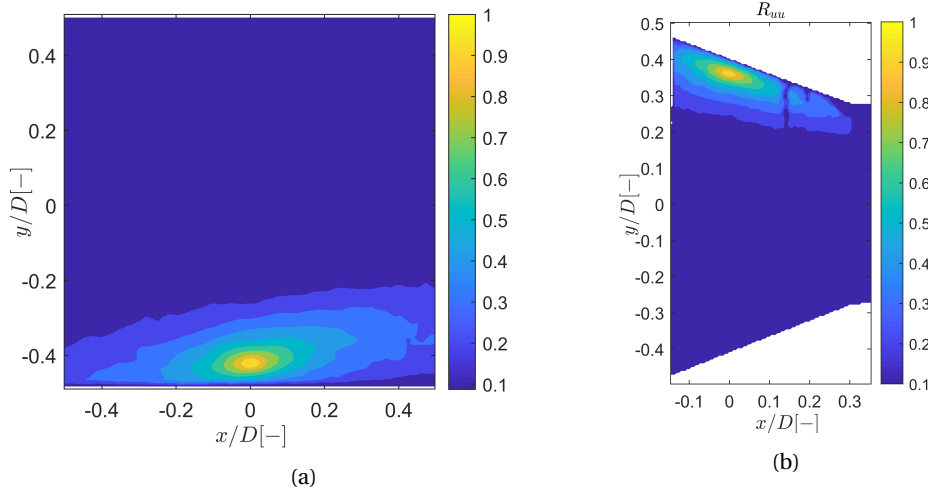


Figure 5.30: Sample two-point correlation R_{uu} at $r/R = 0.82$ at $Re=35,000$; (a) In the straight pre-contraction straight section. (b) Inside the contraction; Note: The flow is from left to right; the vertical strips in the (b) is the result of optical artefacts, see appendix D.

and 1.5 for $Re = 47,000$ case, where local contraction ratio is ~ 1.38 . Thus, c_s is very close to the local contraction ratio and increases slightly with Re , suggesting a possible effect of Re on the experienced strain on large scales of turbulence, i.e., at the highest Re , compression experienced by large scales is maximum. On

the other hand, figure 5.28c and 5.28d shows that R_{vv} at the axis of the contraction has changed significantly in terms of its shape and orientation, i.e., it appears stretched appreciably along the mean flow direction due to the imposed strain.

Close to the wall ($r/R \sim 0.85$), turbulent structure in a fully developed pipe shows a signature of coherent structures inclined at an angle of $\sim 10^\circ$ w.r.t. the straight pipe wall as also observed in boundary layers by Adrian [52], Sillero et.al. [91] and others (see figure 5.30a, 5.31a). Upon straining, the near-wall turbulent

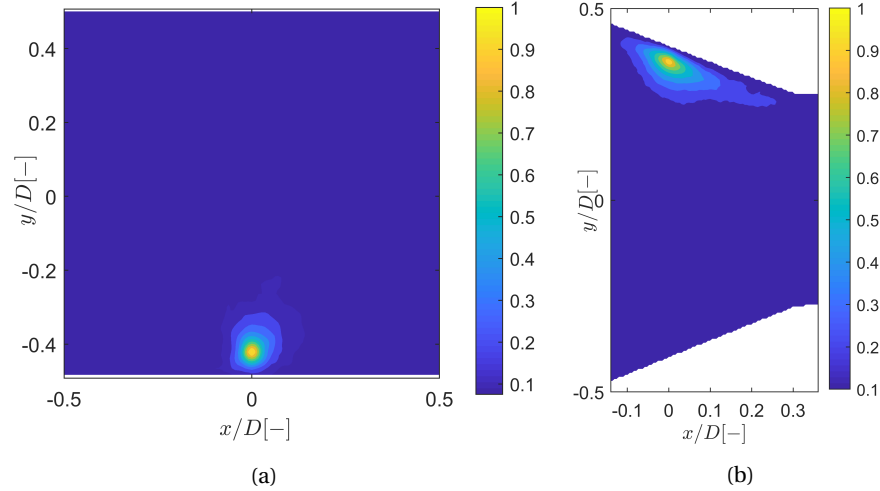


Figure 5.31: Sample two-point correlation R_{vv} at $r/R = 0.82$ at $Re=35,000$; (a) In the straight pre-contraction straight section. (b) Inside the contraction. Note that the flow is from left to right

structures tend to align with the mean flow as the large structures are now inclined at 15° w.r.t. to the horizontal, almost parallel to the walls of contraction. Further, they seem to be more severely affected by the contraction in the radial direction (compressed). It is important to mention however that near the wall, there is a combined effect of shear and strain which can impose added strain on the turbulent structures. The correlations presented in figure 5.28b, 5.30a have vertical stripes of zero correlation due to the optical artefacts mentioned before and in appendix D. Further, R_{vv} also has undergone a severe change in its orientation such that it is now aligned with the mean flow, also it appears stretched in the direction of the mean flow. It is hypothesized that mean strain rate may result in untangling of the braids of hairpin vortex structure resulting in the formation of two-counter rotating eddies as also reported by [8]. See figure 5.32 for articulation. Thus, severe distortion of large turbulent scales upon straining is responsible for the induced anisotropy in turbulence.

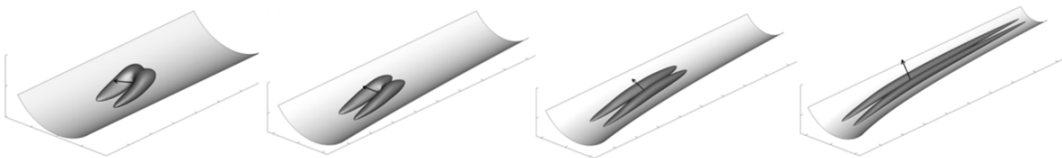


Figure 5.32: Iso-contours of swirling strength realised with DNS, reproduced from [8] (figure 20); left to right: straight section to progressively inside of contraction.

The effect of strain on the small scales of turbulence is ascertained by computing Taylor micro-scales. Taylor micro-scales are computed by fitting a parabola via a least square algorithm to the correlation function (R_{uu}) near the zero separation. The fitted parabola has the form $p_1(x/D)^2 + p_2$, where p_1 and p_2 are the least square fit parameters. Taylor micro-scales which are the measure of small scales are seen to increase in size when strained (inside the contraction) for measured $Re \sim 25,000, 35,000$ as shown in the figure 5.33. This is further qualitatively observed by performing a spatial correlation on the out of plane vorticity (ω) as shown in the equation 5.14. This is justified because the small scales of turbulence are dominant in enstrophy as

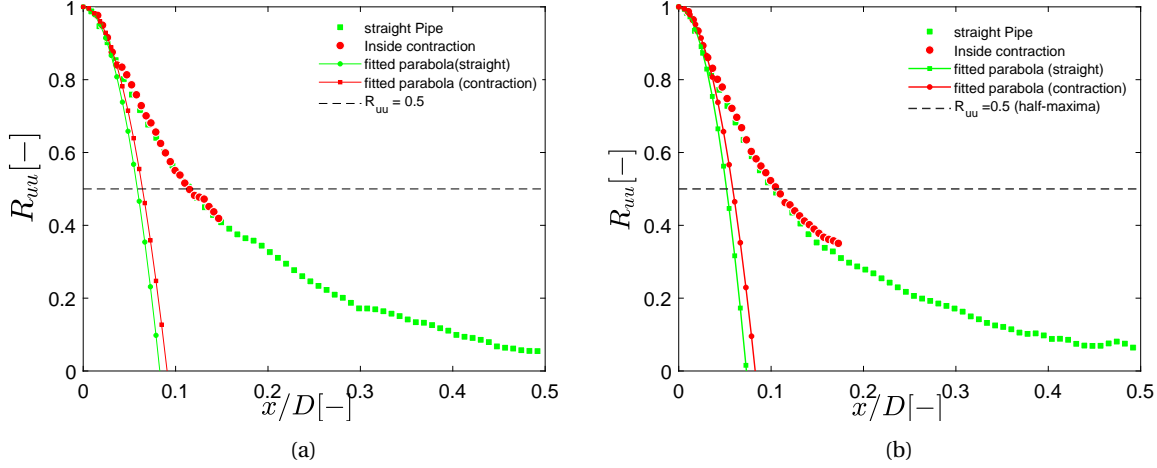


Figure 5.33: Taylor micro-scale comparison in the pre-contraction to inside the contraction for (a) $Re = 25,000$. (b) $Re = 35,000$.

mentioned in section 2.2. The vorticity is computed by computing gradient of the measured velocity field which is calculated using a central difference scheme, followed by a moving mean filter of size (3×3) . The size of the filter is dictated by the 50% overlap employed while computing velocity vector from particle images as each IW contains three data points along each axis. Note that the x-coordinate of the reference point is assigned a local zero for the ease of interpretation while y-coordinate is defined zero along the axis of the pipe.

$$R_{\omega\omega}(\Delta x, \Delta y) = \frac{\overline{\omega'(x_0 + \Delta x, y_0 + \Delta y)\omega'(x_0, y_0)}}{\sqrt{\overline{\omega'^2(x_0 + \Delta x, y_0 + \Delta y)}}\sqrt{\overline{\omega'^2(x_0, y_0)}}} \quad (5.14)$$

It can be seen from the correlation that the small scales are severely affected due to the mean strain. Two effects can be realized viz; shape and orientation of eddies. It seems that the length of correlation increases progressively inside the contraction while it is severely compressed in the radial direction as evident from figure 5.34. Further, the orientation of correlation suggests that the small scales tend to get aligned w.r.t. the mean flow inside the contraction. From the shape of correlation, it can be proposed that the vortical structures assume a form of vortex sheets or layers much like those proposed by Hunt et.al. [33], Elsinga et.al. [92].

Further, these sheets are associated with increased vorticity (enstrophy) under the effect of strain which was also observed in the profiles of enstrophy (see figure 5.26). Here, we define coherence length as the full width of correlation coefficient where it drops to 5% of maximum, i.e., 0.05 on either side of zero. The coherence length of $R_{\omega\omega}$ is estimated to be $\sim \pm 65\eta \sim 130\eta$, where η is as defined by $\eta = DRe^{-3/4}$ and is consistent with Elsinga et.al. [92] in the pre-contraction region of pipe as seen in the figure 5.34d. The coherence length is more than a typical correlation length over which a dissipating vortical structure would span. This is attributed to the spatial organization of the small scale dissipating structures in the form of sheets. Upon straining, these vortex sheets seem to undergo severe stretching in streamwise direction and compression in the radial direction as shown in figure 5.34d. It seems that the small scales suffer more severe deformation as compared to large scale. This can be justified by the higher strain accumulated in the small scales of turbulence.

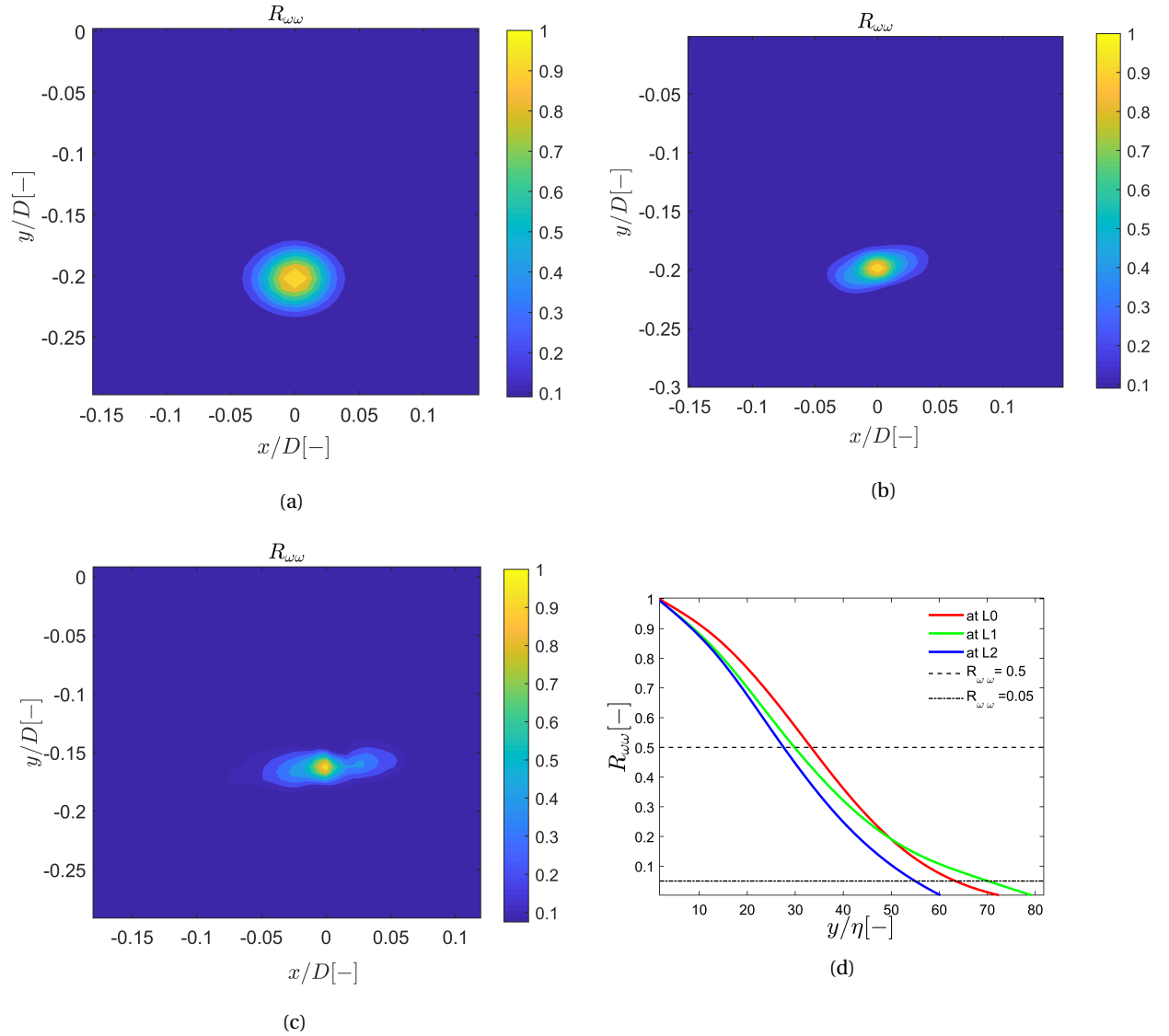


Figure 5.34: Vorticity correlation ($R_{\omega\omega}$) as a function of axial separation at $Re = 35,000$ at various axial locations; (a) Straight pipe (L0). (b) at L1. (c) at L2. (d) The spatial extent of vorticity correlation in terms of Kolmogorov's length scale (η).

5.3.4. Turbulence evolution in post-contraction region

As mentioned before, the flow topology has been divided into pre-contraction, contraction and post-contraction region as shown in figure 5.16. Having analysed strained turbulence inside the contraction, this subsection intends to report observations in the post-contraction region with only a preliminary analysis due to the dearth of time. In-depth analysis is the subject of future work. The profiles of various quantities shown are consistent with the schematic in figure 5.16. Further, the normalisation employed is the same as used in the previous subsection i.e. velocity and turbulent velocity fluctuations are normalised by incoming centreline velocity ($\overline{u_{c,i}}$). Moreover, the radial distance is normalised by local radii (R) at every axial position.

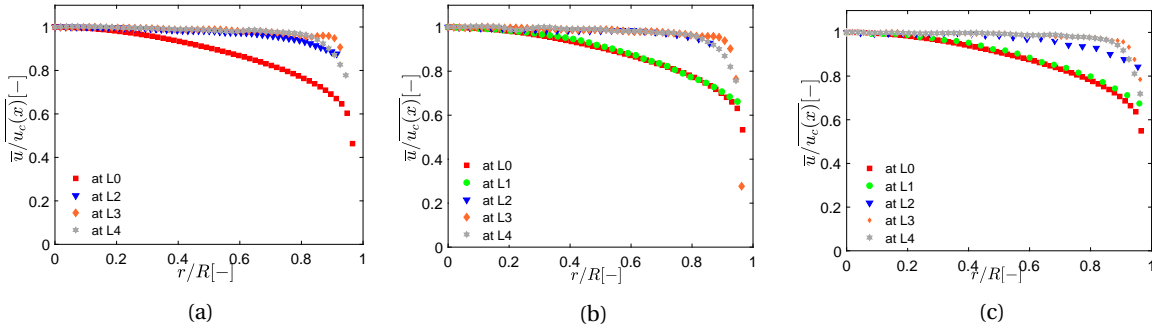


Figure 5.35: Mean axial velocity profile normalised by centreline velocity at different axial positions L0, L1, L2, L3, L4 for Re (a) 25,000 (b) 35,000 (c) 47,700.

It is seen that the mean axial velocity profile gets further flattened in as compared to L2 but has a tendency to relax further downstream at location L4 at all Reynolds number (Re) as shown in figure 5.35. Here, relaxing refers to tenancy towards fully developed pipe flow. Comparing \overline{u} at L4 relative to L3 at disparate Re , it is observed that at low Re , the velocity profile appears less flat. This is because the flow close to the wall will undergo inner-layer growth [93]. The rate of BL growth is higher for low Re as it scales inversely with Re ($d\delta/dt \sim Re^{-1/4}$), where δ is the TBL thickness [94]. In the streamwise velocity fluctuation profiles (figure

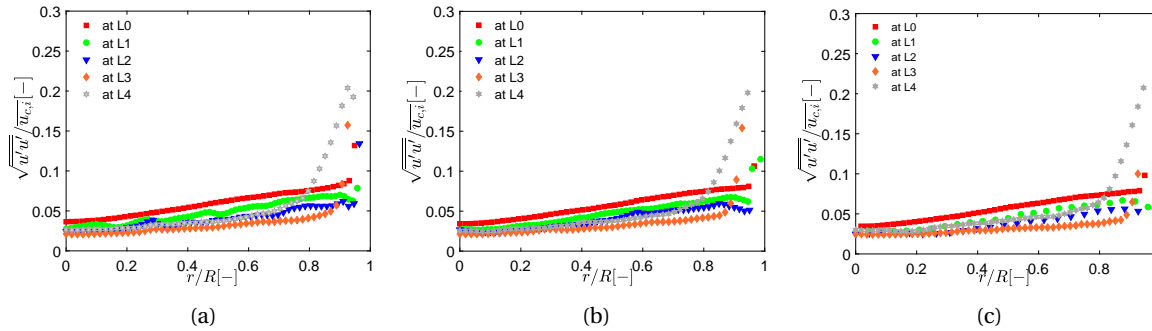


Figure 5.36: Streamwise velocity fluctuations (urms) normalised by incoming centreline velocity at different axial positions i.e. L0, L1, L2, L3, L4 for Re (a) 25,000. (b) 35,000. (c) 47,700.

5.36), it seems that at L3, streamwise fluctuations are lower than inside the contraction (L2) and almost uniform in the radial direction except close to the wall. Further, downstream at L4, there is increase in streamwise velocity fluctuations throughout the span of pipe breaking away from the trend of monotonic decrease from L0 to L3. This is a signature of relaxing turbulence. Moreover, close to the wall, it has a very high peak (almost one order higher magnitude) as also observed by [8, 53] in the downstream part of the venturi in chapter 4 of this report. The author suspects that this is a manifestation of the highly sheared inner-layer redeveloping in the post-contraction region.

The transverse velocity fluctuation shows a monotonic increase in the post-contraction region in the core region of the pipe as seen from figure 5.37. However, near the wall, it decreases at L4 w.r.t. L3. At the axis of the pipe, the mutual exchange of energy from the streamwise to the transverse component of Reynolds

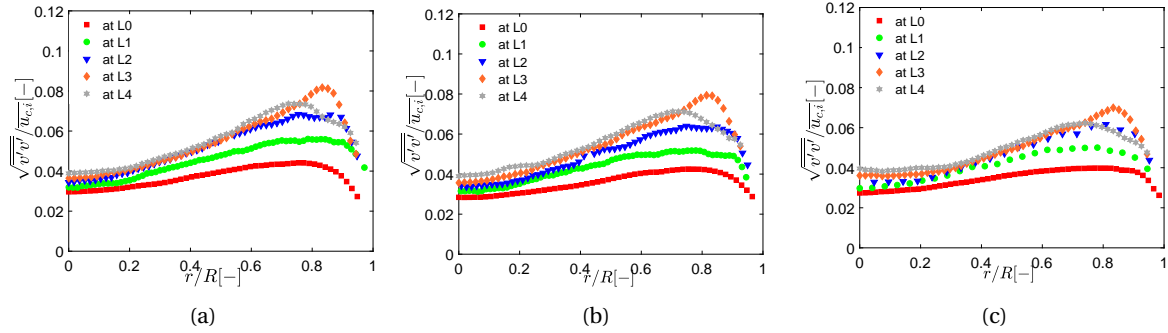


Figure 5.37: Transverse velocity fluctuations (vrms) normalised by incoming centreline velocity at different axial positions L0, L1, L2, L3, L4 for Re (a) 25,000. (b) 35,000. (c) 47,700.

stress continues even in the post-contraction region despite the suspension of straining agency although there is very mild straining. This is made clear in Reynolds's stress anisotropy component (b_{11}^s) at the centre of post-contraction region as shown in the figure 5.38. Although there is an exchange of energy within the components, the magnitude of this exchange is certainly reduced as Reynolds stress anisotropy recovers. The anisotropy induced in Reynolds's stresses inside the contraction is reduced slowly as the flow begins to relax in the post-contraction region. Such slow relaxation of turbulence in post-contraction region has also been observed in wind tunnel experiments with contraction in the past by [5, 34, 41, 50] and more recently by [7, 14, 24]. Further, turbulence at highest Re seems to relax slightly faster than lower Re .

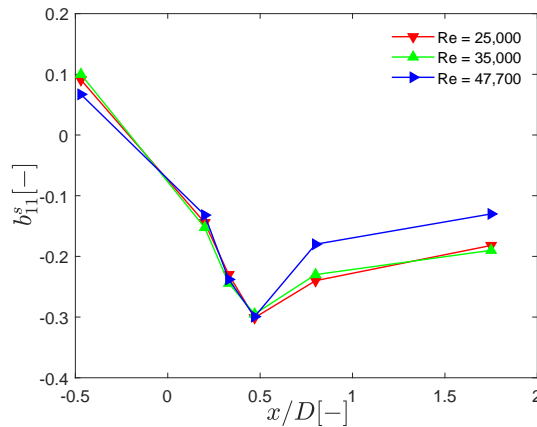


Figure 5.38: Surrogate Reynolds stress anisotropy component (b_{11}^s) along the axial length of contraction.

Reynold's shear stress starts dropping in the core region as compared to the strained profile (L1 and L2) (see figure 5.39). Its evolution is non-intuitive since, at L3, it is very close to the fully developed profile in the core of the pipe but has a peak close to the wall. Further at L4, there is a sudden upsurge in the shear stress throughout the pipe span. This peak is at the same radial position as the peak in vrms (streamwise velocity fluctuation). These observations point to inner-layer redeveloping in this region.

The two-point correlation of velocity fluctuations (R_{uu}) reveal that the averaged large scale turbulent structures has severely shrunk in both the directions, i.e., streamwise and radial, as compared to pre-contraction turbulence. It appears more slender than the structures inside the contraction. Further, it seems that at higher Re the structures are slightly more compressed in radial and elongated in streamwise direction (see figure 5.41). It is likely that at higher Re , large scales of turbulence have adjusted better to new straight pipe section such that $c_s \sim 2.6$ (see equation 5.13 for definition). The shape of R_{vv} suggests that it is significantly bigger than R_{uu} (see figure 5.40) as also reported by [7] although it appears more stretched than inside the contraction. Thus, relaxation in the post-contraction region at the core of the pipe shows Re dependence as also observed in Reynolds stress anisotropy in figure 5.38.

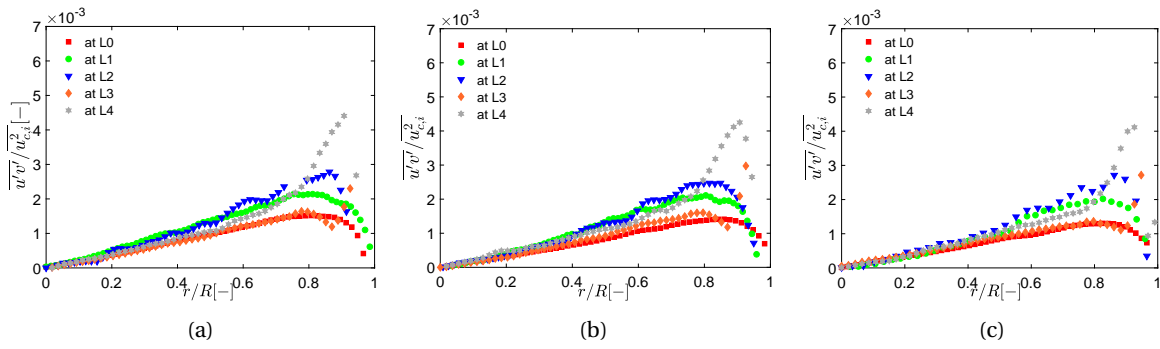


Figure 5.39: Reynolds shear stress normalised by the square of incoming centreline velocity at different axial positions i.e. L0, L1, L2, L3, L4 for (a) $Re=25,000$. (b) $35,000$. (c) $47,700$.

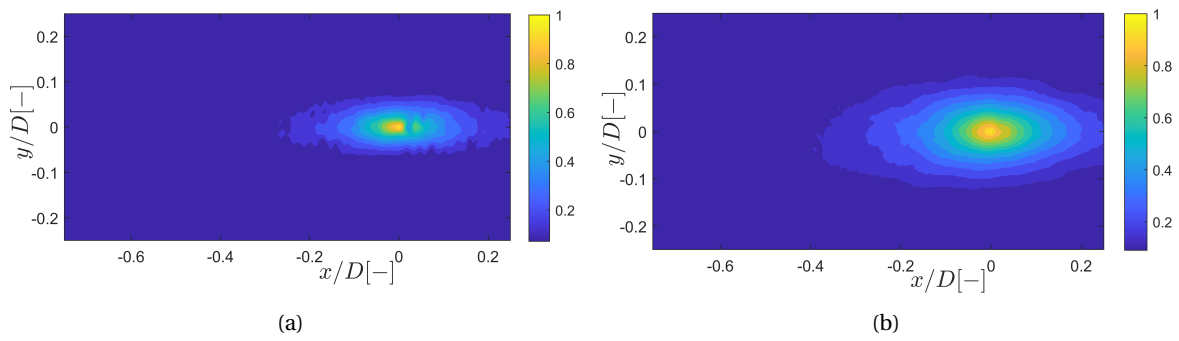


Figure 5.40: Sample two-point correlation at axis of pipe at $Re=35,000$ at axial distance equivalent to L4 (a) R_{uu} . (b) R_{vv} . The flow is from left to right.

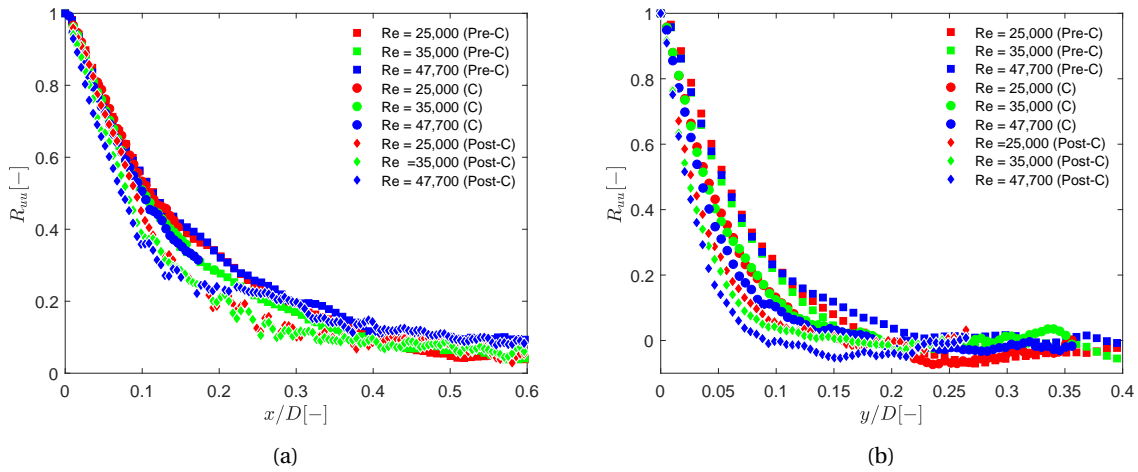


Figure 5.41: R_{uu} at the axis of in pipe in pre-contraction straight section (Pre-C), inside the contraction (C), post-contraction (Post-C); (a) Along streamwise direction. (b) Along the radial direction at $Re = 25,000, 35,000, 47,700$.

6

Conclusions and recommendations

6.1. Conclusion

The main objective of this thesis was to experimentally study the effect of irrotational, axisymmetric strain on fully developed turbulent pipe flow. This was achieved with high-resolution planar Particle Image Velocimetry (PIV) measurements. The effect of strain on large and the small scales of turbulence was studied separately. For this, a mild spatial contraction of $C \sim 3$ was designed, fabricated and assembled downstream of fully turbulent pipe flow. The maximum mean strain rate achieved due to contraction was limited to $s^{*s} \sim 3.2$. The response of turbulence was studied to such mildly rapid strain at three disparate Re (defined on incoming flow) $\sim 25,400$, $35,000$, $47,700$.

The contraction accelerates the mean flow which in turn imposes strain on the turbulence. The effect of strain on the mean flow is to flatten the mean axial velocity profiles due to the added pressure gradient caused by acceleration. The effect of strain on the Reynolds stresses is to suppress turbulence, however, this effect is majorly due to the normalisation with local centreline velocity. The absolute transverse Reynolds stress $\sqrt{v'^2}$ increases at the expense of streamwise Reynolds $\sqrt{u'^2}$ inside the contraction. This mutual exchange of energy within the components is manifested in the anisotropy of Reynolds stress (b_{11}^s) which reverses its sign from ~ 0.1 to ~ -0.3 implying that mean strain induces severe anisotropy in turbulence. It is seen that the evolution of streamwise Reynolds stress, inside the contraction, is well predicted by rapid distortion theory (RDT) while the evolution of transverse Reynolds stress is over-predicted by RDT. Nevertheless, RDT predicts the correct trend of normal Reynolds stresses. The deviation w.r.t. RDT can be attributed to the mild rapidness of the current strain. Further, pipe turbulence being wall-bounded, large scales are confined by blocking effect. Despite strain being only mildly rapid, the closeness of measured data to RDT prediction is noted. It is seen that upon straining, Reynolds shear stress stays practically unaltered close to the axis of pipe while near the wall, increases appreciably.

The response of strain on time-averaged turbulent structures is discerned by computing 2D two-point correlations. It is seen that large scales of turbulence near the axis of pipe are not affected appreciably in the streamwise direction but are severely compressed in radial direction due to the strain. Further, the amount of compression is found to scale with the local contraction ratio. The strain seems to modify transverse correlation (R_{vv}) more than streamwise correlation (R_{uu}). Near-wall coherent structures which were initially inclined with the wall tend to align with the mean flow inside the contraction and become almost parallel to the contraction wall. They were seen to be severely compressed in the radial direction as well. The shape of correlation faintly suggests that mean strain untangles braids of hairpin vortex resulting in two double roller eddy near the wall. Further, this event could be attributed to the increased shear stress in the near-wall region.

The effect of strain on small scales of turbulence is studied by computing Taylor micro-scales and two-point correlation on vorticity ($R_{\omega\omega}$). It is seen that Taylor micro-scales grow slightly inside the contraction as a result of strain. Similarly, $R_{\omega\omega}$ shows that the small scales are spatially organised in the form of sheets which undergo severe deformation inside the contraction. Upon straining, these sheets elongate in streamwise and

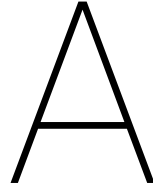
get compressed in the radial direction. Further, these sheets get aligned with the mean flow. It is seen that small scale undergo more severe distortion than large scales of turbulence. However, two-point correlation can only capture averaged structure as instantaneous turbulent structures may reveal further insights. This is left for future work. Furthermore, the effect of Reynolds number (Re) is not realised as s^{*s} is the governing non-dimensional number dictated completely by contraction geometry. Even higher Re than considered here ($> 47,700$) may be required for decoupling of large and small scales of turbulence.

Having studied milder contraction, the response of turbulence to larger contraction ($C \sim 4 - 9$) was experimentally studied in a venturi using planar PIV. The mean flow evolved similar to that of smaller contraction. However, the response of turbulence was quite different. As opposed to an inter-component energy transfer from streamwise transverse component, both the components of normal Reynolds stress were seen to increase at the axis of the contraction. However, downstream of contraction, a delayed transfer of energy was observed much like observed in spatially accelerated wall bounded turbulence. Such distinct response of turbulence to milder and larger contraction was also observed by Hussain and Ramjee [6, 40].

In the post-contraction region, at the axis of pipe, it is seen that mutual exchange of energy (between streamwise and transverse Reynolds stress) continues but the magnitude of exchange has decreased as Reynolds stress anisotropy recovers slowly. Thus, strained turbulence undergoes slow relaxation. At higher Re , large scales at the axis of the pipe are compressed more suggesting Re dependence in the relaxing turbulent flow. However, a detailed analysis could not be carried out due to the limited time scale of a master thesis. Near the wall, relaxation is via a Re dependent inner layer development such that it is faster at lower Re . Further downstream of contraction, there is a sudden upsurge of normal and shear stresses close to the wall suggesting that the highly sheared inner layer is trying to re-develop.

6.2. Recommendation for future work

- It is highly recommended to re-manufacture a test section or polish the existing contraction to avoid optical artefacts mentioned in the appendix D.
- A budget analysis of Reynolds stresses can be performed to see the effect of rapid strain on each term in the governing equation using 3D PIV measurements. However, to perform calibration for a contracting geometry employed in this research is a practical challenge.
- Time resolved measurements can be performed to study the instantaneous turbulent structures during straining and relaxation.
- Turbulent scale interaction and vortex dynamics in post-contraction relaxation can be studied in detail in a longer post-contraction straight pipe than employed in this thesis.
- The turbulence evolution close to the wall is distinct as compared to the core region. Efforts can be made to resolve near-wall turbulence well to observe this.
- Data recorded in the current thesis can be analysed further to investigate the cause of higher distortion experienced by small scales of turbulence inside the contraction.



Appendix 1: Optical anomaly - 1

In order to make sense out of pixel displacements data from PIV, it is required to perform calibration for the measurements. The calibration is performed for three purposes: (i) To focus the camera on the measurement plane (area of interest). (ii) To convert from image scale to real world scale. (iii) Correct optical distortion produced by material of test section and curvature of venturi.

A grid is made of certain number of symbols such as pluses ('+') as shown in the figure with known physical dimensions of plus and separation between them. This thin grid is inserted exactly in the plane where measurements are desired. For (i), LED panel is used as illumination source. The aperture and exposure time of camera is varied to get the best contrast between '+'s and background. The camera is then focused on these '+'s such that very sharp image is obtained. While doing this, live image is continuously streamed from camera on DaVis software is zoomed to see the contrast at pixel scale. Ultimately, multiple images are captured and averaged over to be used for calibration purpose.

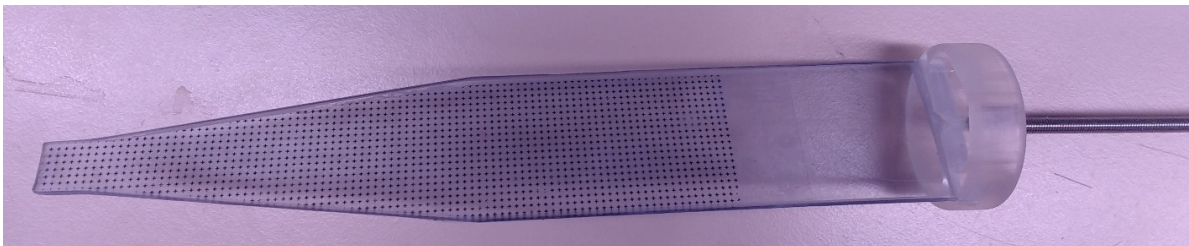


Figure A.1: Calibration Target with grid spacing 2mm and 2mm '+'

For (ii), the images are processed in DaVis where it tries to find plus marks and then fits the grid corresponding to the given physical dimensions of the grid as shown in the figure. For the fitting purpose, linear polynomial should ideally do the job but for higher accuracy, third order polynomial is used which is a standard practice in PIV. Once the grids are fitted, number of pixels are counted between '+'s and related to known physical dimension. Hence, calibration outputs magnification in pixels/mm. Mapping of raw coordinates system to world coordinate system is shown in Appendix C.

If you look closely in the above figure A.2, there is a significant mismatch between target and third order fitted grids in the convergent part of the venturi. This is deemed due to the angles of convergent and divergent part refracting light differently in two parts. This is made clear with ray tracing diagram (figure A.3) where we clearly see rays bending away from each other at the neck of venturi. This is clearly visualized in calibration images since the distance between '+'s increase. This warranted separate calibration of convergent and divergent parts of venturi and stitching them later. After correction, final calibrations looks like as shown in the figure A.4.

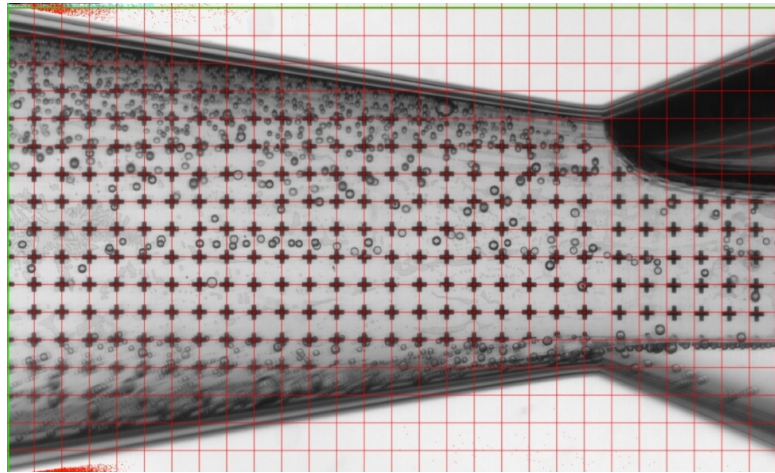


Figure A.2: Calibration grid generated with 3rd order polynomial fitting

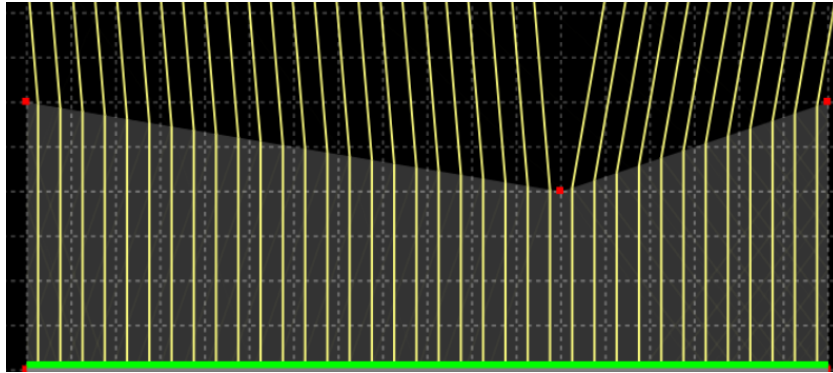


Figure A.3: Qualitative ray tracing diagram for current test setup. source: Ray Optics Simulation

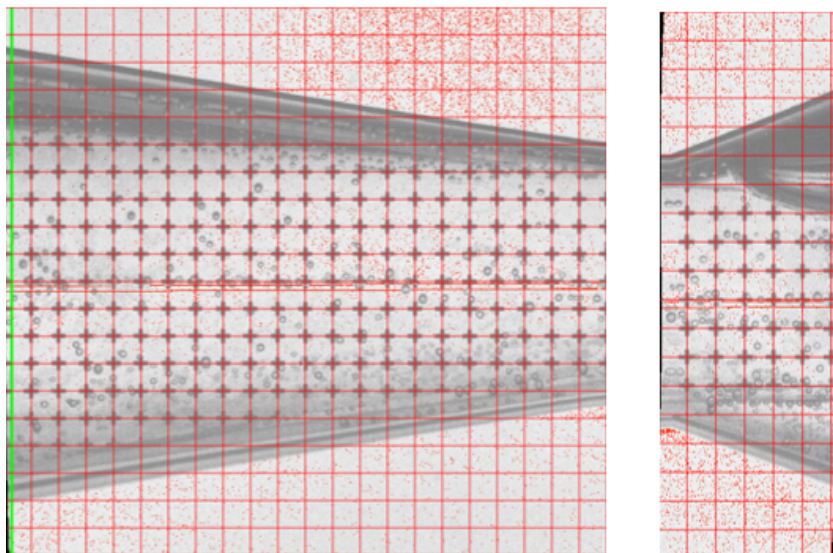


Figure A.4: Final corrected calibration in two different sections

B

Appendix 2: Optical anomaly - 2

It was seen during imaging of low particle density flow that there were streaks of particles especially in the lower part of venturi as shown in the figure B.1. They were not physical and insensitive to camera settings. A closer look at these streaks show that particles at certain locations are imaged with interference pattern. These patterns have peak intensity at the center and gradual reduction away from the centre (as highlighted in figure B.1). The peak intensity is the actual particle image while less intense trails are optical artefacts.

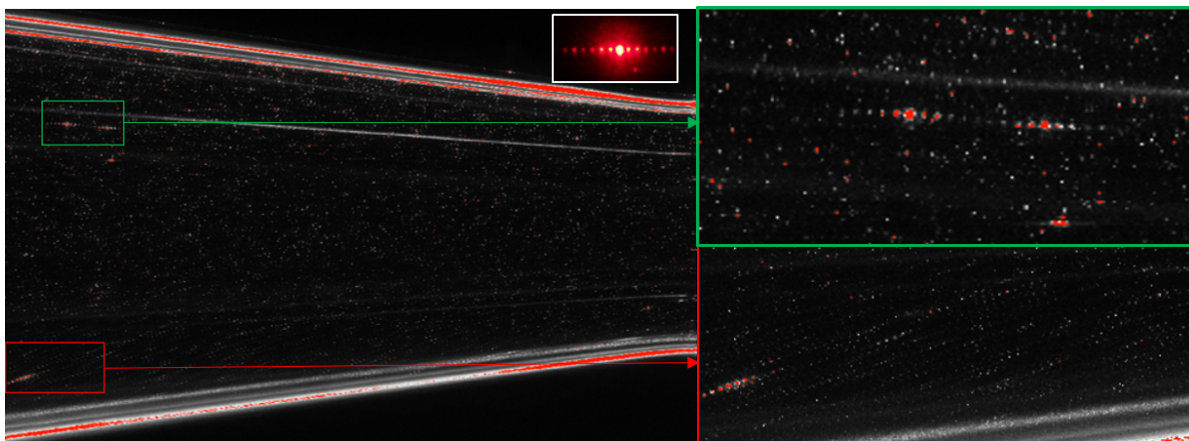


Figure B.1: Particle images with streaks caused by diffraction. The interference pattern shown in white box was reported in [15]

It was suspected that this optical distortion is due to birefringence produced due to anisotropy in Plexi Glass (PMMA) test section. However, it was found that the streaks were local and were probably caused due to the grating present on the test section. The gratings typically are very small slits which are resultant of imperfect surface finish during milling operation. The laser light get bend around these small slits and due to wave nature of light interference pattern is formed as shown in the figure B.2. Such optical artefacts are undesirable, hence it is recommended to polish the inner and outer walls of PMMA test section when it is to be illuminated with coherent light source like laser sheet in PIV.

The Intensity plot is shown for particle image in the inset in figure B.3. Unnecessary pixels have been masked. It can clearly be seen from intensity plot that streaks have intensity distribution like Fraunhofer diffraction pattern (shown in red box). On the other hand, single particle is imaged as a sharp peaks (shown in green box). To observe this clearly, the intensity is plotted along the profiles as shown in the inset of figure B.4 (yellow line). It appears that intensity distribution is indeed like Fraunhofer diffraction pattern in the streaks however, single particles appears as sharp peaks as expected.

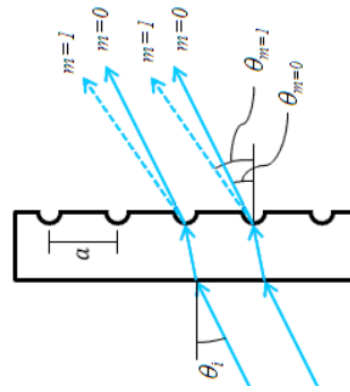


Figure B.2: The diffraction due to gratings (courtesy:Thorlabs Inc.)

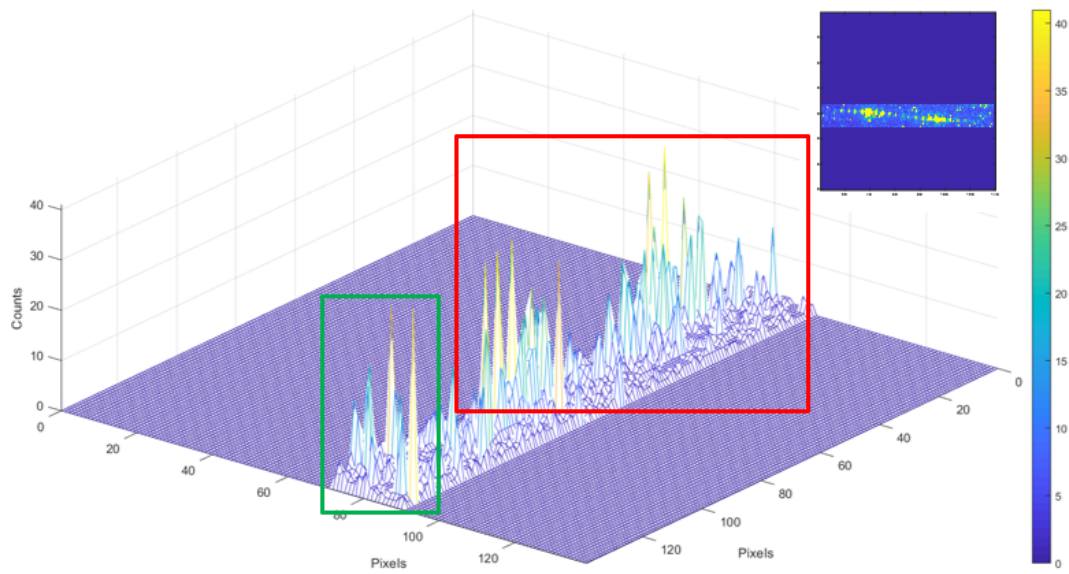


Figure B.3: Surface plot of intensity for particle image as shown in the inset (with thresholding).

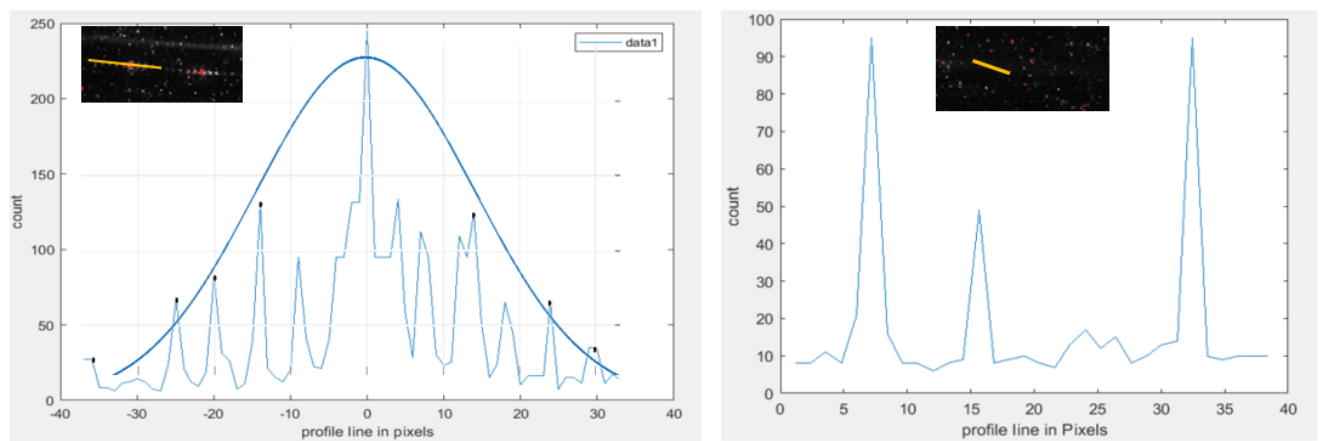
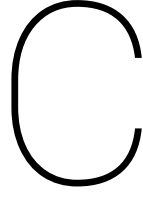


Figure B.4: Left: Intensity plot along a yellow profile line with fitted Gaussian function for a imaged particles streak. Right: Intensity plot along a yellow profile line for un-diffracted particle image



Appendix 3: Calibration

Mapping of raw coordinate system to world coordinate system is done using following steps.

Let $X(x,y)$ be raw coordinate of image and $X' (x',y')$ be the coordinates of world coordinate. Raw coordinates to converted to world coordinates using following transformations.

$$x = x' - dx(s(x'), t(y')) \quad (C.1)$$

$$y = y' - dy(s(x'), t(y')) \quad (C.2)$$

$$s(x') = M_x x' + N_x \quad (C.3)$$

$$t(y') = M_y y' + N_y \quad (C.4)$$

where $s(x')$ and $t(y')$ are linear functions in x' and y' respectively. dx and dy are expressed as third order polynomial in s and t such that

$$dx(s, t) = A_x + B_x s + C_x s^2 + D_x s^3 + E_x t + F_x t^2 + G_x t^3 + H_x s t + I_x s^2 t + J_x s t^2 \quad (C.5)$$

$$dy(s, t) = A_y + B_y s + C_y s^2 + D_y s^3 + E_y t + F_y t^2 + G_y t^3 + H_y s t + I_y s^2 t + J_y s t^2 \quad (C.6)$$

Grids are fitted and above fitting parameters (A_i, B_i, \dots, K_i) are obtained. Such non-linear fit takes into consideration effects of optical distortion like lens aberration and refraction especially at the wall of optical test section.



Appendix 4: Optical anomaly-3

The optical artefacts due to the gratings and machining tool marks on the inner wall of the contraction has resulted in severe loss of cross-correlation, leading to bias in velocity values. The corrupted cross-correlation is shown in the figure D.1 for all the FOVs measured in this report; red corresponds to high and blue is low cross-correlation constant. The pre-contraction is mildly affected with vertical stripes, however, this low correlation does not appear in the velocity values. The contraction has and post-contraction regions have severely affected region, where the low-correlation results in biased velocity values. Amidst this, notice regions of high correlation in post-contraction region.

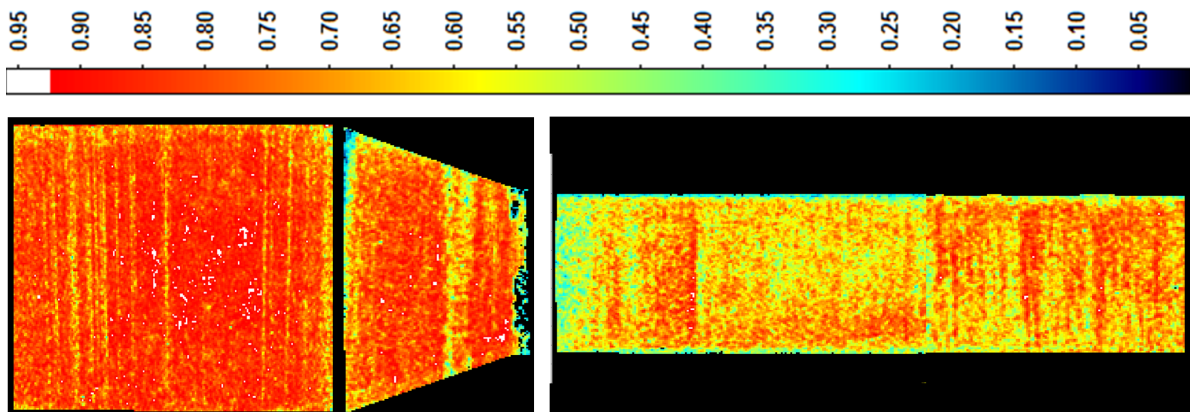


Figure D.1: Cross-correlation coefficient over IW of particle images throughout the measured FOV.

Such artefacts were also noticed on the outer walls of the test section. However, they were removed by in-house polishing using Acrylic polish.

References

- [1] John Leask Lumley Tennekes Hendrik. *A first course in turbulence*. MIT press, 1972.
- [2] Frans T M Nieuwstadt, Bendiks J Boersma, and Jerry Westerweel. *Turbulence Introduction to Theory and Applications of Turbulent Flows*. Springer, 2015. ISBN 9783319315973.
- [3] L. Prandtl. Attaining a Steady Air Stream in Wind Tunnel. Technical Report 8, National Advisory committee for Aeronautics, 1933.
- [4] G. K. Batchelor and Ian Proudman. The effect of rapid distortion of a fluid in turbulent motion. *Quarterly Journal of Mechanics and Applied Mathematics*, 7(1):83–103, 1954. ISSN 00335614. doi: 10.1093/qjmam/7.1.83.
- [5] Mahinder S Uberoi. Effect of Wind-Tunnel Contraction on Free-Stream Turbulence. *Journal of the Aeronautical Sciences*, 23(8):754–764, 1956. ISSN 1936-9956. doi: 10.2514/8.3651. URL <http://arc.aiaa.org/doi/10.2514/8.3651>.
- [6] A. K. M. F. Hussain and V. Ramjee. Effects of the Axisymmetric Contraction Shape on Incompressible Turbulent Flow. *Journal of Fluids Engineering*, 98(1):58, 1976. ISSN 00982202. doi: 10.1115/1.3448210.
- [7] S. Ayyalasomayajula and Z. Warhaft. *Nonlinear interactions in strained axisymmetric high-Reynolds-number turbulence*, volume 566. 2006. ISBN 0022112006. doi: 10.1017/S0022112006002199.
- [8] Seong Jae Jang, Hyung Jin Sung, and Per Åge Krogstad. Effects of an axisymmetric contraction on a turbulent pipe flow. *Journal of Fluid Mechanics*, 687:376–403, 2011. ISSN 00221120. doi: 10.1017/jfm.2011.361.
- [9] R. Narasimha and K. R. Sreenivasan. Relaminarization in highly accelerated turbulent boundary layers. *Journal of Fluid Mechanics*, 61(3):417–447, 1973. ISSN 14697645. doi: 10.1017/S0022112073000790.
- [10] S He and M Seddighi. Transition of transient channel flow after a change in Reynolds number. *Journal of Fluid Mechanics*, 764:395–427, 2015. doi: 10.1017/jfm.2014.698.
- [11] Christian Poelma Saad Jahangir, Willian Hogendoorn. Dynamics of Partial Cavitation in an Axisymmetric Converging and Diverging. *International Journal of Multiphase Flows*, pages 1–9, 2019. doi: .1037//0033-2909.I26.1.78.
- [12] J G M Eggels, F Unger, M H Weiss, J Westerweel, R J Adrian, R Friedrich, and F T M Nieuwstadt. Fully developed turbulent pipe flow: a comparison between DNS and experiment. *J. Fluid Mech.*, 268:175–209, 1994.
- [13] Mahinder S. Uberoi. Equipartition of energy and local isotropy in turbulent flows. *Journal of Applied Physics*, 28(10):1165–1170, 1957. ISSN 00218979. doi: 10.1063/1.1722600.
- [14] Ö Ertunç. *Experimental and Numerical Investigations of Axisymmetric Turbulence*. PhD thesis, Technischen Fakultät der Universität Erlangen-Nürnberg, 2006.
- [15] H. Zapata, F. Fernandez, and A. L. Rivera. Moire patterns in red. Technical Report September, 2013.
- [16] Saravanamuttoo, Herbert IH, Gordon Frederick Crichton Rogers and Henry Cohen. *Gas turbine theory*. Pearson Education, 2001.
- [17] Ovid Baker. Design of Pipelines for the Simultaneous Flow of Oil and Gas. Technical report, Magnolia Petroleum Co. Dallas, Texas, 2007.
- [18] Stephen B. Pope. *Turbulent flows*. Cambridge university press, 2000.

- [19] Zellman Warhaft. Why we need experiments at high Reynolds numbers. *Fluid Dynamics Research*, 41(2), 2009. ISSN 01695983. doi: 10.1088/0169-5983/41/2/021401.
- [20] Adrian, Ronald J. and Jerry Westerweel. *Particle image velocimetry*. Cambridge University Press, 2011., no. 30. edition, 2011.
- [21] J. Westerweel. *Digital Particle Image Velocimetry: Theory and Application*. PhD thesis, TU Delft, 1993.
- [22] Jerry Westerweel, Gerrit E. Elsinga, and Ronald J. Adrian. Particle Image Velocimetry for Complex and Turbulent Flows. *Annual Review of Fluid Mechanics*, 45(1):409–436, 2011. ISSN 0066-4189. doi: 10.1146/annurev-fluid-120710-101204.
- [23] G. E. Elsinga. *Tomographic particle image velocimetry and its application to turbulent boundary layers*, volume 41. 2008. ISBN 9789090231587. doi: 10.1007/s00348-006-0212-z. URL <http://link.springer.com/10.1007/s00348-006-0212-z>.
- [24] Jun Chen, Charles Meneveau, and Joseph Katz. Scale interactions of turbulence subjected to a straining-relaxation-destraining cycle. *Journal of Fluid Mechanics*, 562:123–150, 2006. ISSN 00221120. doi: 10.1017/S0022112006000905.
- [25] G. Newman and John L. Lumley. The return to isotropy of homogeneous turbulence. *Journal of Fluid Mechanics*, 436:59–84, 1976. ISSN 00221120. doi: 10.1017/S002211200100386X.
- [26] G. E. Elsinga and I. Marusic. Universal aspects of small-scale motions in turbulence. *Journal of Fluid Mechanics*, 662:514–539, 2010. ISSN 00221120. doi: 10.1017/S0022112010003381.
- [27] Moon Joo Lee. Distortion of homogeneous turbulence by axisymmetric strain and dilatation. *Physics of Fluids A*, 1(9):1541–1557, 1989. ISSN 08998213. doi: 10.1063/1.857331.
- [28] D. Fiskaletti, J. Westerweel, and G. E. Elsinga. Long-range μ PIV to resolve the small scales in a jet at high Reynolds number. *Experiments in Fluids*, 55(9):1–15, 2014. ISSN 07234864. doi: 10.1007/s00348-014-1812-7.
- [29] G. I. Taylor. Turbulence in a contracting stream. *Journal of Applied Mathematics and Mechanics*, 15(1-2): 91–96, 1935. ISSN 15214001. doi: 10.1002/zamm.19350150119.
- [30] H. S. Ribner and M. Tucker. Spectrum of Turbulence in Contracting stream. Technical report, 1952.
- [31] J. C. R. Hunt and N. K.-R. Kevlahan. Rapid Distortion Theory and the structure of turbulence. *New Approaches and Concepts in Turbulence*, 212:285–305, 1993. ISSN 3764329246. doi: 10.1007/978-3-0348-8585-0.
- [32] Saville A.M. Recent Developments in Rapid Distortion Theory. *Annual Review of Fluid Mechanics*, 19: 325–446, 1987. doi: 10.1007/978-3-662-03770-6_9.
- [33] N. K.R. Kevlahan and J. C.R. Hunt. Nonlinear interactions in turbulence with strong irrotational straining. *Journal of Fluid Mechanics*, 337:333–364, 1997. ISSN 00221120. doi: 10.1017/S0022112097004941.
- [34] A. A. Townsend. The uniform distortion of homogeneous turbulence. *Quarterly Journal of Mechanics and Applied Mathematics*, 7(1):104–127, 1954. ISSN 00335614. doi: 10.1093/qjmam/7.1.104.
- [35] H. J. Tucker and A. J. Reynolds. The distortion of turbulence by irrotational plane strain. *Journal of Fluid Mechanics*, 32(04):657, 1968. ISSN 0022-1120. doi: 10.1017/S0022112068000947.
- [36] Mahinder S. Uberoi and Stanley Wallis. Effect of grid geometry on turbulence decay. *Physics of Fluids*, 10(6):1216–1224, 1967. ISSN 10706631. doi: 10.1063/1.1762265.
- [37] Genevieve Comte Bellot and Stanley Corrsin. The use of a contraction to improve the isotropy of grid-generated turbulence. *Jornal of fluid Mechanics*, 25(1966), 1965. doi: 10.1017/S0022112066000338.
- [38] J. C.R. Hunt. A theory of turbulent flow round two-dimensional bluff bodies. *Journal of Fluid Mechanics*, 61(4):625–706, 1973. ISSN 14697645. doi: 10.1017/S0022112073000893.

- [39] By M E Goldstein. The effect of finite turbulence spatial scale on the amplification of turbulence by a contracting stream. *Journal of Fluid Mechanics*, 98(3):473–608, 1980.
- [40] V. Ramjee and A. K. M. F. Hussain. Influence of the Axisymmetric Contraction Ratio on Free-Stream Turbulence. *Journal of Fluids Engineering*, 98(3):506, 1976. ISSN 00982202. doi: 10.1115/1.3448386.
- [41] Jimmy Tan-atichat. Effects Of Axisymmetric Contractions On Turbulence Of Various Scales. Technical report, National Aeronautics and Space Administration, Chicago, Illinois, 1980.
- [42] Özgür Ertunç and Franz Durst. On the high contraction ratio anomaly of axisymmetric contraction of grid-generated turbulence. *Physics of Fluids*, 20(2), 2008. ISSN 10706631. doi: 10.1063/1.2837173.
- [43] Shunichi Tsugé. Effects of flow contraction on evolution of turbulence. *Physics of Fluids*, 27(8):1948–1956, 1984. ISSN 10706631. doi: 10.1063/1.864876.
- [44] Lennart S Hultgren and Shucheng Chen. Rapid distortion of small-scale turbulence by an axisymmetric contraction. *Physics of Fluids*, 409(26):409–415, 1983. doi: 10.1063/1.864152.
- [45] Christopher J. Zusi and J. Blair Perot. Simulation and modeling of turbulence subjected to a period of uniform plane strain. *Physics of Fluids*, 25(11), 2013. ISSN 10706631. doi: 10.1063/1.4821450.
- [46] Christopher J. Zusi and J. Blair Perot. Simulation and modeling of turbulence subjected to a period of axisymmetric contraction or expansion. *Physics of Fluids*, 26(11), 2014. ISSN 10897666. doi: 10.1063/1.4901188.
- [47] J.C.R. Hunt S.Kida. Interaction between different scales of turbulence over short times. *Journal of Fluid Mechanics*, 201:411–445, 1989. ISSN 14697645. doi: 10.1017/S0022112089000996.
- [48] M. P. Clay and P. K. Yeung. A numerical study of turbulence under temporally evolving axisymmetric contraction and subsequent relaxation. *Journal of Fluid Mechanics*, 805:460–493, 2016. ISSN 14697645. doi: 10.1017/jfm.2016.566.
- [49] D. Naot. Rapid distortion solutions for a stress transport turbulence model in contracting flow. *Physics of Fluids*, 21(5):752–756, 1978. ISSN 10706631. doi: 10.1063/1.862294.
- [50] Robert A. Antonia, P. Lavoie, L. Djenidi, and A. Benaissa. Effect of a small axisymmetric contraction on grid turbulence. *Experiments in Fluids*, 49(1):3–10, 2010. ISSN 07234864. doi: 10.1007/s00348-009-0704-8.
- [51] M. S. Chong, J. Soria, A. E. Perry, J. Chacin, B. J. Cantwell, and Y. Na. Turbulence structures of wall-bounded shear flows found using DNS data. *Journal of Fluid Mechanics*, 357:225–247, 1998. ISSN 00221120. doi: 10.1017/S0022112097008057.
- [52] Ronald J. Adrian. Hairpin vortex organization in wall turbulence. *Physics of Fluids*, 19(4), 2007. ISSN 10706631. doi: 10.1063/1.2717527.
- [53] Arnold F Moene. *Swirling pipe flow with axial strain Experiment and Large Eddy Simulation*. PhD thesis, Technische Universiteit Eindhoven, 2003.
- [54] B. E. Launder. Laminarization of the Turbulent Boundary Layer in a Severe Acceleration. *Journal of Applied Mechanics*, (10):12–13, 1964.
- [55] M. A. Badri Narayanan. An experimental study of reverse transition in two-dimensional channel flow. *J. Fluid Mech.*, 31(3):609–623, 1968.
- [56] V. C. Patel and M. R. Head. Reversion of turbulent to laminar flow. *Journal of Fluid Mechanics*, 34(2): 371–392, 1968. ISSN 14697645. doi: 10.1017/S0022112068001953.
- [57] M. A. Badri Narayanan and V. Ramjee. On the criteria for reverse transition in a two-dimensional boundary layer flow. *Journal of Fluid Mechanics*, 35(2):225–241, 1969. ISSN 14697645. doi: 10.1017/S002211206900108X.

- [58] Ron F. Blackwelder and Leslie S.G. Kovaszny. Large-scale motion of a turbulent boundary layer during relaminarization. *Journal of Fluid Mechanics*, 53(1):61–83, 1972. ISSN 14697645. doi: 10.1017/S0022112072000047.
- [59] Hiroaki Tanaka and Hirotaka Yabuki. Laminarization and Reversion to Turbulence of Low Reynolds Number Flow Through a Converging to Constant Area Duct. *Journal of Fluids Engineering*, 108(3):325, 1986. ISSN 00982202. doi: 10.1115/1.3242581.
- [60] T Oikawa. Fluid Flow and Heat Transfer in a Periodically Diverging-Converging Turbulent Duct Flow. *Chemical Pharmaceutical Bulletin*, 36(43):2091, 1993.
- [61] Ugo Piomelli †, Elias Balaras, and Andrea Pascarelli. Turbulent structures in accelerating boundary layers. *Journal of Turbulence*, 1(December 2014):N1, 2002. ISSN 1468-5248. doi: 10.1088/1468-5248/1/1/001.
- [62] C. Bourassa and F. O. Thomas. An experimental investigation of a highly accelerated turbulent boundary layer. *Journal of Fluid Mechanics*, 634:359–404, 2009. ISSN 00221120. doi: 10.1017/S0022112009007289.
- [63] S. He and J. D. Jackson. A study of turbulence under conditions of transient flow in a pipe. *Journal of Fluid Mechanics*, 408:1–38, 2000. ISSN 00221120. doi: 10.1017/S0022112099007016.
- [64] S.W. Tu and B.R. Ramaprian. Fully developed periodic turbulent pipe flow. Part 1. Main experimental results and comparison with predictions. *Journal of Fluid Mechanics*, 137:31–58, 1983.
- [65] M. Seddighi, S. He, A. E. Vardy, and P. Orlandi. Direct numerical simulation of an accelerating channel flow. *Flow, Turbulence and Combustion*, 92(1-2):473–502, 2014. ISSN 13866184. doi: 10.1007/s10494-013-9519-z.
- [66] David Greenblatt and Edward A. Moss. Rapid temporal acceleration of a turbulent pipe flow. *Journal of Fluid Mechanics*, 514:65–75, 2004. ISSN 00221120. doi: 10.1017/S0022112004000114.
- [67] K. He, M. Seddighi, and S. He. DNS study of a pipe flow following a step increase in flow rate. *International Journal of Heat and Fluid Flow*, 57:130–141, 2016. ISSN 0142727X. doi: 10.1016/j.ijheatfluidflow.2015.09.004.
- [68] Mahinder S. Uberoi and Stanley Wallis. Small axisymmetric contraction of grid turbulence. *Journal of Fluid Mechanics*, 24(3):539–543, 1966. ISSN 14697645. doi: 10.1017/S0022112066000806.
- [69] Matthew P Clay. *Strained Turbulence and Low-Diffusivity Turbulent Mixing Using High Performance Computing*. PhD thesis, Georgia Institute of Technology, 2017.
- [70] R. Narasimha and K. R. Sreenivasan. *Relaminarization in highly accelerated turbulent boundary layers*, volume 61. 1973. ISBN 0022112073000. doi: 10.1017/S0022112073000790.
- [71] Ugo Piomelli and Junlin Yuan. Numerical simulations of spatially developing, accelerating boundary layers. *Physics of Fluids*, 25(10), 2013. ISSN 10706631. doi: 10.1063/1.4825033.
- [72] S. He and M. Seddighi. Turbulence in transient channel flow. *Journal of Fluid Mechanics*, 715:60–102, 2013. ISSN 00221120. doi: 10.1017/jfm.2012.498.
- [73] J. M.J. Den Toonder and F. T.M. Nieuwstadt. Reynolds number effects in a turbulent pipe flow for low to moderate Re. *Physics of Fluids*, 9(11):3398–3409, 1997. ISSN 10706631. doi: 10.1063/1.869451.
- [74] Casimir Willem Hendrik Van Doorne. *Stereoscopic PIV on transition in pipe flow*. PhD thesis, TU Delft, 2004.
- [75] Hermann Schlichting. *Boundary Layer Theory*. McGraw-Hill, 7th edition, 1979.
- [76] Amitosh Dash, Saad Jahangir, and Christian Poelma. Direct comparison of shadowgraphy and x-ray imaging for void fraction determination. *Measurement Science and Technology*, 29(12), 2018. ISSN 13616501. doi: 10.1088/1361-6501/aaea49.

- [77] Martin Bruschi, Kristine John, Saad Jahangir, Udhav Gawandalkar, Willian Hogendoorn, Christian Poelma, Sven Grundmann. *exp_saad.pdf. Experiments in Fluids (under revision)*, 2019.
- [78] Jerry Westerweel and Fulvio Scarano. Universal outlier detection for PIV data. *Experiments in Fluids*, 39(6):1096–1100, 2005. ISSN 07234864. doi: 10.1007/s00348-005-0016-6.
- [79] Zambri Harun. *The structure of adverse and favourable pressure gradient turbulent boundary layers*. PhD thesis, UNiversity of Melbourne, 2012.
- [80] M. D. Deshpande and D. P. Giddens. Turbulence measurements in a constricted tube. *Journal of Fluid Mechanics*, 97(1):65–89, 1980. ISSN 14697645. doi: 10.1017/S0022112080002431.
- [81] Linda Deutz. Study of the properties of turbulent flow through a venturi using LDA techniques. *MSc Thesis, TU Delft*, 2003.
- [82] Jun Chen, Joseph Katz, and Charles Meneveau. Study of Scale Interactions in strained and destrained Turbulence. In *ASME Heat Transfer/Fluids Engineering Summer Conference*, number 4, 2018.
- [83] L. R. Joel Sundstrom and Michel J. Cervantes. On the Similarity of Pulsating and Accelerating Turbulent Pipe Flows. *Flow, Turbulence and Combustion*, 100(2):417–436, 2018. ISSN 15731987. doi: 10.1007/s10494-017-9855-5.
- [84] V. C. Patel and M. R. Head. Some observations on skin friction and velocity profiles in fully developed pipe and channel flows. *Journal of Fluid Mechanics*, 38:181–201, 1969.
- [85] A A Draad, G D C Kuiken, and F T M Nieuwstadt. Laminar-Turbulent transition in pipe flow for Newtonian and non-Newtonian fluids. 377:267–312, 1998.
- [86] Jerke Eisma, Jerry Westerweel, Gijs Ooms, and Gerrit E. Elsinga. Interfaces and internal layers in a turbulent boundary layer. *Physics of Fluids*, 27(5), 2015. ISSN 10897666. doi: 10.1063/1.4919909. URL <http://dx.doi.org/10.1063/1.4919909>.
- [87] J. Westerweel M. Gul, G.E. Elsinga. Internal Shear Layers and Edges of Unifrom Momentum Zones in a Turbulent Pipe Flow. *Journal of Fluid Mechanics*, Submitted, 2019.
- [88] R. E. Britter, J. C.R. Hunt, and J. C. Mumford. The distortion of turbulence by a circular cylinder. *Journal of Fluid Mechanics*, 92(2):269–301, 1979. ISSN 14697645. doi: 10.1017/S0022112079000628.
- [89] John Kim, Parviz Moin, and Robert Moser. Turbulence statistics in fully developed channel flow at low reynolds number. *Journal of Fluid Mechanics*, 177(May):133–166, 1987. ISSN 14697645. doi: 10.1017/S0022112087000892.
- [90] James M. Wallace. Space-time correlations in turbulent flow: A review. *Theoretical and Applied Mechanics Letters*, 4(2):022003, 2014. ISSN 20950349. doi: 10.1063/2.1402203.
- [91] Juan A. Sillero, Javier Jiménez, and Robert D. Moser. Two-point statistics for turbulent boundary layers and channels at Reynolds numbers up to 2000. *Physics of Fluids*, 26(10), 2014. ISSN 10897666. doi: 10.1063/1.4899259. URL <http://dx.doi.org/10.1063/1.4899259>.
- [92] G. E. Elsinga, T. Ishihara, M. V. Goudar, C. B. Da Silva, and J. C.R. Hunt. The scaling of straining motions in homogeneous isotropic turbulence. *Journal of Fluid Mechanics*, 829:31–64, 2017. ISSN 14697645. doi: 10.1017/jfm.2017.538.
- [93] A Klein. REVIEW: Turbulent Developing Pipe FLOW. 103(June 1981):243–249, 1981.
- [94] White, Frank M. and Isla Corfield. *Viscous fluid flow*. New York: McGraw-Hill, vol. 3 edition, 2006.